INCLUSIVE MEASUREMENTS OF THE $pp \rightarrow pn\pi^+$ REACTION AT 420 AND 500 MeV

By

ROBERT GORDON PLEYDON

A THESIS SUBMITTED IN PARTIAL FULFILLMENT
OF THE REQUIREMENTS FOR THE DEGREE OF
MASTER OF SCIENCE
IN THE DEPARTMENT
OF PHYSICS.

DEPARTMENT OF PHYSICS
THE UNIVERSITY OF MANITOBA
WINNIPEG, MANITOBA
CANADA

© April, 1997

National Library of Canada
Acquisitions and Bibliographic Services
395 Wellington Street
Ottawa ON K1A 0N4
Canada

Bibliothèque nationale du Canada
Acquisitions et services bibliographiques
395, rue Wellington
Ottawa ON K1A 0N4
Canada

Your file Votre référence

Our file Notre référence

The author has granted a non-exclusive licence allowing the National Library of Canada to reproduce, loan, distribute or sell copies of this thesis in microform, paper or electronic formats.

The author retains ownership of the copyright in this thesis. Neither the thesis nor substantial extracts from it may be printed or otherwise reproduced without the author's permission.

L'auteur a accordé une licence non exclusive permettant à la Bibliothèque nationale du Canada de reproduire, prêter, distribuer ou vendre des copies de cette thèse sous la forme de microfiche/film, de reproduction sur papier ou sur format électronique.

L'auteur conserve la propriété du droit d'auteur qui protège cette thèse. Ni la thèse ni des extraits substantiels de celle-ci ne doivent être imprimés ou autrement reproduits sans son autorisation.

0-612-23458-4

Canada

THE UNIVERSITY OF MANITOBA

FACULTY OF GRADUATE STUDIES

*****

COPYRIGHT PERMISSION PAGE

INCLUSIVE MEASUREMENTS OF THE $pp \rightarrow pn\pi^+$ REACTION AT 420 AND 500 MeV

By

ROBERT GORDON PLEYDON

A Thesis/Practicum submitted to the Faculty of Graduate Studies of The University of Manitoba in partial fulfillment of the requirements of the degree of

MASTER OF SCIENCE

Robert Gordon Pleydon **1997 (c)**

Permission has been granted to the Library of The University of Manitoba to lend or sell copies of this thesis/practicum, to the National Library of Canada to microfilm this thesis and to lend or sell copies of the film, and to Dissertations Abstracts International to publish an abstract of this thesis/practicum.

The author reserves other publication rights, and neither this thesis/practicum nor extensive extracts from it may be printed or otherwise reproduced without the author's written permission.

Abstract

Inclusive measurements of the pion differential cross sections and analyzing powers have been made for the reaction $pp \rightarrow pn\pi^+$ over the angular range 24° to 100°, using the SASP spectrometer at TRIUMF. A 1 cm thick liquid hydrogen target was used, with an identical empty cell for background determination. These studies included the $pp \rightarrow d\pi^+$ reaction for verification of the cross section normalization. Measurements extended to pion momenta as low as 80 MeV/c. Experimental cross sections are compared with a final state interaction model prediction and the contribution of the σ_{11} term. The analyzing powers closely follow those of the $pp \rightarrow d\pi^+$ reaction at the same centre of mass momentum and energy.

Acknowledgements

For patient guidance and supervision, Willie Falk.

For careful reading of my thesis and constructive comments thereon, Stan Yen and Norm Davison.

For the cheerful provision of a reliable target, Walter Kellner and the late John Pedersen.

For sharing their SASP lore, Pat Walden, Stan Yen, Dave Hutcheon, Andy Miller, Alan Ling and Elie Korkmaz.

For several figures and lessons on the history of SASP optics, Munasinghe Punyasena.

For technical support and interesting times with NOVA 2.0, the esteemed Peter Green.

For technical advice of various kinds, Corrie Kost, Russell King, Luis Fernandes and Randy Churchman.

For TRIUMF beam insights, Phil Levy and Anatoli Zelenski.

For the target diagrams, Al Wilson.

For an excellent place to be, the lunchers of the University of Manitoba.

Sverdrups of thanks to friend, colleague and avid Certs fan Araz Hamian, and to Mona Benjamintz, for her fine example.

Contents

Abstract

Acknowledgements i

List of Figures v

List of Tables xi

1 Introduction 1

1.1 The Pion 1

1.2 Pion production in nucleon-nucleon collision 1

1.3 E633 2

2 The Experiment 4

2.1 Beam 4

2.1.1 Energy calibration 4

2.1.2 Current measurement and the SEM 6

2.1.3 Polarization and the IBP 8

2.1.4 IBP vs SEM rates 12

2.2 Target 14

2.2.1 Energy loss in the target 17

2.3 SASP 18

2.3.1 Coordinate system 20

2.3.2 Focal plane 28

2.3.3 Transfer matrix 32

2.3.4 Dispersion 33

2.3.5 Event trigger 34

2.3.6 NOVA 38
2.3.7 Coordinate corrections 39
2.3.8 Particle identification 42
2.3.9 Missing mass 46
2.3.10 Acceptance and survival 50
2.3.11 Livetime 51
2.3.12 Detector efficiency 53
2.3.13 VDC and FEC meantime 55
2.4 Run plan 57

3 Analysis and Results **60**
3.1 Analysis 60
3.1.1 Cross section 60
3.1.2 Subtraction of synchronous muons 62
3.1.3 Subtraction of the deuteron peak 64
3.1.4 Analyzing power 67
3.1.5 Statistical error 67
3.1.6 Systematic error 70
3.1.7 Measurements without the Front End Chamber 71
3.2 Results 72
3.2.1 $pp \rightarrow d\pi^+$ 72
3.2.2 $pp \rightarrow pn\pi^+$ 73

4 Discussion **90**
4.1 Theory 90
4.2 Comparison of experimental results with theory 91
4.2.1 $pp \rightarrow d\pi^+$ 91
4.2.2 $pp \rightarrow pn\pi^+$ 92

5 Conclusions **93**
5.1 Recommendations 93
5.2 Conclusions 93

Bibliography **95**

A Glossary of variables **97**

B E633 NOVA off-line OPSEQ **102**

C The E633_ANAL.FOR program **106**

D The MUON_MC.FOR program **118**

List of Figures

2.1 Beamline 4B in the Proton Hall, showing the major components of a SASP experiment. Adapted from [7]. 5

2.2 The ratios of spin UP/DOWN counts from the SEM and IBP. The SEM indicates false asymmetries at low currents. 9

2.3 A schematic of the detector layout of the In-Beam Polarimeter (a) and its counter logic (b) [7]. 10

2.4 The difference between measured P_{UP} and P_{DOWN}—an indicator of instrumental asymmetry. 12

2.5 Ratios of beam current measurements from SEM and IBP, (a) before and (b) after SEM 'dark current' correction. 13

2.6 Beam current ratios from the IBP and SEM with corrected IBP target thicknesses. The difference between the two beam energies—the 420 MeV ratios are approximately 6% higher than the 500 MeV ratios—is unexplained. 14

2.7 The E633 target assembly. 15

2.8 The target ladder. 16

2.9 The cyindrical target shell, showing the beam entrance window and the particle exit window. 17

2.10 Particle paths in the target. 18

2.11 Momentum corrections for energy loss in the target, at two reaction angles, beam energy 420 MeV. 19

2.12 The Second Arm SPectrometer (SASP) [15]. 21

2.13 The points of interest, and their coordinate systems, along the SASP particle path. 23
2.14 NOVA histograms of the target coordinates STHI_L3 (a) and SXI_L3 (b). The target position was calculated from the target angle and the X coordinate at the FEC. 24
2.15 NOVA histograms of the Y Transport coordinate at the target, calculated without (a) and with (b) FEC data. 25
2.16 NOVA histograms of target angle ϕ_i, calculated from focal plane coordinates (a) and from FEC data (b). 26
2.17 A schematic showing the orientation of the VDC X and U wires. 27
2.18 NOVA histograms of particle coordinates at the SASP focal plane. . . . 29
2.19 Schematic of the SASP focal plane and VDCs, also showing the Transport coordinate system and an arbitrary particle trajectory 31
2.20 A schematic diagram of the trigger electronics. Adapted from [7]. At the upper left are the input signals which comprise the event trigger: the scintillator paddles PDn; the two photomultipliers of the large S1 scintillator; and the VDC X1 plane. 35
2.21 Schematic of signal timing from X1, the Paddle OR, S1, and the RF pulses. The delay shown represents various delays applying to the Latch signal and the RF pulses. 37
2.22 The NOVA userfunctions of E633 data analysis. 40
2.23 A selected region of LX2POS, showing the gap (a), and (b) the same region after 'filling'. 41
2.24 Correlation plots of ϕ_i calculated from focal plane coordinates versus ϕ_i with FEC coordinates, where the former is calculated without (a) and with (b) aberration corrections. 43
2.25 HSPID: a particle identification spectrum showing pion, muon and positron loci, distinguishable by their different timing. LAPDSUM is the sum of scintillator paddle signals for the event, which is an indication of ionization in the scintillator array. 44

2.26 A plot of calculated pion characteristics in the SASP spectrometer. Pions of higher kinetic energy have smaller flight times and lose less energy in the scintillator material. 45

2.27 Schematic of the general $pp \rightarrow pn\pi^+$reaction. Vectors represent the incident beam proton, the scattered pion, and the recoil proton-neutron system. 46

2.28 The Transport coordinates beyond the target. The Transport angles made by the beam and an arbitrary pion path with the central trajectory are shown. 48

2.29 Plots of target angle STHL_L3 versus Missing Mass minus deuteron mass. Small correlations (a) are corrected by a set of aberration corrections (b). 49

2.30 The pion survival fraction, plotted as a function of SDEL_Z, the deviation from the central momentum P_0. 51

2.31 Normalized cross sections for the reaction $pp \rightarrow d\pi^+$, measured across the focal plane at both E633 beam energies. The fitted curve is the SASP acceptance function. 52

2.32 Computer livetime versus event rate for spin states UP and DOWN. . . 53

2.33 Ratio of spin-gated to ungated Event totals, plotted against the spin-gated event rate. If the beam current remained stable during spin-flipping, this ratio should be constant. 54

2.34 Combined detector efficiency, with and without the FEC. Efficiency declines at increased rates, as measured by the X1 plane (a) and scintillator S1 (b). 56

3.1 Measured muon cross sections are shown for the lower momentum bites at several angles and energies, along with Monte Carlo predictions. Agreement is good in (a) and (d); corrections were made based on (b) and (c). 63

3.2 For beam energy 500 MeV, reaction angle 23.5°: (a) shows the estimated muon cross sections with and without the pion survival factor, and the measured cross sections before and after muon subtraction; (b) shows the analyzing powers before and after corrections for muon subtraction. . . 65

3.3 A cross section measurement including the deuteron peak and the beginning of the three body continuum (a). An expansion of the separation region (b) illustrates the peak subtraction technique; shown are the original cross section measurement σ_m, the reflected peak shape σ_d and the peak-subtracted cross section σ_s, with error. 66

3.4 Measured cross sections for the reaction $pp \rightarrow d\pi^+$, calculated with and without FEC data, and the accepted values [25]. Statistical error bars are smaller than the plotting symbols. 72

3.5 Cross sections and analyzing powers for $pp \rightarrow pn\pi^+$. 500 MeV, θ=23.6°, with the predictions of Falk/Wilkin. For the cross section, the Wilkin prediction is also shown with a σ_{11} term added. 74

3.6 Cross sections and analyzing powers for $pp \rightarrow pn\pi^+$. 500 MeV, θ=35.0°, with the predictions of Falk/Wilkin. For the cross section, the Wilkin prediction is also shown with a σ_{11} term added. 75

3.7 Cross sections and analyzing powers for $pp \rightarrow pn\pi^+$. 500 MeV, θ=45.0°, with the predictions of Falk/Wilkin. For the cross section, the Wilkin prediction is also shown with a σ_{11} term added. 76

3.8 Cross sections and analyzing powers for $pp \rightarrow pn\pi^+$. 500 MeV, θ=55.0°, with the predictions of Falk/Wilkin. For the cross section, the Wilkin prediction is also shown with a σ_{11} term added. The cross section results have been scaled down from the cross sections calculated without FEC data. 77

3.9 Cross sections and analyzing powers for $pp \rightarrow pn\pi^+$. 500 MeV, θ=65.1°, with the predictions of Falk/Wilkin. For the cross section, the Wilkin prediction is also shown with a σ_{11} term added. 78

3.10 Cross sections and analyzing powers for $pp \rightarrow pn\pi^+$. 500 MeV, θ=75.2°, with the predictions of Falk/Wilkin. For the cross section, the Wilkin prediction is also shown with a σ_{11} term added. 79
3.11 Cross sections and analyzing powers for $pp \rightarrow pn\pi^+$. 500 MeV, θ=85.1°, with the predictions of Falk/Wilkin. For the cross section, the Wilkin prediction is also shown with a σ_{11} term added. 80
3.12 Cross sections and analyzing powers for $pp \rightarrow pn\pi^+$. 500 MeV, θ=100.0°, with the predictions of Falk/Wilkin. For the cross section, the Wilkin prediction is also shown with a σ_{11} term added. The cross section results were scaled down from the cross section calculated without FEC data. . 81
3.13 Cross sections and analyzing powers for $pp \rightarrow pn\pi^+$. 420 MeV, θ=25.1°, with the predictions of Falk/Wilkin. For the cross section, the Wilkin prediction is also shown with a σ_{11} term added. 82
3.14 Cross sections and analyzing powers for $pp \rightarrow pn\pi^+$. 420 MeV, θ=34.9°, with the predictions of Falk/Wilkin. For the cross section, the Wilkin prediction is also shown with a σ_{11} term added. 83
3.15 Cross sections and analyzing powers for $pp \rightarrow pn\pi^+$. 420 MeV, θ=45.0°, with the predictions of Falk/Wilkin. For the cross section, the Wilkin prediction is also shown with a σ_{11} term added. 84
3.16 Cross sections and analyzing powers for $pp \rightarrow pn\pi^+$. 420 MeV, θ=55.1°, with the predictions of Falk/Wilkin. For the cross section, the Wilkin prediction is also shown with a σ_{11} term added. 85
3.17 Cross sections and analyzing powers for $pp \rightarrow pn\pi^+$. 420 MeV, θ=65.1°, with the predictions of Falk/Wilkin. For the cross section, the Wilkin prediction is also shown with a σ_{11} term added. 86
3.18 Cross sections and analyzing powers for $pp \rightarrow pn\pi^+$. 420 MeV, θ=75.1°, with the predictions of Falk/Wilkin. For the cross section, the Wilkin prediction is also shown with a σ_{11} term added. 87
3.19 Cross sections and analyzing powers for $pp \rightarrow pn\pi^+$. 420 MeV, θ=85.1°, with the predictions of Falk/Wilkin. For the cross section, the Wilkin prediction is also shown with a σ_{11} term added. 88

3.20 Cross sections and analyzing powers for $pp \rightarrow pn\pi^+$. 420 MeV, θ=100.0°, with the predictions of Falk/Wilkin. For the cross section, the Wilkin prediction is also shown with a σ_{11} term added. The cross section results were scaled down from the cross section calculated without FEC data. . 89

List of Tables

1.1 Isospin decomposition for the cross sections of proton-proton pion production. The subscripts on σ refer to the isospin state of the nucleons before and after the reaction. 2

2.1 The momenta of pions from the $pp \rightarrow d\pi^+$ reaction in the two momentum scans, and the beam energies calculated from them. 7

2.2 Calibration constants of the Secondary Emission Monitor. 7

2.3 Current calibration constants of the IBP [11]. 11

2.4 Design specifications for the Second Arm Spectrometer [13]. 19

2.5 Some of the SASP dimensions used in calculating coordinates. 28

2.6 A summary of the E633 data and background runs. 58

2.7 A list of runs with unpolarized beam. 59

Chapter 1

Introduction

1.1 The Pion

The pion was first hypothesized by Yukawa as the quantum of the strong nuclear force [1]. Virtual pions are considered to mediate in the exchange of momentum and charge in nucleon-nucleon interactions at the longer range of the strong force. Above a certain threshold energy level, the pion can become a physical particle. By observing the produced pions we can learn about the physics of nucleon-nucleon interaction, both as free particles and within a nucleus.

1.2 Pion production in nucleon-nucleon collision

The reaction $pp \rightarrow pn\pi^+$ is one of the pion-producing nucleon-nucleon interactions. which follow the general form

$$N + N \rightarrow N + N + \pi. \tag{1.1}$$

Proton-proton collisions result in three possible outcomes within this category, which are listed in table 1.1 along with their isospin decompositions. The reaction $pp \rightarrow pn\pi^+$ involves a mixture of two isospin channels which cannot be determined from the measurements of the single channel reactions.

Above the three body energy threshold, all three reactions will occur. Using a magnetic spectrometer, the $pp \rightarrow pp\pi^0$ reaction is excluded, and deuteron production is

Reaction	Isospin Decomposition
$pp \rightarrow d\pi^+$	$\sigma_{10}(d)$
$pp \rightarrow pp\pi^0$	σ_{11}
$pp \rightarrow pn\pi^+$	$\sigma_{10}(np) + \sigma_{11}$

Table 1.1: Isospin decomposition for the cross sections of proton-proton pion production. The subscripts on σ refer to the isospin state of the nucleons before and after the reaction.

distinguished on the basis of the energy of the detected pion. For a given reaction angle, the two body reaction produces a sharp peak in measured pion energy, and the onset of $pp \rightarrow pn\pi^+$ is marked by the beginning of a continuum which commences several MeV lower.

1.3 E633

Bhatia *et al.* have measured analyzing powers and spin correlation parameters for $pp \rightarrow pn\pi^+$ at 650 and 800 MeV [2]. They detected all three outgoing particles, and measurements were made for pion angles 40.5° and 48.5° at 800 MeV, and 82.0° at 650 MeV. Hancock *et al.* have measured analyzing powers and cross sections at 800 MeV [3]. The proton and pion were detected in coincidence, for twelve angle pairs. Daehnick *et al.* have measured differential cross sections for $pp \rightarrow pn\pi^+$ just above the pion production threshold, at energies from 292.4 to 319.5 MeV [4]. The reaction kinematics were calculated from the energies of coincident protons and neutrons.

Between these energies there were inclusive measurements of cross sections and analyzing powers at 400 and 450 MeV by Falk *et al.* [5]. Reaction angles were 46° to 88° (lab). These measurements used a CH_2 target, and therefore involved the subtraction of pions produced on the carbon nucleus, and error was considerable. There were also measurements, by Waltham *et al.*, of spin correlations and spin asymmetries for $pp \rightarrow pn\pi^+$ [6]. These were exclusive measurements; all three outgoing particles were detected, for selected angles.

The purpose of E633 was to provide more precise inclusive cross section and analyzing power measurements in this intermediate energy range, at a nearly complete set of reaction angles, and over the entire observable pion momentum range.

Polarized proton beams at 420 and 500 MeV struck a target of liquid hydrogen 1 cm thick. Pions were detected in TRIUMF's large solid angle SASP spectrometer, at scattering angles from 24 to 100 degrees. At each angle data were collected for all momenta from the deuteron peak through the three body continuum to the lower limit of detection.

E633 employed a new target which allowed simple switching from a full to empty cell. With this feature, background measurements could be made immediately before and after each data-taking run, for the same spectrometer setting.

Chapter 2

The Experiment

E633 was carried out at TRIUMF in Vancouver, Canada, using the Second Arm Spectrometer (SASP), located in the Proton Hall on beamline 4B. Figure 2.1 shows the locations of the significant devices.

2.1 Beam

The TRIUMF cyclotron can deliver up to 600 nA of polarized protons at energies from 183 to 520 MeV. In E633 measurements were made using two beam energies, 420 MeV and 500 MeV. Beam current ranged from $\sim$ 0.1 nA to $\sim$ 8 nA. The beam was delivered in 1.5 ns pulses every 43 ns, originating in an optically-pumped polarized ion source. The beam's vertical polarization was nominally 75%, except in a few unpolarized runs to test the polarization measurement instrumental asymmetry.

2.1.1 Energy calibration

In the medium energy resolution (MERO) set-up, the beam energy stability is better than 0.1%, but the beam energy is only known, *a priori*, to within 1 MeV. Therefore it was desirable to perform a beam energy calibration with the experimental data. In the $pp \rightarrow d\pi^+$ reaction, two-body kinematics directly relate the beam energy to the momentum of the outgoing pion, for a given reaction angle. In two momentum scans of the spectrometer, eleven measurements of $pp \rightarrow d\pi^+$ were made at each of the two beam energies. Table 2.1 lists the measured momenta of the detected pions from the

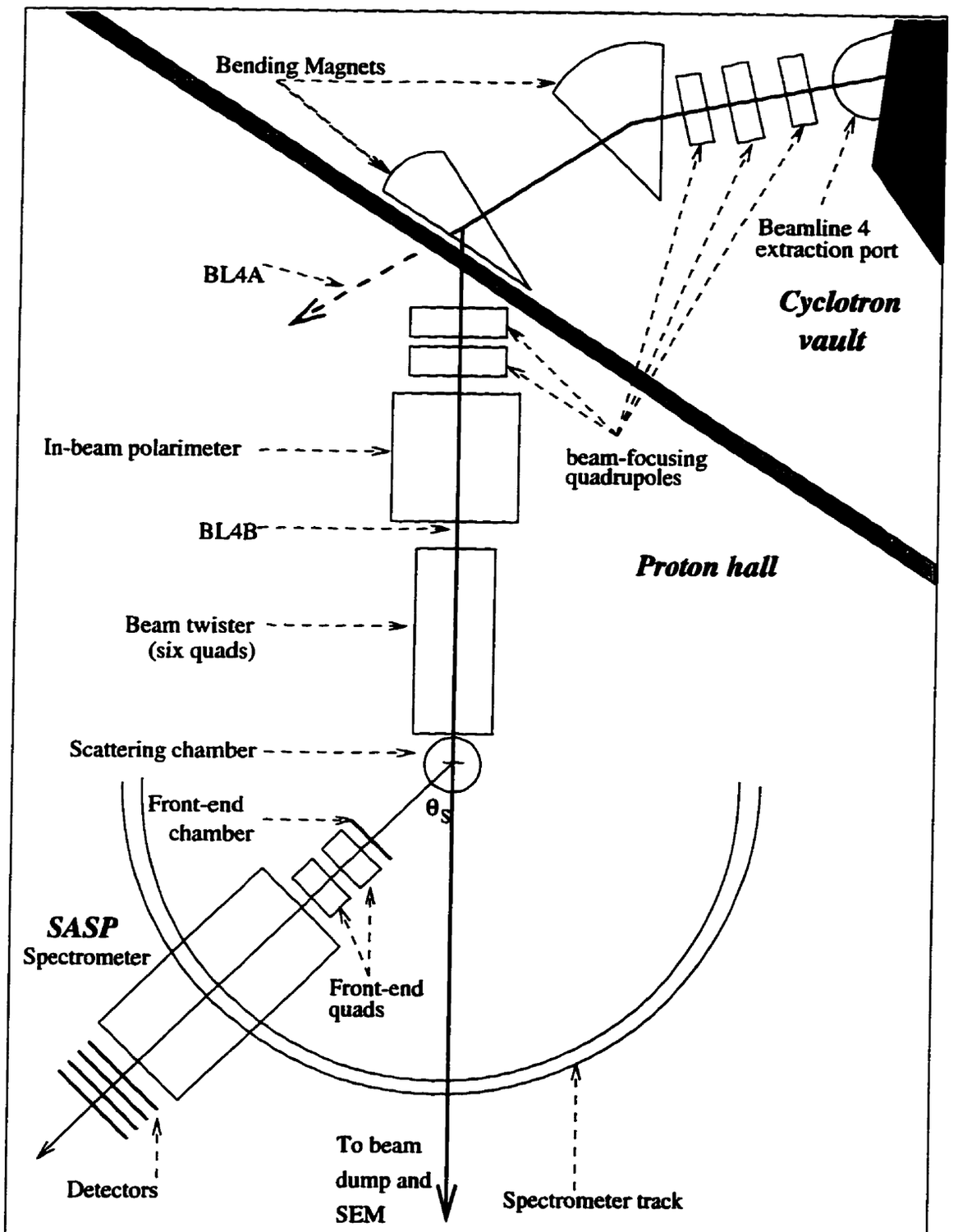

Figure 2.1: Beamline 4B in the Proton Hall, showing the major components of a SASP experiment. Adapted from [7].

two-body reaction, and the beam energies calculated from them. Systematic error arises from uncertainty in the reaction angle, θ, and the SASP momentum calibration [8]. All reported data analysis used these mean beam energies for kinematics.

2.1.2 Current measurement and the SEM

Current on beamline 4B was continuously monitored using the Secondary Emission Monitor (SEM) located near the beam dump.

The Secondary Emission Monitor (SEM) consists of a series of aluminum foils in an evacuated chamber. Alternating foils are at high voltage, so a current flows when passing protons liberate electrons from the aluminum. This current is collected in a capacitor. When the capacitor charge exceeds 0.1014 nC [9], the SEM counter is incremented and the capacitor is drained to begin accumulating again.

There is, necessarily, a random error of ± 1 in total SEM counts. Furthermore, it had been speculated in the past that there might also be a SEM 'dark current'—an apparent current in the SEM even when no beam was passing through it—due to background radiation, pickup in the wiring, or some other cause. Comparison of the SEM current measurement with IBP current measurement at low levels (see figure 2.5) suggested a dark current of 0.0366 counts/second during E633, and this figure was subtracted from the measured current for data analysis. The evidence for this correction is presented in section 2.1.4. After E633 a 'dark' count rate of 0.07 counts/second (four consecutive measurements of 7 counts in 99.9 seconds; negative polarity only; no beam present) in the 4B2 SEM was discovered [10]. This higher rate would be inconsistent with our experimental data, so the empirical value of 0.0366/s was used.

The SEM count rate is calibrated to beam current for different energies with a Faraday Cup. A recent calibration [9] established the relationship between the SEM count and the total charge that has passed through it:

$$C_{SEM}/0.1nC/\frac{dE}{dx}(Al) = 0.30777 \tag{2.1}$$

where $\frac{dE}{dx}(Al)$ has the units MeV/g/cm^2. The coefficients for converting SEM counts to charge are listed in table 2.2.

The scalers counting pulses from the SEM current integrator were gated by the

E633 BEAM ENERGY					
$\theta = 23.6°$			$\theta = 55.0°$		
Run #	P_π(MeV/c)	T_{beam}(MeV)	Run #	P_π(MeV/c)	T_{beam}(MeV)
75	294.90	500.24	269	166.94	420.00
76	295.84	500.19	270	167.13	420.27
77	294.76	500.09	275	166.80	419.81
78	294.49	499.76	277	166.67	419.62
79	294.50	499.78	278	166.54	419.44
80	294.46	499.72	280	166.67	419.62
81	294.62	499.91	281	166.70	419.66
82	294.52	499.79	282	166.75	419.74
83	294.66	499.97	283	166.73	419.72
84	294.45	499.72	284	166.56	419.67
85	294.01	499.12	285	166.17	420.33
Mean		499.85	Mean		419.79
Std. dev.		0.28	Std. dev.		0.28
Syst. error		0.53	Syst. error		0.36

Table 2.1: The momenta of pions from the $pp \rightarrow d\pi^+$ reaction in the two momentum scans, and the beam energies calculated from them.

Energy	$\frac{dE}{dx}(Al)$	C_{SEM}
MeV	$MeV/gm/cm^2$	*counts/nC*
499.9	2.18	6.71
419.8	2.35	7.24

Table 2.2: Calibration constants of the Secondary Emission Monitor.

polarization state of the beam. At the lower beam currents of this experiment, the ratio of UP counts to DOWN counts became erratic. This occurs when the SEM count frequency falls far below the spin flip frequency (40 Hz); when this happens the ratio is strongly influenced by the statistical sorting error of the few SEM events into spin states. For example, at 500 MeV and $I_{BEAM} = 0.1$ nA, the SEM count rate was only ~ 0.7 Hz, with total counts typically around 700. This error is not present in In-Beam Polarimeter (IBP) data (see figure 2.2) because of its much higher rates. Consequently, the SEM total counts ($SEM_{UP} + SEM_{DOWN}$) were used as a measure of total current, but the ratio of currents I_{UP} to I_{DOWN} was taken from the count ratio of the IBP.

The total SEM accumulated current (charge) for an whole run, in nC, was

$$SEMI = \frac{SEM_{UP} + SEM_{DOWN} - 0.0366T}{C_{SEM}}, \tag{2.2}$$

where T is the total spin-gated run time, in seconds. The statistical error, in nC, is

$$\varepsilon_{SEMI} = \frac{2}{C_{SEM}}, \tag{2.3}$$

where the 2 arises from the ± 1 error in each of SEM_{UP} and SEM_{DOWN}.

2.1.3 Polarization and the IBP

Beam polarization was continuously measured with the In-Beam Polarimeter (IBP), a device situated upstream of the spectrometer. This measurement involves passing the beam protons through a material of known analyzing power—in this case polyethylene (CH_2)—and measuring the asymmetry e of the outgoing elastically scattered protons. Figure 2.3 shows the detectors which count protons scattered to the left and right of the beam in coincidence with recoil protons at the corresponding angle on the opposite side. An accidentals rate is simultaneously determined by counting coincidences between the scattered proton signals and recoil proton signals from the previous beam burst, 43 ns earlier. The subtraction of these random coincidences gives a corrected asymmetry:

$$e = \frac{(L - L_{acc}) - (R - R_{acc})}{(L - L_{acc}) + (R - R_{acc})}. \tag{2.4}$$

The vertical polarization P is

$$P = e/A_{IBP} \tag{2.5}$$

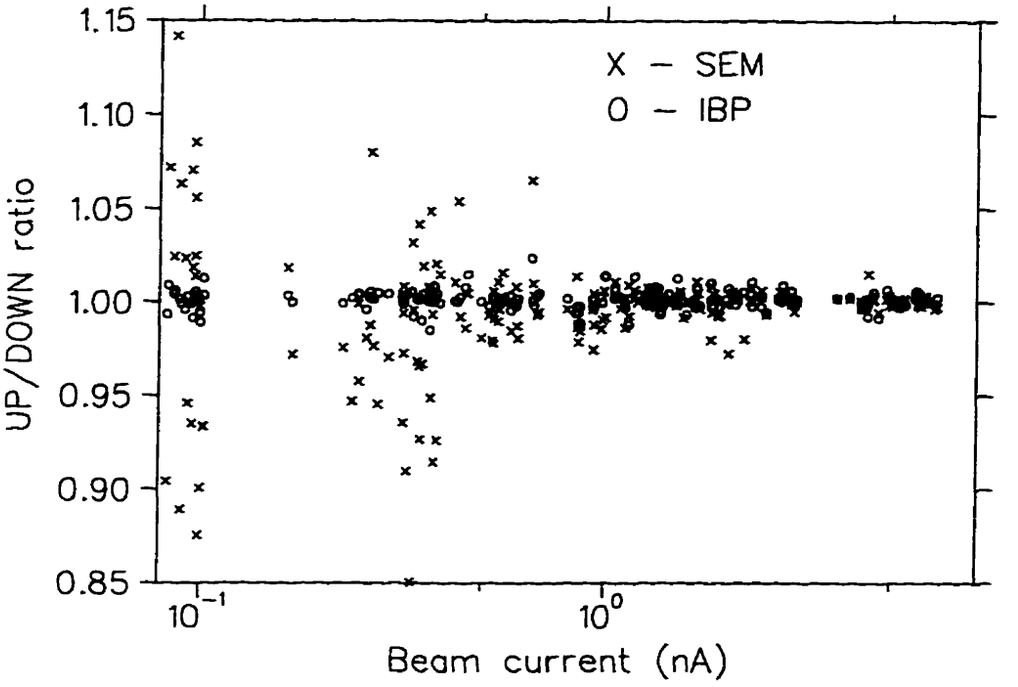

Figure 2.2: The ratios of spin UP/DOWN counts from the SEM and IBP. The SEM indicates false asymmetries at low currents.

where A_{IBP} is the analyzing power for pp scattering (with a correction for the carbon in the CH_2) : 0.470 at 500 MeV and 0.434 at 420 MeV [11]. The IBP can also be used as a current monitor by adding the Left and Right counts, and using a current calibration and the thickness of the target. The coefficents for the conversion of IBP counts to charge for the IBP targets used in E633 are listed in table 2.3.

The statistical error in polarization arises from the error in the asymmetry de

$$dP = de/A_{IBP}. \tag{2.6}$$

The statistical error in e comes from the contributions of the counting errors of the IBP detectors

$$(de)^2 = (dL)^2(\frac{\partial e}{\partial L})^2 + (dL_{acc})^2(\frac{\partial e}{\partial L_{acc}})^2 + (dR)^2(\frac{\partial e}{\partial R})^2 + (dR_{acc})^2(\frac{\partial e}{\partial R_{acc}})^2 \tag{2.7}$$

where $(dL)^2 = L$, and so on. In full, the polarization error is expressed

$$dP = \frac{2}{A_{IBP}} \frac{\sqrt{(L+L_{acc})(R-R_{acc})^2 + (R+R_{acc})(L-L_{acc})^2}}{((L-L_{acc})+(R-R_{acc}))^2}. \tag{2.8}$$

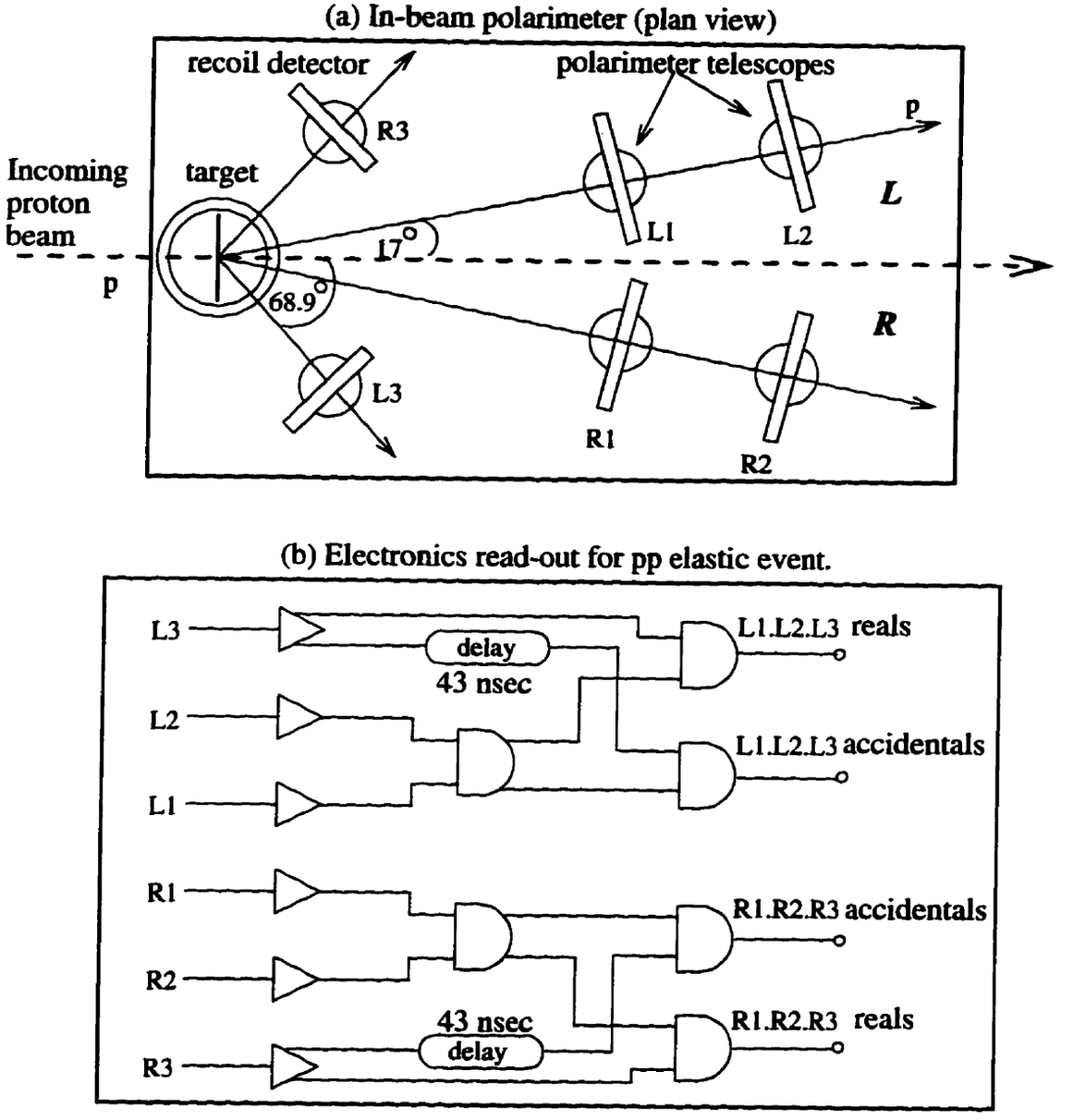

Figure 2.3: A schematic of the detector layout of the In-Beam Polarimeter (a) and its counter logic (b) [7].

Target #	density mg/cm^2	C_{IBP} $counts/nA$	Beam Energy MeV
3	1.60	111	500
		98	420
4	42.3	2945	500
		2595	420

Table 2.3: Current calibration constants of the IBP [11].

Spin-Off Correction

For unpolarized beam, e should be zero. A non-zero e would indicate an instrumental asymmetry, possibly due to detector misalignment, an electronics fault, beam misalignment, or photomultiplier gain difference. The procedure to determine the extent of instrumental asymmetry is to regularly measure e with an unpolarized beam, and subtract the resulting e_0 from the asymmetry in data-taking runs. In E633, there were not enough of these spin off runs to give a reliable value for e_0. Instead, we fitted the difference between the polarizations measured in the spin up and down states

$$P_{DIFF} = P_{UP} - |P_{DOWN}| \tag{2.9}$$

from all the runs. This quantity was a function of both run number and IBP target. The function fitted to P_{DIFF} was divided by 2 to get P_{CORR} which was added to the measured P_{UP} and subtracted from the measured P_{DOWN}. This procedure requires that the magnitude of the polarization was equal for the two spin states. This was assumed to be true because of the optically pumped polarized ion source. The source of polarization is optically pumped rubidium vapour in which the polarization reaches saturation levels equal in both spin states, which are stable against slight variations in pumping laser frequency and intensity. The equality of polarization magnitudes has also been extensively tested [12].

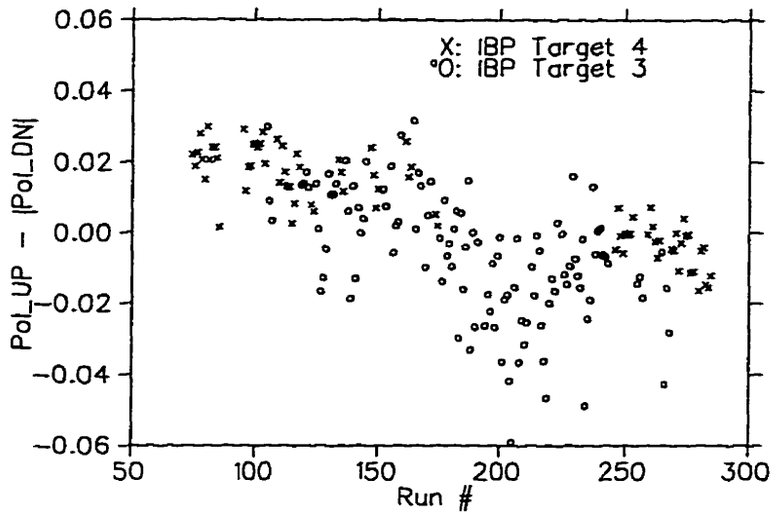

Figure 2.4: The difference between measured P_{UP} and P_{DOWN}—an indicator of instrumental asymmetry.

2.1.4 IBP vs SEM rates

Both the IBP and the SEM are current measuring devices. The SEM has been directly calibrated to current with a Faraday Cup. The IBP calibration depends upon the thickness of its CH_2 target. This quantity was only measured to a precision of 10%. Furthermore, it is known that the target material warps in the heat of usage. Therefore. IBP current is not considered an accurate absolute measurement, or even necessarily consistent over the course of an experiment. Nonetheless, a comparison of currents calculated from the count rates of the two devices can be used to verify consistency. Systematic errors were inferred from the data shown in figure 2.5(a). Four different loci are apparent, separated by beam energy and IBP target. Curvature in these loci at lower currents led to suspicion of the SEM behaviour at low count rates, and the hypothesis of a constant 'dark current' which artificially raised I_{SEM}. Figure 2.5(b) shows the same ratios after the dark current correction given in section 2.1.2. After the experiment, a measurement with beam off determined a rate of 0.07 counts/second, but since the cause remains unknown, the correction determined from the experimental data was used.

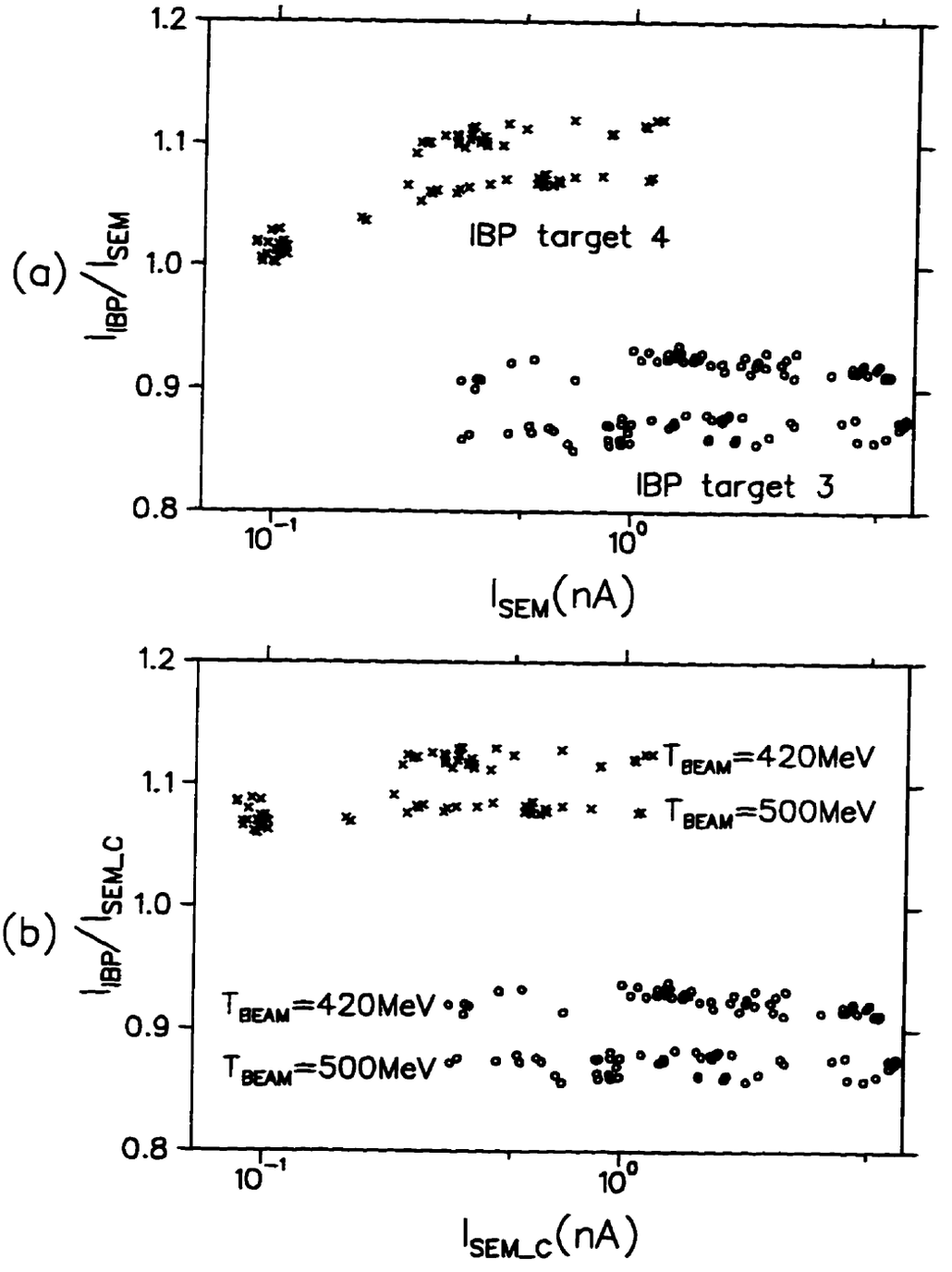

Figure 2.5: Ratios of beam current measurements from SEM and IBP, (a) before and (b) after SEM 'dark current' correction.

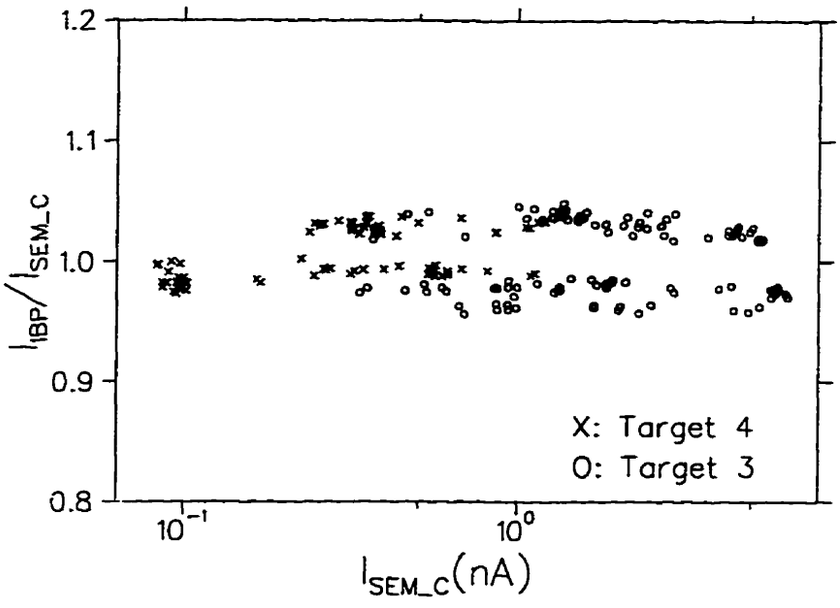

Figure 2.6: Beam current ratios from the IBP and SEM with corrected IBP target thicknesses. The difference between the two beam energies—the 420 MeV ratios are approximately 6% higher than the 500 MeV ratios—is unexplained.

It is possible to use the corrected data of figure 2.5(b) to correct the target thicknesses. Changes in target thickness—factors of 0.918 and 1.116 respectively—bring the target 4 loci down and the target 3 loci up to bracket unity, as shown in figure 2.6. There remains the unexplained systematic error between the two beam energies (the upper and lower lines in figure 2.6), which suggests an error in the energy-dependent calibration of either or both of the IBP and SEM. It could also be caused by overly high discriminator thresholds in the IBP. These would accept proportionally more of the protons at 420 MeV, because of their larger energy loss in the detectors.

2.2 Target

A new target built for E633 was designed for fast changes of target position and target angle. The target assembly within the scattering chamber is shown in figure 2.7. A target ladder moves vertically, under remote control, within a cylindrical shell, which

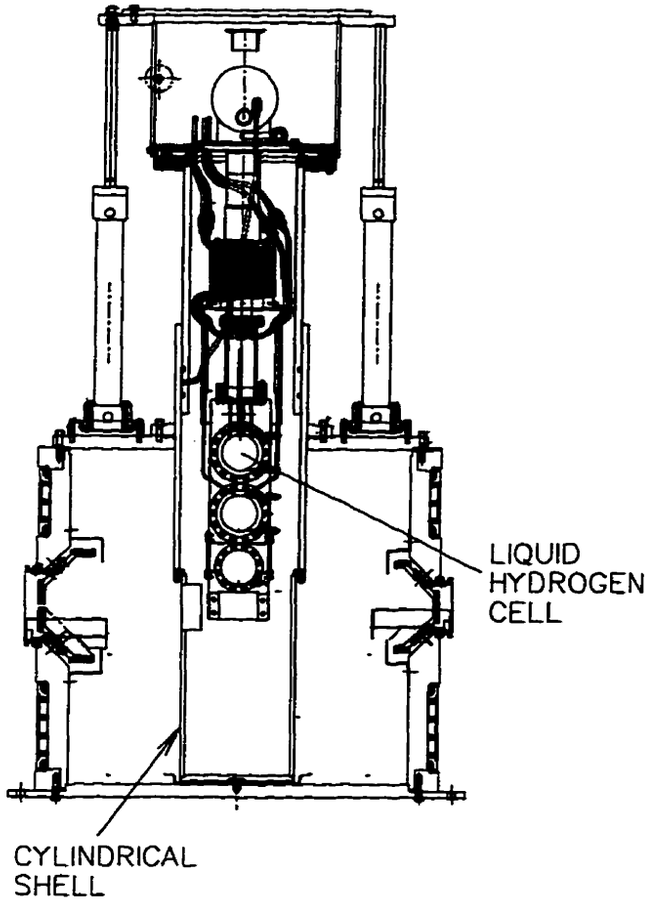

Figure 2.7: The E633 target assembly.

forms an second, inner vacuum chamber within the evacuated scattering chamber.

The target ladder is shown in figure 2.8. Starting at the top, there is a liquid hydrogen cell, a liquid deuterium cell (not used in this experiment), an empty dummy cell for background measurements, and a ZnS scintillator for examining the beam profile. A layer of CH_2 (polyethylene) was placed over the ZnS as a test target.

The liquid hydrogen cell consisted of two 0.001" stainless steel foils holding LH_2 at an absolute pressure of 16.0 - 16.5 psi. This pressure caused the foils, held 5 mm apart at the cell perimeter, to bulge outward, resulting in a central thickness of 9.8 mm. The diameter of the cell was 7 cm. The dummy target was 5 cm in diameter but was otherwise identical in construction. Not being pressurized, the dummy cell walls

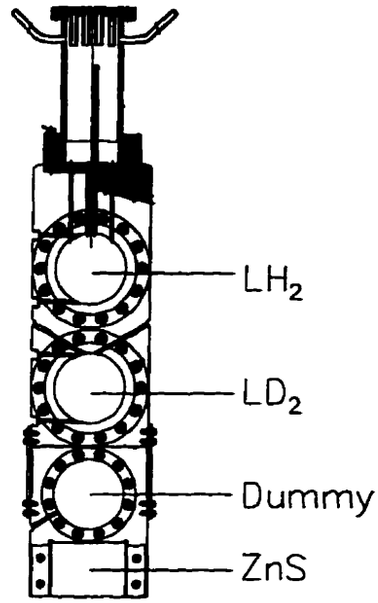

Figure 2.8: The target ladder.

remained 5 mm apart. The target ladder was wrapped in a thick layer of superinsulation, with holes over the targets. Then a thin sleeve of superinsulation completely covered the target ladder, stopping at the top of the scintillator.

The cylindrical shell is shown in figure 2.9. Its windows consisted of 0.005" Mylar over the entrance window, and 0.005" Kapton over the exit window, with an additional 0.001" of aluminum placed over the beam entrance and exit areas.

The target angle—its orientation with respect to the beam axis—could be changed by manually rotating the target frame assembly.

The range of accessible reaction angles was limited by three factors. The Second Arm Spectrometer (SASP) can be placed at a minimum angle of 23.6° to the beam. The target shell exit window is open to 135°, which is also the maximum SASP angle. Finally, the target cell foil retaining rings (represented schematically in figure 2.10) place a limit on the maximum reaction angle measured with respect to a perpendicular to the target cell. This last limit is a function of beam spot size (typically 2 mm wide by 2 cm high) and target angle, but could be safely taken to be 70°.

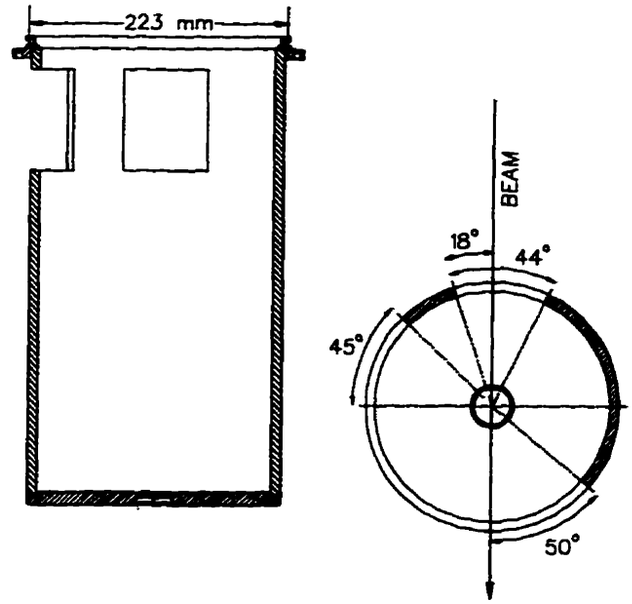

Figure 2.9: The cyindrical target shell, showing the beam entrance window and the particle exit window.

2.2.1 Energy loss in the target

E633 used a thick target in which energy loss was significant. In data analysis, energy loss was calculated on an event-by-event basis and restored to the measured pion momentum, so that the kinematics of a lossless reaction would be approximated. Figure 2.10 shows the particle paths in the target. Energy loss was based on averaging the losses for reactions occurring at the beginning and at the end of the active area where the beam passes through the target. Tracing backwards, we observe that the pion loses energy in the cell window on departure and in the LH_2 from the reaction point to the window. The incoming proton would have already lost energy moving through the liquid hydrogen to the reaction, and as it entered through the first cell window. The thicknesses of the materials 'seen' by the particles are functions of target and reaction (SASP) angles. The translation of beam proton energy loss into resultant pion loss involves a proportionality factor which is approximately a function of reaction angle.

Energy loss in the shell entrance and exit windows was also considered.

The restored momentum, calculated in the NOVA userfunction USRR, ranged from

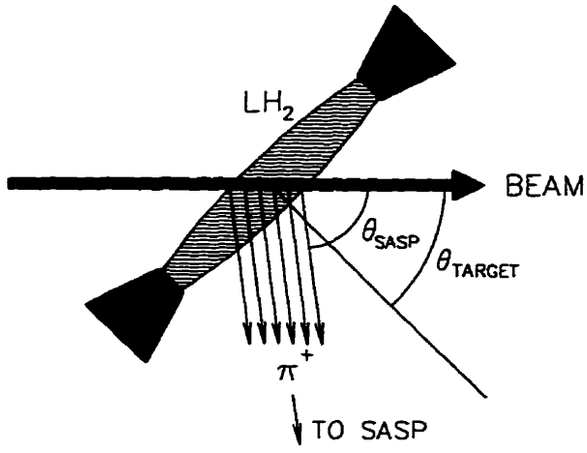

Figure 2.10: Particle paths in the target.

below the level of resolution to about 2 MeV/c. Some typical corrections are shown in figure 2.11.

2.3 SASP

The Second Arm Spectrometer (SASP) is a quadrupole-quadrupole-dipole spectrometer which came into operation in early 1994. The SASP layout is shown in figure 2.12. Specifications are listed in table 2.4. The spectrometer pivots about the target in the scattering chamber, to detect outgoing particles at different reaction angles. The angular range of SASP is 23° to 135° (or -23° to -135°, by the Madison coordinate system convention).

Particles from the target leave the scattering chamber through a windowless sliding seal and are focused by the two quadrupoles. The focused beam passes through the dipole magnet where it is bent upwards by 90° and resolved into its constituent momenta at the focal plane (shown in figure 2.12 as a curved line below VDC1).

The detector system consists of a series of wire chambers and scintillators. Particles first pass through the Front End Chamber (FEC). The FEC is an optional detector of SASP, used in E633 because particle flux was fairly low. The FEC is a wire chamber with wires strung vertically and horizontally to measure the X (bend plane) and Y

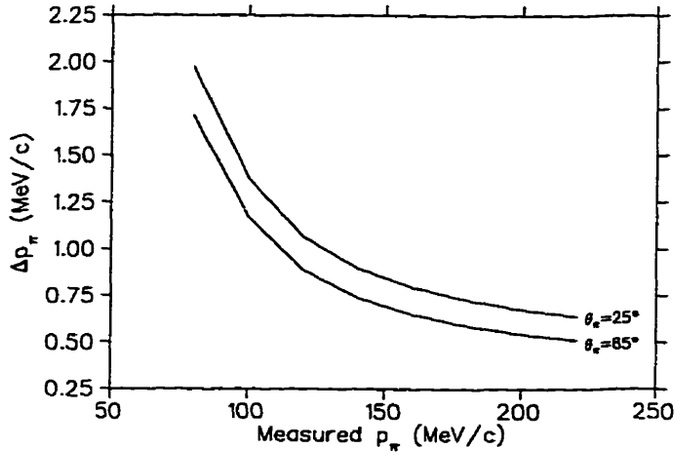

Figure 2.11: Momentum corrections for energy loss in the target, at two reaction angles. beam energy 420 MeV.

SASP Specifications	
design central momentum:	660 MeV/c
maximum central momentum:	720 MeV/c
momentum bite:	-10% to 15%
solid angle:	13.5 msr at central momentum
resolution $\frac{\Delta p}{p}$:	1.74×10^{-4} at central momentum
Dispersion/Magnification:	4.70 cm/%
flight path:	7.02 m at central momentum
angular acceptance:	± 85 mr in bend plane
	± 43 mr in non-bend plane

Table 2.4: Design specifications for the Second Arm Spectrometer [13].

(non-bend plane) coordinates, and provides the first location information beyond the target for particles passing through the spectrometer. The FEC output can be used for event triggering (discussed in section 2.3.5) and for the determination of time-of-flight through the spectrometer, but in E633 FEC data was used primarily for particle path reconstruction and chamber efficiency calculations.

The particles are next 'seen' as they pass through the Vertical Drift Chambers (VDCs). Currents in the VDC wires indicate the position of a particle as it passes amongst them. Coordinates are reported in X and U, which can be combined to give a Y (non-bend plane) coordinate (the U wires are strung at an angle of 30° to the X wires; perpendicular Y wires would be too long). With X and Y information from VDC1 and VDC2, the intersection of the particle track with the focal plane can be calculated. VDC1's X plane was also used as part of the event trigger.

Above the VDCs are five focal plane scintillator paddles. A signal from one or more of the paddles is part of the event trigger. The strength of the scintillator signal—proportional to the energy lost by the particle as it passed through the material—is an approximate measure of the kinetic energy of the particle; for a given type, slower particles lose more energy as they pass through matter than faster ones. This information is used in particle identification, which is discussed in section 2.3.8.

The last detector is a large scintillator called S1. A signal from S1 is the last component of an event trigger.

2.3.1 Coordinate system

The path of scattered particles, as they pass from the target through SASP, is described by coordinates in the TRANSPORT coordinate system [14]. The conventions of the Transport system are:

- Z is measured along an outgoing central trajectory, and is measured in metres.
- X is perpendicular to Z, lying in the spectrometer *bend plane*, and is measured in the direction of increasing momentum (in the spectrometer). X is measured in centimetres.

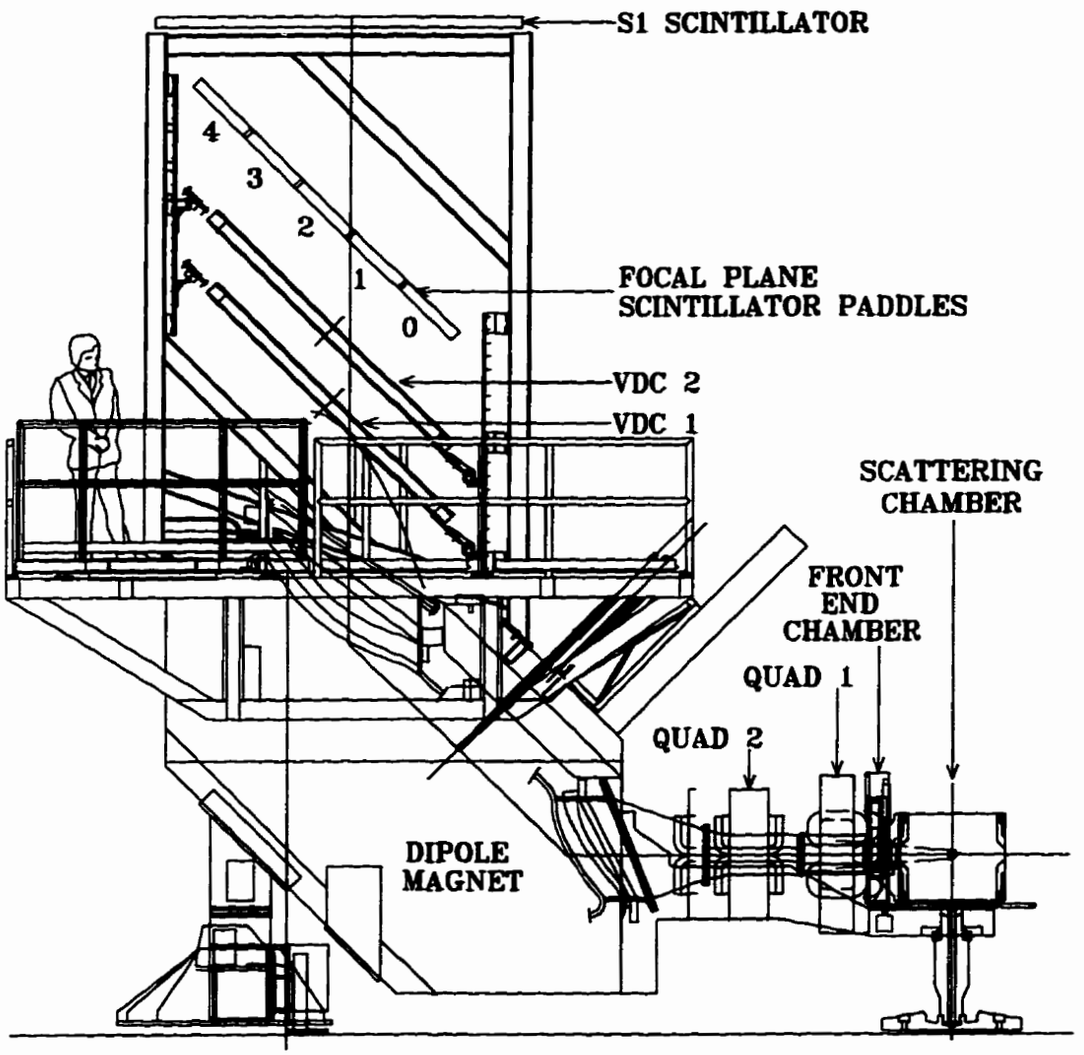

Figure 2.12: The Second Arm SPectrometer (SASP) [15].

- Y is perpendicular to X and Z, and therefore lies in the *non-bend plane*, and is directed to form a right-handed X-Y-Z system. Y is measured in centimetres.

- θ and ϕ are angles to the central trajectory. θ increases in the positive X direction; ϕ increases in the positive Y direction. Both angles are measured in milliradians.

A coordinate system of this kind can be established at any point along the beam path. We are interested in characterizing the particle path at the target, the FEC, and the focal plane (discussed in detail in section 2.3.2). Our detector system supplies spatial coordinates at the three wire chamber detectors. A schematic of the SASP system, showing Transport coordinate systems at three points along the central trajectory and the three detector systems (which have different units and orientations) appears in figure 2.13. Online and replay processing time is largely devoted to converting the raw detector output into detector system coordinates, and then calculating the desired Transport coordinates from these.

More details on how the wire chambers work—how the passage of a particle is recognized and converted to coordinate information—are provided in reference [7]. The following is a brief discussion of coordinates relevant to E633. Some of these will be considered in greater depth in section 2.3.7. Table 2.5 contains a selection of SASP dimensions used in the calculation of coordinates. The following is a list of coordinates defined in NOVA analysis (NOVA is the data analysis program, described in section 2.3.6). By local convention, SASP variables begin with S or L. Target and focal plane coordinates are designated with I and F, respectively; for instance, SXF is the X coordinate at the SASP focal plane. In many cases there was more than one way to calculate a coordinate, so a variable name often has an algorithm-identifying suffix after the coordinate label.

SXI is the Transport X coordinate at the target. In principle SXI, and in fact all target coordinates, are directly related to the focal plane coordinates through the transfer matrix, which is discussed in section 2.3.3. In E633, direct calculations of SXI in this way did not have sufficient accuracy. Instead, we used a corrected target angle STHI and projected back from the FEC event coordinate, SX0_TR

$$SXI_L3 = SX0_TR - (STHI_L3/1000) * (SFEC0DIST - 0.6400), \quad (2.10)$$

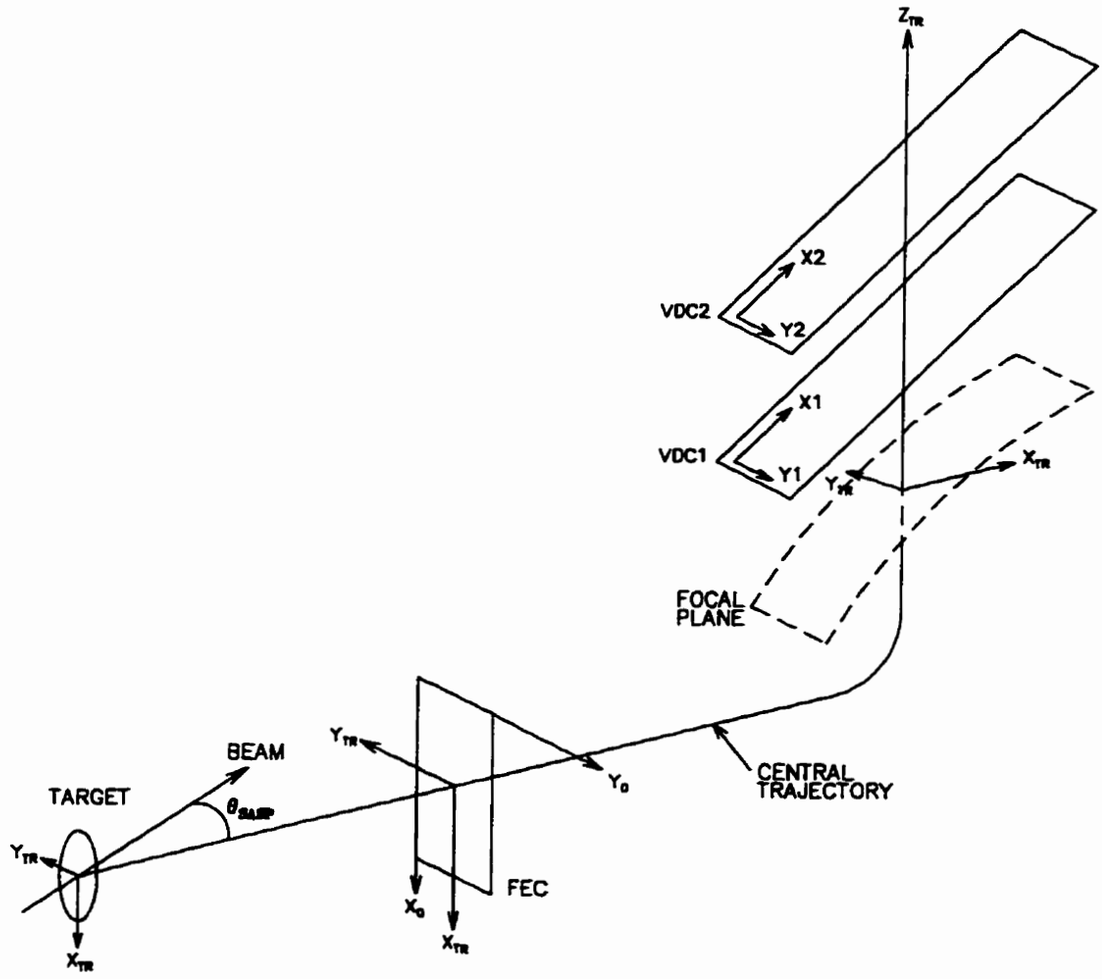

Figure 2.13: The points of interest, and their coordinate systems, along the SASP particle path.

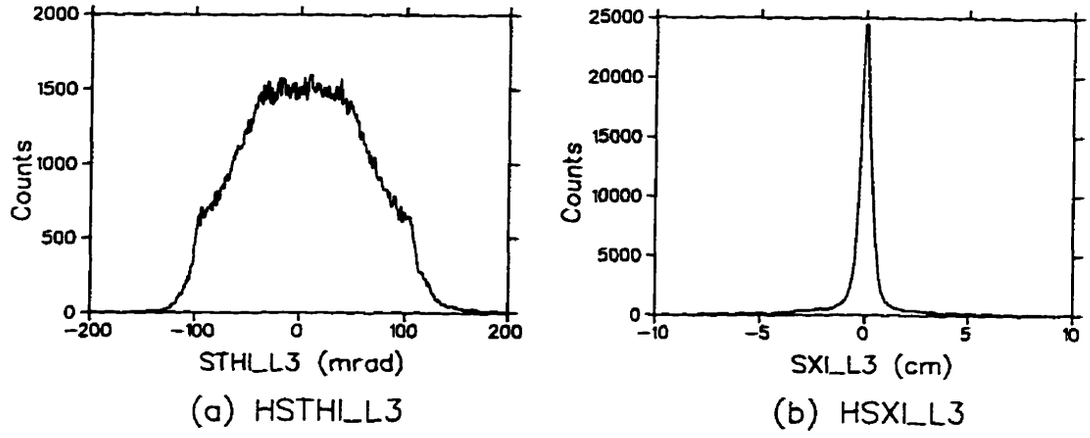

Figure 2.14: NOVA histograms of the target coordinates STHI_L3 (a) and SXI_L3 (b). The target position was calculated from the target angle and the X coordinate at the FEC.

where (SFEC0DIST-0.64) is the distance, in cm, from the target to the FEC X plane. Figure 2.14(b) shows a typical distribution of SXI_L3. In order to remove obvious non-pions from the event stream, a cut was placed in the OPSEQ (appendix B) which selected events with $(-3.5 < SXI_L3 < 3.5)$.

SYI is the Transport Y coordinate at the target. SYI_F was calculated in USRF by a least squares fit involving LY0POS and the intersections of the particle path with VDC1 and VDC2. SYI_F is a substantial improvement over SYI_P, calculated from the focal plane coordinates alone, as shown in figure 2.15. However, our algorithm worked well only for events at the high momentum end of the focal plane, so there was no cut on SYI in the OPSEQ. Note that the width of the real y_i distribution would be the projection of the target's active area (see figure 2.10) in the SASP direction,

$$\Delta y_i \simeq \frac{t \sin\theta_{SASP}}{\cos\theta_{TARGET}}, \tag{2.11}$$

where t is the target thickness.

STHI is the particle path angle in the X-Z plane at the target in the Transport coordinate system. We calculated our first approximation of STHI from the focal plane

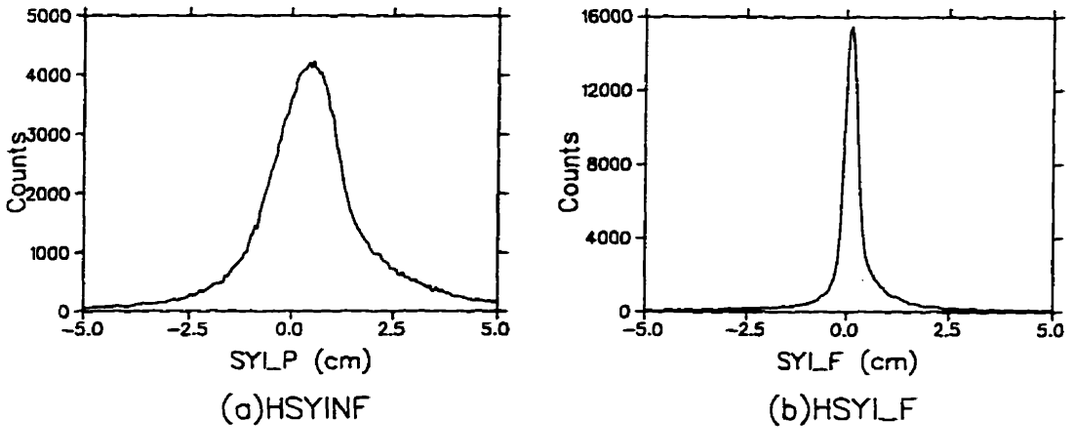

Figure 2.15: NOVA histograms of the Y Transport coordinate at the target, calculated without (a) and with (b) FEC data.

angle STHFCN and the transfer matrix element (see section 2.3.3) which relates the two:

$$STHI_P3 = STHFCN/R22. \tag{2.12}$$

With corrections for SASP aberrations, as discussed in section 2.3.7, we obtained the more accurate STHI_L3. A typical histogram of STHI_L3 appears in figure 2.14(a). A cut was placed on STHI_L3, selecting (-100,100).

SPHI is the Y-Z plane angle at the target, in Transport units (milliradians). The most accurate version was called SPHI_P5. This came from taking SYI to be zero and using the FEC Y coordinate in the small angle approximation:

$$SPHI_P5 = -5.0 \times (LY0POS - LY0_CENT)/(SFEC0DIST + 0.64), \tag{2.13}$$

where (SFEC0DIST+0.64) is the distance from the target to the FEC Y plane, in cm (the -5.0 is a unit conversion factor). A cut on this coordinate selected (-50,50). Without the FEC, our first approximation to this quantity was calculated from SYF, using the transfer matrix element which theoretically relates the two:

$$SPHI_P3 = SYF/R34. \tag{2.14}$$

With corrections for SASP aberrations, this becomes SPHI_L3. Because this was less accurate than SPHI_P5, a less stringent cut was applied, selecting (-60,60).

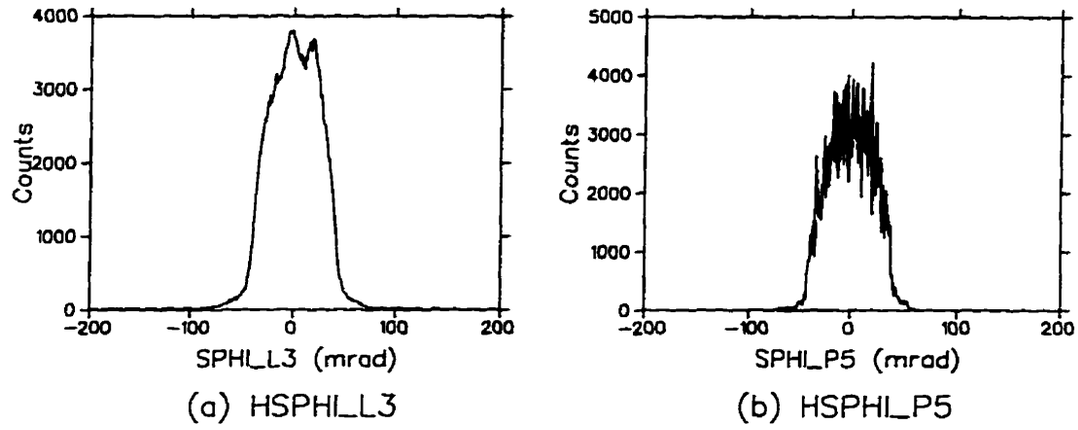

Figure 2.16: NOVA histograms of target angle ϕ_i, calculated from focal plane coordinates (a) and from FEC data (b).

Histograms of both calculations of ϕ_i are shown in figure 2.16.

LX0POS is the the coordinate denoted X_0 in figure 2.13, measured in 50 μm units. This is the quantity directly decoded from the FEC wire signals. Note that although LX0POS is in the same direction as its Transport counterpart, it has a different origin (the central trajectory has LX0POS=LX0_CENT) and units.

LY0POS is the coordinate denoted Y_0 in figure 2.13, measured in 50 μm units. In this system the central trajectory passes through the FEC at LY0POS = LY0_CENT. Note that LY0POS has the opposite direction to the Transport convention.

SX0_TR is the bend plane Transport coordinate at the FEC. It is calculated

$$SX0_TR = (LX0POS - LX0_CENT) \times 0.005. \tag{2.15}$$

SY0_TR is the non-bend plane Transport coordinate at the FEC. It is calculated

$$SY0_TR = -(LY0POS - LY0_CENT) \times 0.005. \tag{2.16}$$

LX1POS is the distance in the X direction in VDC1 (this is X1 in figure 2.13), in 50 μm units.

LU1POS is the distance in the U direction (see figure 2.17) in VDC1, in 50 μm units.

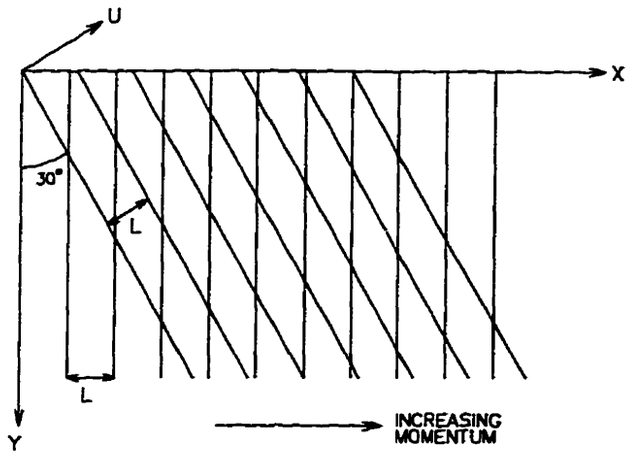

Figure 2.17: A schematic showing the orientation of the VDC X and U wires.

LY1POS is the distance in the Y direction in VDC1 (this is Y1 in figure 2.13), in 50 μm units. There are no wires in the VDC that directly give the Y1 coordinate; it is calculated from LX1POS and LU1POS

$$LY1POS = \sqrt{3} \cdot LX1POS - 2 \cdot LU1POS. \tag{2.17}$$

LX2POS is the distance in the X direction in VDC2 in 50 μm units.

LU2POS is the distance in the U direction in VDC2 in 50 μm units.

LY2POS is the distance in the Y direction in VDC2 in 50 μm units, calculated in the same way as LY1POS.

SXF is the point where the particle trajectory intersects the SASP focal surface, in the Transport X coordinate (the origin of the focal plane Transport system is approximately the intersection point of the central trajectory with the focal surface, which is discussed in detail in section 2.3.2). A plot of SXF appears in figure 2.18(a). Note the sharp peak corresponding to the $pp \rightarrow d\pi^+$ reaction at the high end of the focal plane.

SYF is the Transport Y coordinate at the SASP focal plane. An SYF distribution is shown in figure 2.18(b).

Selected SASP Dimensions		
SFEC0DIST		56.0394 cm
LX0CENT		1620×50μm
SY0CENT		740×50μm
The following are measured along Z_{TR}:		
Focal surface to:	X1	2.66 cm
	U1	6.97 cm
	X2	58.38 cm
	U2	62.69 cm

Table 2.5: Some of the SASP dimensions used in calculating coordinates.

SZF is the Transport Z coordinate at the SASP focal plane.

STHF is the angle in the *bend plane* (X-Z) at the focal plane, in Transport units. The NOVA coordinate is called STHFCN, which has been offset such that STHFCN=0 for θ_i=0. In fact, the offset value THOFF used in our analysis was slightly incorrect [16], but this inaccuracy was provided for in the aberration correction function USRL. An STHF distribution is shown in figure 2.18(c). A cut was placed on this coordinate, selecting (-200,200).

SPHF is the angle in the *non-bend plane* (Y-Z) at the focal plane, in Transport units. A typical SPHF distribution is shown in figure 2.18(d). Note that the non-bend plane angle of a particle path should not increase from between the target and focal plane.

The calculation of the focal plane coordinates is discussed in section 2.3.2.

2.3.2 Focal plane

The focal plane is the locus of points for which the position in the bend plane direction is independent of the bend plane angle at the target. In the coordinates introduced in

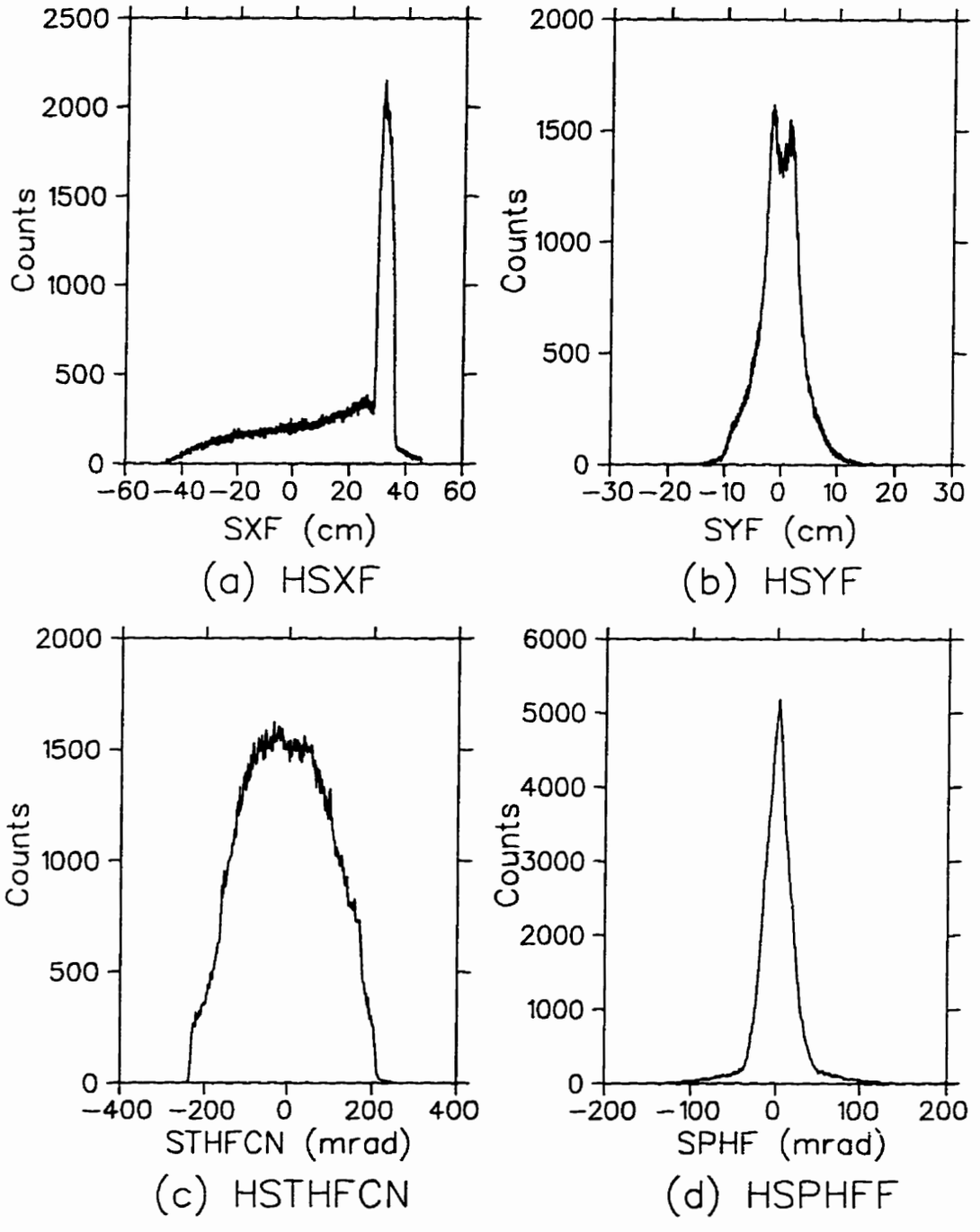

Figure 2.18: NOVA histograms of particle coordinates at the SASP focal plane.

section 2.3.1, this is to say that for any particular particle track, SXF is independent of STHI, and so all of the particles of a given momentum and SXI intersect the focal plane at the same SXF. Thus, the focal plane position is a function of the momentum of the particle and its initial position SXI.

The focal surface is curved and lies just below VDC1. The focal surface has been parameterized in terms of a coordinate system originating at LX1POS = 0, as shown in figure 2.19. In this system X=LX1POS and Z is perpendicular to X, pointing towards VDC2. In these coordinates the focal plane is described by the polynomial

$$Z_{FP} = a_0 + a_1 X_{FP} + a_2 X_{FP}^2 + a_3 X_{FP}^3 + a_4 X_{FP}^4 \tag{2.18}$$

where the coefficients have been empirically determined [17].

An arbitrary ray intersects VDC1 at X_1 and VDC2 at X_2, where

$$X_2 = LX2POS + X2OFF. \tag{2.19}$$

These two points define a line

$$Z = mX + b \tag{2.20}$$

where

$$m = \frac{SVDCDIST}{X_2 - X_1} \text{ and } b = -mX_1. \tag{2.21}$$

Combining equations 2.18 and 2.20 leads to the fourth order polynomial in the focal surface intersection point X_I,

$$mX_I + b = a_0 + a_1 X_I + a_2 X_I^2 + a_3 X_I^3 + a_4 X_I^4. \tag{2.22}$$

The valid root of this equation is found using the Newton-Raphson numerical method, in the userfunction (for more about userfunctions, please see section 2.3.6) USR9.

The resultant intersection points X_I and Z_I are then converted into the the Transport coordinate SXF by a 45° rotation, a translation $-\vec{R}_0$, and a multiplication by a factor to convert from 50μm units to centimetres. The origin of the focal plane Transport coordinate system is very nearly the point of intersection of the central trajectory with the focal surface - for historical reasons it is slightly displaced, in Z_{TR}, from the intersection point.

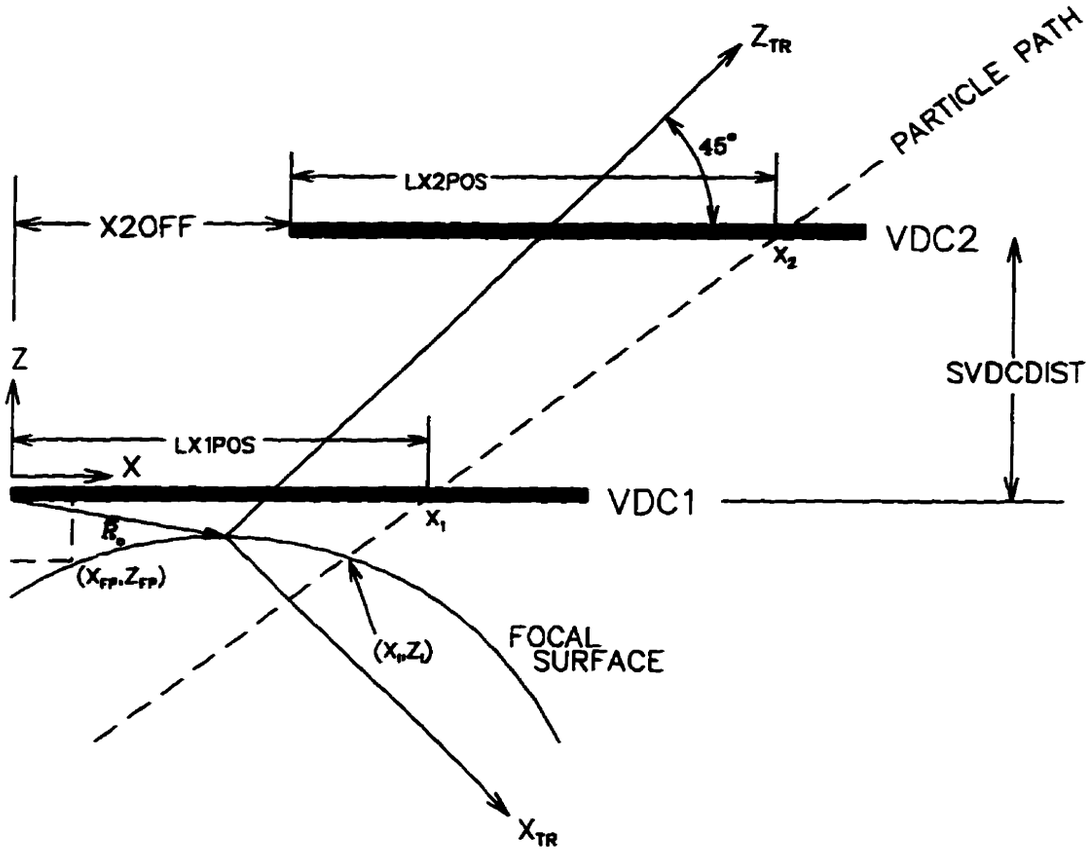

Figure 2.19: Schematic of the SASP focal plane and VDCs, also showing the Transport coordinate system and an arbitrary particle trajectory

Earlier calibration has related SXF to the momentum deviation δ through the polynomial

$$SDEL_9 = a_0 + a_1 SXF + a_2 SXF^2 + a_3 SXF^3 + a_4 SXF^4. \tag{2.23}$$

SDEL_9 was our initial approximation (calculated in USR9) to δ, which is the deviation of the particle momentum from the spectrometer's central momentum p_o, defined

$$\delta = \frac{p - p_o}{p_o} \times 100\%. \tag{2.24}$$

The central momentum is determined by the SASP magnetic field: $p_o = 49.97 \cdot B_{SASP}$, where p_o is in MeV/c and B_{SASP} is the dipole field in kG and calculated from an NMR probe measurement 15" from the centre of the field.

Once Z_I has been determined, obtaining SYF is comparatively simple. Defining a Y coordinate to complete the X and Z chosen above, we can define a line in the Y-Z plane using the measured VDC intersections Y_1 and Y_2. The intersection of this line with the focal surface at Z_I gives the coordinate Y_I, which is then converted to Transport coordinates.

2.3.3 Transfer matrix

The focal plane coordinates of a given particle are a function of the coordinates of that particle at the target. To first order, this relationship is given by the transfer matrix [18], in the vector equation

$$\begin{array}{ccccc} \textit{particle at} & & & & \textit{particle at} \\ \textit{focal plane} & & \textit{transfer matrix} & & \textit{target} \end{array}$$

$$\begin{pmatrix} x_f \\ \theta_f \\ y_f \\ \phi_f \\ l_f \\ \delta_f \end{pmatrix} = \begin{pmatrix} R_{11} & 0 & 0 & 0 & 0 & R_{16} \\ R_{21} & R_{22} & 0 & 0 & 0 & R_{26} \\ 0 & 0 & R_{33} & R_{34} & 0 & 0 \\ 0 & 0 & R_{43} & R_{44} & 0 & 0 \\ R_{51} & R_{52} & R_{53} & R_{54} & R_{55} & R_{56} \\ 0 & 0 & 0 & 0 & 0 & R_{66} \end{pmatrix} \begin{pmatrix} x_i \\ \theta_i \\ y_i \\ \phi_i \\ l_i \\ \delta_i \end{pmatrix} \qquad (2.25)$$

where x, θ, y and ϕ are the geometrical coordinates introduced in section 2.3.1. The Transport conventions apply to all coordinates. l is the deviation of path length from that of the central trajectory; this coordinate was not used in E633 analysis. δ is the momentum deviation introduced in equation 2.24.

The full 6×6 transfer matrix is simplified by elementary spectrometer properties. To first order, bend plane coordinates x and θ and non-bend plane coordinates y and ϕ are decoupled. Since the energy of the particle should not be changed by the static magnetic fields of the spectrometer, the R_{66} element is set to unity, so $\delta = \delta_i = \delta_f$. The focal plane is defined such that the final position in the bend plane x_f is a function of target position x_i and momentum δ and is independent of target angle θ_i; for particles of a given momentum, there is a point-to-point focus in X. Finally, to first order, the non-bend plane coordinates (y_f, ϕ_f) are independent of momentum δ.

For SASP, the first order transfer matrix elements are not constant across the focal plane, but can be empirically parameterized in δ [17]. The calculation of the matrix elements was carried out in the NOVA userfunction USRE. Equation 2.26 shows the matrix element values for $\delta = 0$.

$$\begin{pmatrix} x_f \\ \theta_f \\ y_f \\ \phi_f \\ l_f \\ \delta_f \end{pmatrix} = \begin{pmatrix} 0.815 & 0.0 & 0 & 0 & 0 & 2.682 \\ 2.699 & -1.775 & 0 & 0 & 0 & 5.405 \\ 0 & 0 & -3.978 & -0.176 & 0 & 0 \\ 0 & 0 & -12.28 & -0.790 & 0 & 0 \\ R_{51} & R_{52} & R_{53} & R_{54} & R_{55} & R_{56} \\ 0 & 0 & 0 & 0 & 0 & 1 \end{pmatrix} \begin{pmatrix} x_i \\ \theta_i \\ y_i \\ \phi_i \\ l_i \\ \delta_i \end{pmatrix} \tag{2.26}$$

2.3.4 Dispersion

Equation 2.25 in section 2.3.3 defines how the focal plane position x_f is a function of target position x_i and momentum δ through the spectrometer's *magnification* M

$$M = \left.\frac{\partial x_f}{\partial x_i}\right|_{\delta=const} = R_{11} \tag{2.27}$$

and its *dispersion* D

$$D = \left.\frac{\partial x_f}{\partial \delta}\right|_{x_i=const} = R_{16}. \tag{2.28}$$

Since the spectrometer measures momentum through the focal plane position, it follows that momentum resolution is limited by the size, in x_i, of an achromatic beamspot.

This limitation can be overcome by using *dispersed* beam, in which there is a linear correspondence between the spread of the beam in position, Δx_i, and the momentum spread of the beam protons, $\Delta\delta$. The coefficient of dispersion, expressed in cm/%, is selected to minimize the spread in x_f:

$$\begin{aligned} \Delta x_f &= R_{11}\Delta x_i + R_{16}\Delta\delta = 0, \\ \Rightarrow \frac{-R_{16}}{R_{11}} &= \frac{\Delta x_i(cm)}{\Delta\delta(\%)} \\ \text{and } \frac{-R_{16}}{R_{11}} &= -D/M. \end{aligned} \tag{2.29}$$

From table 2.4 in section 2.3, D/M = 4.7 cm/% at the central momentum. However, it is the momentum spread of the pions at the target which must be used, not that of the

beam protons, so the beam dispersion required is

$$\frac{\Delta x_i(cm)}{\Delta\delta(\%)} = -4.70 \times \frac{\Delta p_\pi/p_\pi}{\Delta p_p/p_p}. \tag{2.30}$$

Therefore the desired dispersion depends upon the kinematics of the pion production. For the reaction $pp \rightarrow d\pi^+$ under the conditions of E633, the calculated beam dispersion requirement ranged from -13.5 cm/% to -17.4 cm/% at 420 MeV, and from -10.7 cm/% to -11.8 cm/% at 500 MeV, and so the maximum available dispersion, -11 cm/%, was used. Our measured momenta showed no x_i dependence, so dispersion matching was successful in reducing this momentum resolution limitation to below the level of others (such as variation in energy loss in the target, discussed in section 2.2.1).

2.3.5 Event trigger

Of the many events which register in the various SASP detectors, combinations of detector signals which might indicate an event of interest are selected at the hardware level by the SASP trigger. ECL programmable electronics enable the experimenter to adjust trigger conditions while an experiment is running, and the the trigger definition terms are accessible in NOVA, the online control and analysis program used by the SASP group and others at TRIUMF (for more about NOVA, please see section 2.3.6). Events selected by the trigger are written to tape, and as many as possible are also analyzed online.

Selecting a good trigger involves balancing two considerations: one wishes to record all events which are possibly valid; but since there is a technical limit to the rate at which data can be recorded it is also desirable to trigger on as little 'junk' as possible.

For E633 the trigger was defined, in NOVA terms,

```
LEVENT        I*4 Var    0
  (BIT5|BIT7)*((LES1&LEPADL)&LEX1)
LSLOWAUX      I*4 Param  1 .
```

LEVENT is also called the 'top-end event' definition. Reading from right to left, the event definition requires a signal from the VDC1 X plane (LEX1), one or more focal plane scintillator paddles (LEPADL), and the S1 scintillator (LES1)(see figure 2.12).

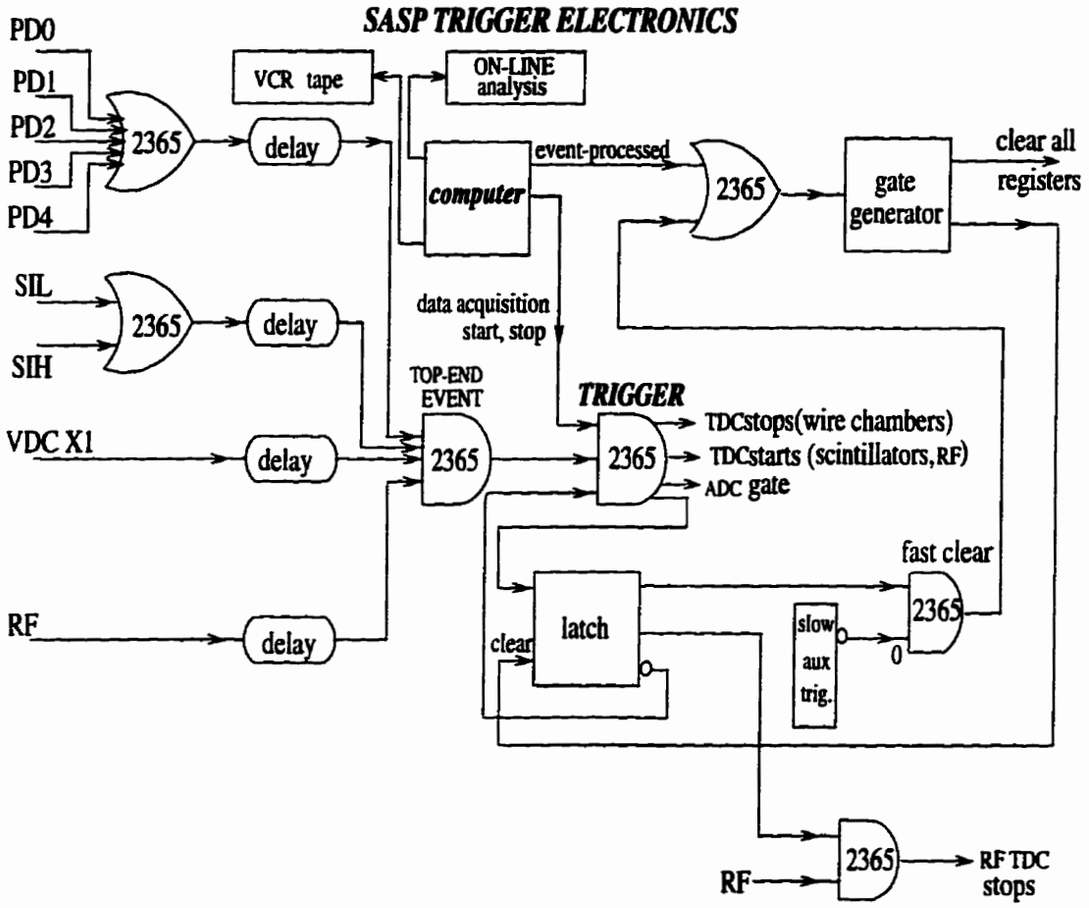

Figure 2.20: A schematic diagram of the trigger electronics. Adapted from [7]. At the upper left are the input signals which comprise the event trigger: the scintillator paddles PDn; the two photomultipliers of the large S1 scintillator; and the VDC X1 plane.

A schematic of the trigger electronics is shown in figure 2.20. This diagram shows, at the left, the VDC X1, an OR of the two S1 photomultipliers (one at each end of S1). and an OR of the five focal plane scintillator paddles PDn. These signals comprise the input AND gate which defines the top-end event. Then, if acquisition is enabled and the electronics are not busy, the data acquisition electronics are triggered.

LSLOWAUX is a trigger component normally using signals from the front end chamber—usually an OR of the two FEC planes—to further 'clean up' the signal by fast-clearing top end events when they do not pass the front end condition. In E633 front end information was not used in the trigger: LSLOWAUX was set to 1, which (after inversion, as shown in the diagram) inhibits the fast clear. The front end chamber was not used because there was initial doubt about its efficiency. In fact the FEC appears to have been efficient and reliable, when it was plugged in (see section 2.4 to find out when this was not the case).

Time of flight

As discussed in section 2.3.2, the momentum of a particle is a function of its measured focal plane X position—SXF in Transport coordinates. The velocity of a particle of a given momentum is a function of its mass. Therefore velocity, as a quantity distinct from momentum, is useful for particle identification, which is discussed in detail in section 2.3.8. There are two ways of obtaining velocity with SASP, through determination of the particle's time of flight through the spectrometer. This is not exactly a measurement of velocity, since the length of a particle's path through the spectrometer is a function of its momentum and the dipole field setting, but it is close enough for particle identification purposes.

An absolute time of flight is obtained by measuring the delay between a signal from the Front End Chamber and a signal from a top end detector. This method is reliable but not precise, since the wire planes of the front end chamber do not give sharp signals in time. The time of flight determined using the FEC and the focal plane scintillator paddles, was called LTOF. LTOF did not have sufficient resolution for particle identification in E633.

A relative time of flight is obtained by measuring the time from a valid focal plane

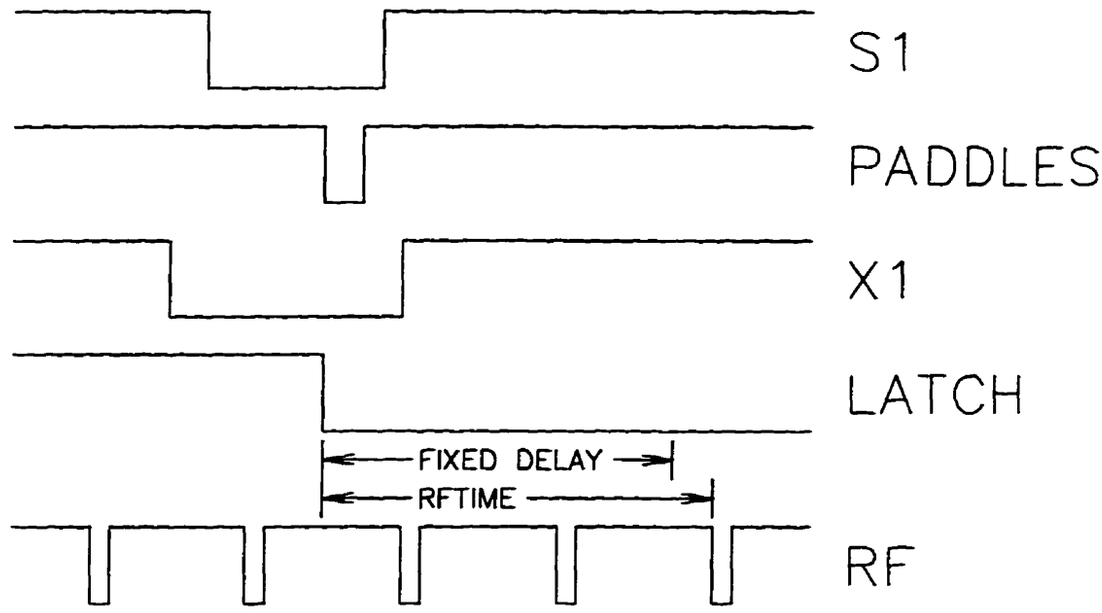

Figure 2.21: Schematic of signal timing from X1, the Paddle OR, S1, and the RF pulses. The delay shown represents various delays applying to the Latch signal and the RF pulses.

scintillator paddle hit to an RF timing pulse. RF pulses come from cyclotron control with the frequency of beam bursts, *i.e.*, every 43 nanoseconds. This method is illustrated in figure 2.21. The diagram shows the three signals which form the event trigger: VDC X1, scintillator S1, and Paddle OR. The chronology is representative, not exact. The Paddle OR signal is the most precise of the three (because X1 is a wire chamber and S1 is a very large scintillator) and therefore it is delayed in the electronics to be the last to start. Thus, the beginning of the trigger signal is determined by the time of a paddle hit.

The event trigger starts a TDC device to begin timing. The TDC is stopped by the next RF pulse, after a fixed period which keeps a clear separation between the end of the trigger/start pulse and the beginning of the RF/stop pulse. This delay could be changed during an experiment to accomodate shifts in the relative timing of events and RF pulses. Although the absolute time measured, called LRFTIME in NOVA, is meaningless, the *relative* timing of different events can be determined in this way. Note

that slower particles have later trigger starts and hence lower LRFTIME; faster particles have higher LRFTIME. Resolution in LRFTIME was approximately eight times that of LTOF.

2.3.6 NOVA

Once the raw output from the SASP and beamline detectors has been shaped into a data stream, it is written to tape. A fraction of it—how much depends upon computer live time—is also analyzed online using Peter Green's NOVA analysis program [20].

NOVA carries out an OPeration SEQuence (OPSEQ) on each event. The OPSEQ is a program of condition and variable evaluations and histogram incrementations. The OPSEQ used for E633 online analysis appears in Appendix B. Conditions, variables, parameters and histograms can be defined and the OPSEQ itself rewritten in the NOVA environment while the experiment is running, enabling experimenters to examine and test their data as it is created.

NOVA can also call *userfunctions*—subroutines (typically, though not necessarily. written in Fortran) which calculate quantities whose definitions are fixed. For example USR1 calculates the VDC and FEC chamber coordinates (LX1POS, LY2POS, etc.) from the wire signals and various chamber parameters.

In addition to real data events which consist of a set of SASP detector data, *scaler* events are periodically generated. Scaler events consist of run statistics such as number of hits in particular wire planes and scintillators, and beam monitoring statistics from the IBP and SEM. NOVA shapes this information into rates (counts per second) and running totals. Online, the scalers provide quick insight into the state of the beam and the spectrometer activity. Offline, beam statistics are used for current normalization, polarization corrections, and so forth. Unlike data events, all scaler events are analyzed online.

Offline, NOVA is also used, and since speed is less important, much more data processing—more histograms, more userfunctions, etc.— is possible. In the offline analysis, almost all of the numerical quantities of interest which do not come directly from the electronics are calculated in userfunctions. Figure 2.22 is a flowchart of these routines, showing how they interact. USR1 calculates the chamber hit coordinates, USR9

calculates focal plane Transport coordinates (section 2.3.2), USRE calculates the elements of the first order transfer matrix (section 2.3.3), USRP calculates, to first order, the target Transport coordinates (section 2.3.1). Other userfunctions are discussed in the appropriate sections.

2.3.7 Coordinate corrections

VDC X2 gap

In E633 there was an unexplained problem in the X wire plane of VDC2. Figure 2.23(a) shows a gap in a segment of the LX2POS distribution. Since an X2 coordinate is required for calculating focal plane position, this gap was causing otherwise valid events (in the $\delta \sim 12\%$ region) to be disqualified. The solution was to generate X2 events in the gap when X2 was missing and there was a U2 event in a corresponding range. A probability was introduced so the X2 efficiency in the gap region would be consistent with regions to either side. The userfunction USRK implemented this solution, whose effect can be seen in Figure 2.23(b).

Trajectory angles at the target

Reconstruction of the reaction requires the two components of the scattering angle: the bend plane target angle θ_i and the non-bend plane target angle ϕ_i.

When the FEC is used, equation 2.13 gives SPHI_P5, the most accurate determination of ϕ_i. When the FEC is not used, a first approximation can be made to ϕ_i using the transfer matrix and the non-bend plane coordinate at the focal plane (equation 2.14). This is called SPHI_P3. Note that equation 2.14 is not a full 2 X 2 inversion of the non-bend plane elements of the transfer matrix. Though this is required in principle, it turns out to be less accurate in practice.

The bend plane target angle could not be calculated from FEC data. Because a dispersed beam about 2 cm high was used, the beam spot could not be considered point-like in x_i. Thus it is necessary to carry out the partial transfer matrix inversion to obtain STHI_P3 as defined in equation 2.12.

Inaccuracies in both STHI_P3 and SPHI_P3 arise from optical aberrations in the

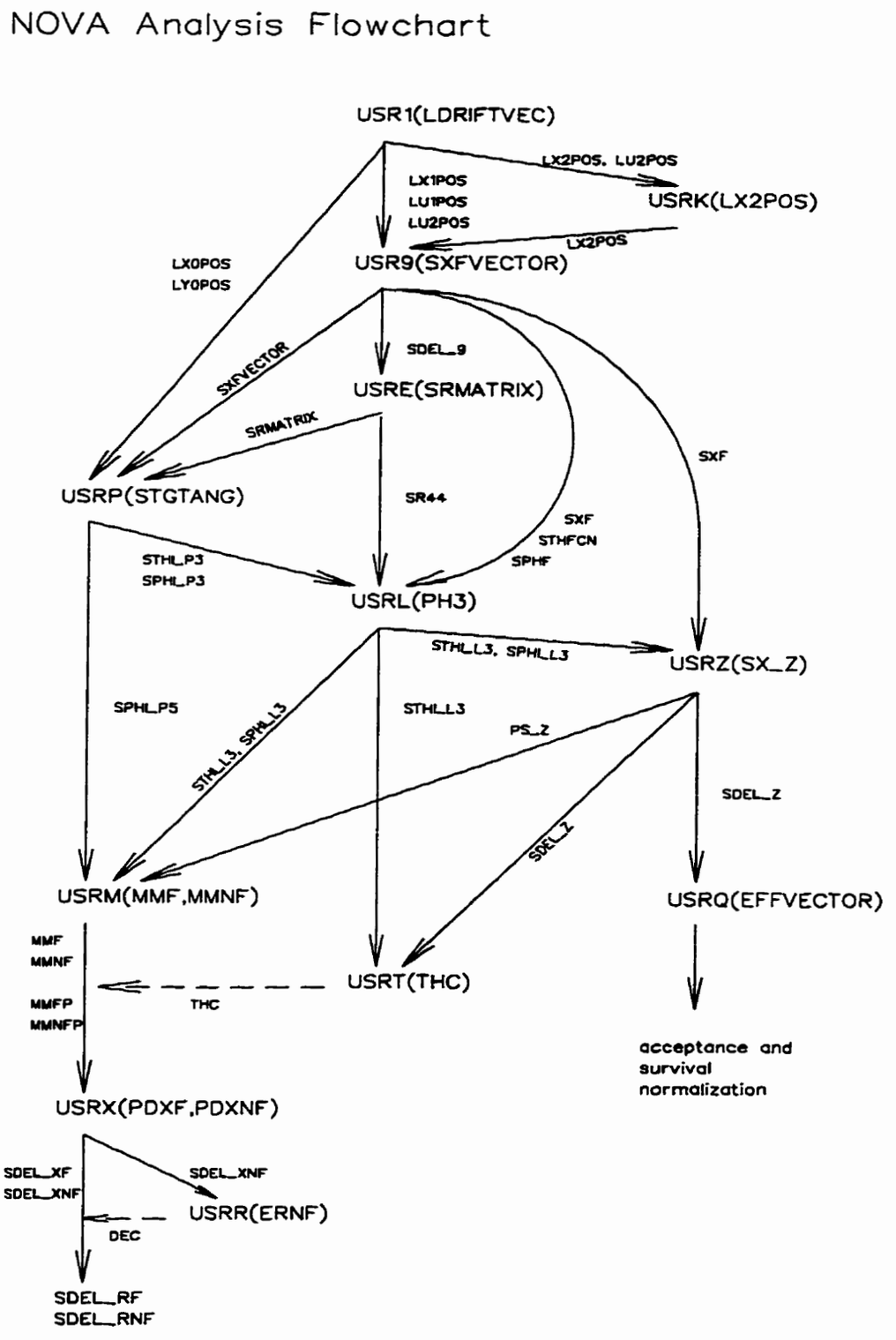

Figure 2.22: The NOVA userfunctions of E633 data analysis.

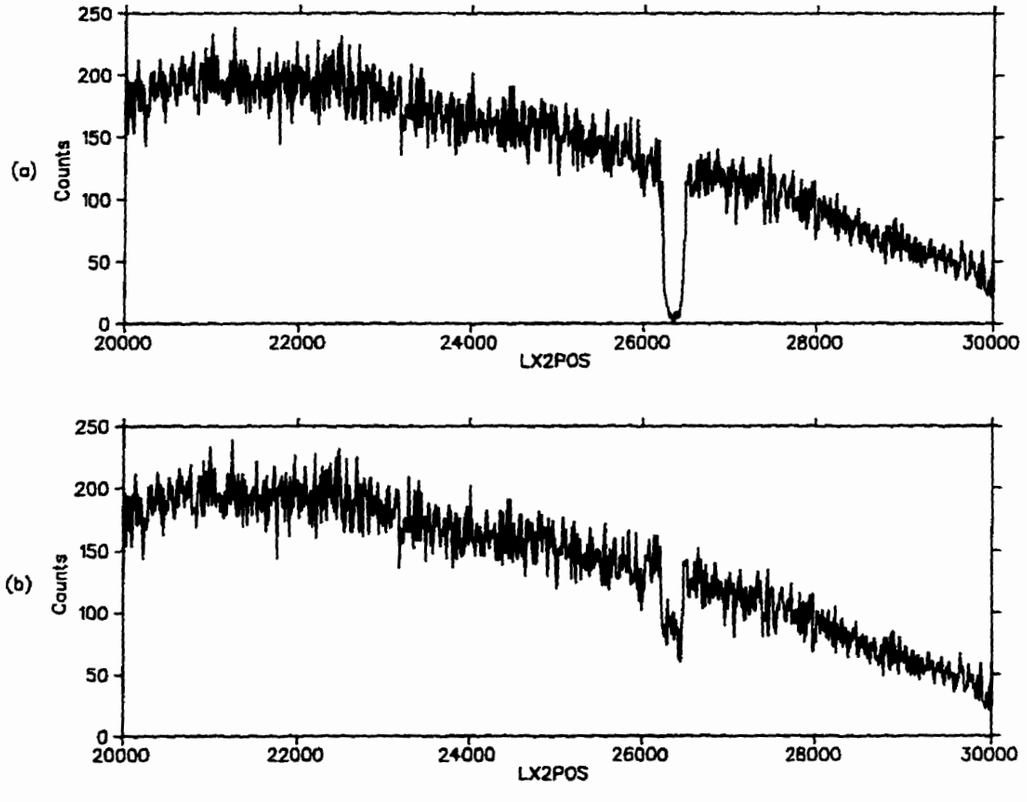

Figure 2.23: A selected region of LX2POS, showing the gap (a), and (b) the same region after 'filling'.

spectrometer which distort focal plane coordinates. The effect of these aberrations has been parameterized in θ_f, for θ_i, and in θ_f and δ, for ϕ_i. For a detailed explanation, please see reference [7]. The corrected angles, STHI_L3 and SPHI_L3, were calculated in USRL. The improvement in SPHI is shown in figure 2.24, where one sees the much better correlation between SPHI_P5 (the most accurate approximation to ϕ_i available) and SPHI_L3.

Focal plane position

The resolution of the focal plane position SXF, and hence also the momentum, is also affected by optical aberrations. Corrections have been calculated [7] and take the form

$$SXFC = SXF - C_0 - C_1\theta_i - C_2\theta_i^2 - C_3\theta_i^3 - C_4\theta_i^4 - C_5\theta_i^5 \qquad (2.31)$$

where θ_i is the STHI_L3 discussed earlier. This correction is implemented in USRZ, and also provides the corrected momentum deviation SDEL_Z.

2.3.8 Particle identification

It was desirable during the experiment and, of course, essential for later analysis to identify the pions within the stream of other particles passing through the spectrometer. namely protons, deuterons, muons and positrons.

A simple criterion for selection, which can be applied early in the analysis with little use of processor time, is time of flight. Protons and deuterons, from elastic scattering and $pp \rightarrow d\pi^+$, respectively, have very different flight times than pions, in the momentum range of E633 (in any case, such protons and deuterons would have insufficient kinetic energy to reach the end of the spectrometer). Much closer times of flight may be expected for muons from pion decay, $\pi^+ \rightarrow \mu^+\nu_\mu$ and positrons from the further decay $\mu^+ \rightarrow e^+\nu_e\overline{\nu_\mu}$. Still, for the majority of momentum settings, these other particles should be distinguishable in time, provided the decay(s) occurred in or near the target. The issue of pion decay within the spectrometer itself is discussed in section 2.3.10.

Figure 2.25 shows an example of how relative flight time (LRFTIME, introduced in section 2.3.5) distinguishes pions from muons and positrons, in the particle identification spectrum HSPID. The width of each locus in LRFTIME is due to the range of momenta

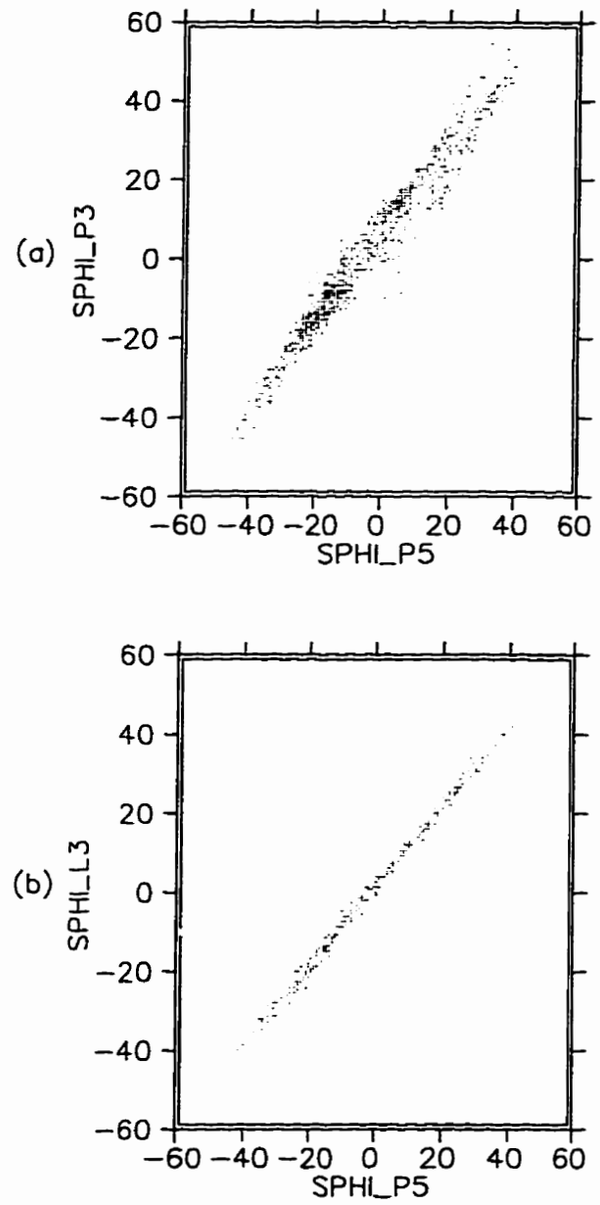

Figure 2.24: Correlation plots of ϕ_i calculated from focal plane coordinates versus ϕ_i with FEC coordinates, where the former is calculated without (a) and with (b) aberration corrections.

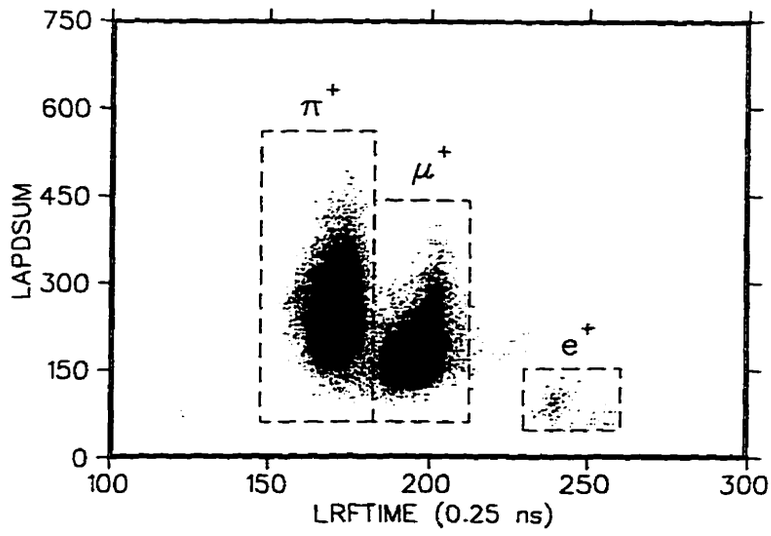

Figure 2.25: HSPID: a particle identification spectrum showing pion, muon and positron loci, distinguishable by their different timing. LAPDSUM is the sum of scintillator paddle signals for the event, which is an indication of ionization in the scintillator array.

(and hence times of flight) within it. The length of the proton beam pulse makes a smaller contribution.

For the same momenta, pions, muons and positrons will lose different amounts of energy in matter. Therefore the summed signals from the focal plane scintillator paddle array, LAPDSUM, is also used in particle identification. It is not a precise measure, however, and cuts in this quantity were loose. Figure 2.26 shows how pions were expected to vary in relative time of flight and, proportionally, in LAPDSUM, across the range of pion energies of E633. With the calculations represented by figure 2.26 for the pions and muons (positron time of flight is effectively constant across our momentum range), the pion locus could normally be 'tracked' across HSPID for successive measurements involving incrementally lower momentum ranges.

Three difficulties involving this kind of particle indentification which appeared in E633 will be briefly discussed:

Firstly, SASP Paddle 0 had lower gain than the other paddles. Consequently LAPDSUM tended to be low for particles of the lowest momenta at each setting. It is

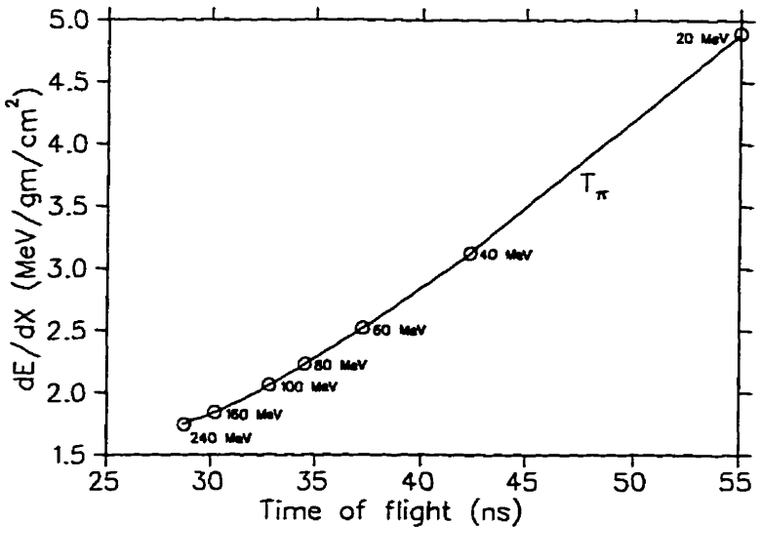

Figure 2.26: A plot of calculated pion characteristics in the SASP spectrometer. Pions of higher kinetic energy have smaller flight times and lose less energy in the scintillator material.

possible, though there is no direct evidence for it, that events have been lost because some Paddle 0 events did not pass a low end hardware cut.

Secondly, SASP Paddle 4 had different timing than the other paddles, by approximately -27 LRFTIME units (or about 7 ns). Since LRFTIME is defined by the timing difference between a Paddle signal and a later RF pulse, this initially caused loci in HSPID to have small 'doubles' which were, in fact, the high momentum part of the groups. The adopted correction was to simply subtract 27 from LRFTIME for paddle 4 events.

Thirdly, it will be recalled from figure 2.21 on page 37 that LRFTIME provides the timing of an event relative to the cyclotron RF pulse. For all events for which the event time plus the fixed delay is *coincident* with the RF (TDC stop) pulse, the LRFTIME will be equal to the delay (which is, ideally, adjusted to prevent this occurence). In some E633 runs, the timing of the pion locus was accidentally allowed to reach the edge of the timing window represented by two consecutive RF pulses. It will be observed that very late events will move into the next window and thus 'wrap around' to high LRFTIME, but there will be some intermediate events which 'pile up' around the minimal

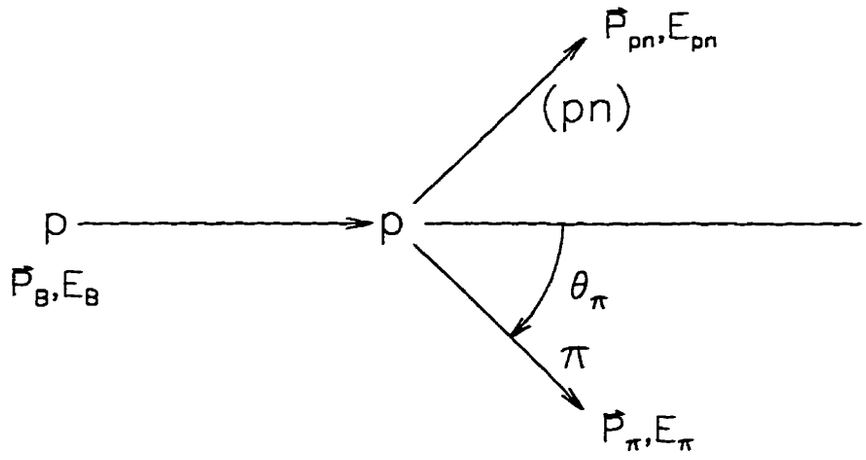

Figure 2.27: Schematic of the general $pp \rightarrow pn\pi^+$reaction. Vectors represent the incident beam proton, the scattered pion, and the recoil proton-neutron system.

LRFTIME. This can make it difficult or impossible to distinguish loci.

Additional particle identification insight could sometimes be gained by examining particle path traceback to the target (particles which were produced in a post-target decay may not trace back to the beamspot), and by examining the delta spectra of the different HSPID loci (different particles will have different survival fractions at the focal plane, resulting in different overall spectrum shape). These methods were occasionally of value in E633 analysis. The subtraction of those muons whose HSPID locus substantially overlapped that of the pions is discussed in section 3.1.2.

2.3.9 Missing mass

Calculation

Figure 2.27 is a presentation of the general $pp \rightarrow pn\pi^+$ reaction, where a single momentum vector $\vec{P}_{pn}$ represents the combined proton-neutron system. This reaction conserves momentum

$$\vec{P}_B = \vec{P}_{pn} + \vec{P}_\pi \tag{2.32}$$

and total energy

$$E_B + m_p = E_{pn} + E_\pi. \tag{2.33}$$

Rearranging these equations for the variables of the pn system gives

$$\vec{P}_{pn}=\vec{P}_B - \vec{P}_\pi \tag{2.34}$$

and

$$E_{pn} = E_B + m_p - E_\pi, \tag{2.35}$$

and the general expression for its invariant mass is

$$\mathcal{M}^2 = E_{pn}^2 - P_{pn}^2. \tag{2.36}$$

Here, $\mathcal{M}$ — the 'missing mass' of the undetected pn system — is the mass of the recoil particle(s) plus the internal energy of the system. In the two body case, $pp \rightarrow d\pi^+$, $\mathcal{M}$ is just m_d. Substituting equations 2.34 and 2.35 into equation 2.36 gives

$$\begin{aligned} \mathcal{M}^2 \;=\; & E_B^2 + m_p^2 + E_\pi^2 + 2m_pE_B - 2E_BE_\pi - 2m_pE_\pi + \\ & 2\,\vec{p}_B \cdot \vec{p}_\pi - p_p^2 - p_\pi^2 \end{aligned} \tag{2.37}$$

which can be expressed more simply as

$$\mathcal{M}^2 = 4m_p^2 + m_\pi^2 + 2m_pT_B - 2(T_B + 2m_p)E_\pi + 2p_Bp_\pi \cos\theta_\pi, \tag{2.38}$$

where T_B is the incident beam kinetic energy, and θ_π is the angle between the beam axis and direction of the scattered pion. To obtain the value $\cos\theta_\pi$, consider the scalar product of unit vectors along the pion and beam axes. Figure 2.28 shows how the Transport cartesian coordinate system (X_{TR},Y_{TR},Z_{TR}) applies to the SASP central trajectory beyond the target (but before bending in the dipole). In this system, the unit vector of a particular pion path is

$$\vec{R}_\pi = \frac{\tan\theta_i\hat{x} + \tan\phi_i\hat{y} + \hat{z}}{\sqrt{\tan^2\theta_i + \tan^2\phi_i + 1}} \tag{2.39}$$

and the unit vector along the beam path is

$$\vec{R}_B = \sin\theta_{SASP}\hat{y} + \cos\theta_{SASP}\hat{z}. \tag{2.40}$$

Now,

$$\vec{R}_\pi \cdot \vec{R}_B \equiv \mid \vec{R}_\pi \mid\mid \vec{R}_B \mid \cos\theta_\pi, \tag{2.41}$$

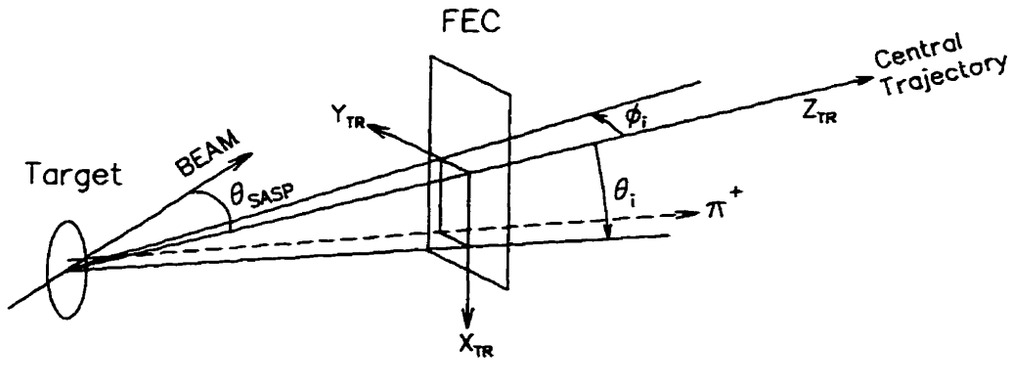

Figure 2.28: The Transport coordinates beyond the target. The Transport angles made by the beam and an arbitrary pion path with the central trajectory are shown.

therefore

$$\cos\theta_\pi = \frac{\tan\phi_i \sin\theta_{SASP} + \cos\theta_{SASP}}{\sqrt{\tan^2\theta_i + \tan^2\phi_i + 1}}. \tag{2.42}$$

It will be recalled from section 2.3.1 that the pion angles at the target are measured quantities: STHI_L3 is θ_i, in milliradians, and SPHI_P5 and SPHI_L3 are ϕ_i (calculated with and without FEC data, respectively), also in milliradians. Therefore with equation 2.42, missing mass could be calculated with equation 2.38, giving us MMF (using SPHI_P5) and a 'no FEC' version MMNF (using SPHI_L3).

Corrections

Small correlations were found between STHI_L3 and MMF. These were concluded to be due to a previously unconsidered optical aberration. The correlations appear as curvature in the locus of the pion peak from the two-body reaction, in plots of MMF versus STHI_L3, as shown in figure 2.29(a). The correlations varied in both momentum deviation δ and spectrometer dipole field B. Exact fits to the correlations were found at the momenta and field settings of the focal plane scan runs (see section 2.4 for details of the scans). Bilinear interpolation of these fits provided a correction term for missing mass. A corrected missing mass locus is shown in figure 2.29(b). The correction term THC was calculated in USRT;

$$MMFP = MMF - THC(\delta, \theta_i, B_{SASP}). \tag{2.43}$$

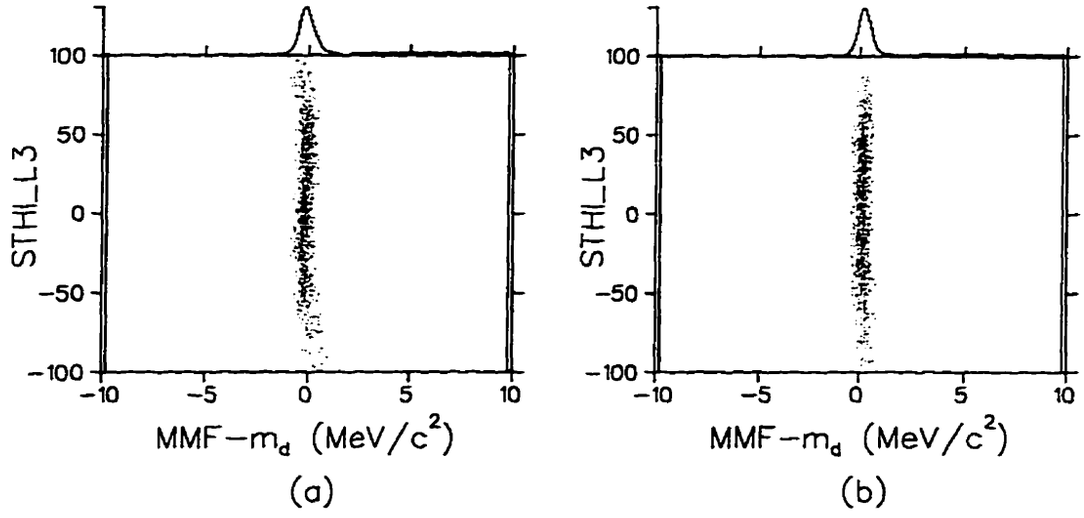

Figure 2.29: Plots of target angle STHI_L3 versus Missing Mass minus deuteron mass. Small correlations (a) are corrected by a set of aberration corrections (b).

The FECless missing mass, MMNF, had much lower resolution, and THC was not applied to it. MMNF was found to have, at some settings, a weak linear correlation with SPHI_L3. This is likely indicative of a flaw in the SPHI_L3 algorithm. MMNF was corrected with an *ad hoc* linear correction term.

Momentum extraction

After the θ_i aberrations were corrected, the pion momentum was re-extracted from the missing mass $\mathcal{M}$ by solving for pion momentum in equation 2.38, with the scattering angle set to the SASP angle. Then $\cos\theta_\pi$ becomes simply $\cos\theta_{SASP}$, and the pion momenta were shifted to the value they would have had at the nominal reaction angle. The useful solution of the quadratic equation

$$p_\pi = \frac{-B + \sqrt{B^2 - 4AC}}{2A} \tag{2.44}$$

where

$$\begin{aligned} A &= 4(T_B + 2m_p)^2 - 4p_B^2 \cos^2\theta_{SASP} \\ B &= -4p_B \cos\theta_{SASP}(4m_p^2 + m_\pi^2 + 2m_p T_B - \mathcal{M}^2) \\ C &= 4(T_B + 2m_p)^2 m_\pi^2 - (4m_p^2 + m_\pi^2 + 2m_p T_B - \mathcal{M}^2)^2 \end{aligned}$$

was obtained in USRX for both MMFP and MMNF, returning δ's SDEL_XF and SDEL_XNF.

Momentum re-extraction can fail when equation 2.38 produces an $\mathcal{M}$ which is unphysical for $\phi_i = 0$. For the beam energies and reaction angles of E633, this could occur at pion momenta largely outside our range of interest, and the number of events lost in this manner was inconsequential.

2.3.10 Acceptance and survival

Pion Survival

Recorded events were weighted by the pion survival fraction

$$SURV = \exp\left(-\frac{m_\pi c EFF_L}{P_\pi c\tau}\right), \tag{2.45}$$

where P_π is the pion momentum; $c\tau$ for the pion is 7.804 m. The SASP effective length for pions, EFF_L, was determined using a Monte Carlo program which considers the number of pions that decay through the length of the spectrometer. This effective length varies from approximately 8.3 m at 80 MeV/c to 7.6 m at 300 MeV/c, for a central trajectory and was further parameterized in terms of momentum deviation δ:

$$EFF_L = \begin{cases} A + B\delta + C\delta^2 + D\delta^3 + E\delta^4 + F\delta^5 & \delta \geq 0.0 \\ A + B\delta & \delta < 0.0 \end{cases} \tag{2.46}$$

where the coefficients A through F are functions of the pion momentum. The determination of the coefficients is discussed in detail in reference [15]. The survival fraction was calculated in userfunction USRQ, using the corrected momentum deviation SDEL_Z (introduced in section 2.3.7). Pion survival at several momentum ranges is plotted in figure 2.30.

NOVA histograms with results weighted by the pion survival factor, $\frac{1}{SURV}$, have the suffix _SN, as in HSDELFUP_SN.

SASP acceptance

SASP calibration scans were made using the $pp \rightarrow d\pi^+$ reaction at both 500 and 420 MeV, at the beginning and end of the data-taking period, respectively (see the Run

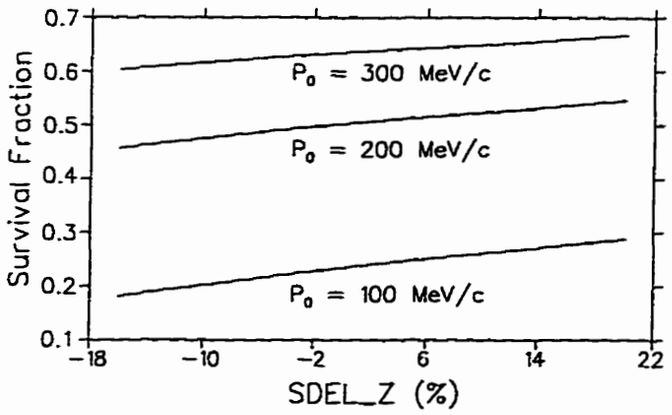

Figure 2.30: The pion survival fraction, plotted as a function of SDEL_Z, the deviation from the central momentum P_0.

Plan in section 2.4). The normalized cross sections derived for $pp \rightarrow d\pi^+$ are shown in figure 2.31. The cross sections were corrected for pion survival and the other factors discussed in section 3.1.1. A fit to this data provided the SASP relative acceptance as a function of momentum deviation SDEL_Z, and was calculated for each event by USRQ. NOVA histograms of events weighted with the pion survival and SASP acceptance factor, $\frac{1}{SURV \cdot ACC}$, have the suffix _AS.

2.3.11 Livetime

The computer livetime n_{live} is defined

$$n_{live} = \frac{latch}{event}, \tag{2.47}$$

where *event* is the number of events meeting the trigger definition, and *latch* is the number of events processed by the detector electronics (see section 2.3.5). Error in livetime is [21]

$$\varepsilon_{n_{live}} = \sqrt{\frac{n_{live}(1 - n_{live})}{event}}. \tag{2.48}$$

In E633, there were also event and latch counters gated by the beam spin state. Livetime calculated from these was a nearly linear function of event rate, as shown in figure 2.32. Livetime calculated from ungated scalers showed excursions from simple rate

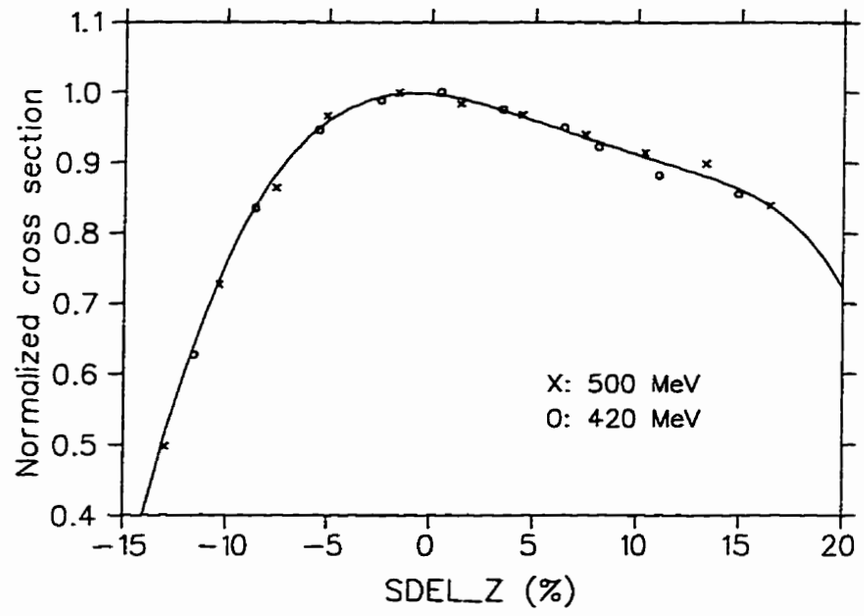

Figure 2.31: Normalized cross sections for the reaction $pp \rightarrow d\pi^+$, measured across the focal plane at both E633 beam energies. The fitted curve is the SASP acceptance function.

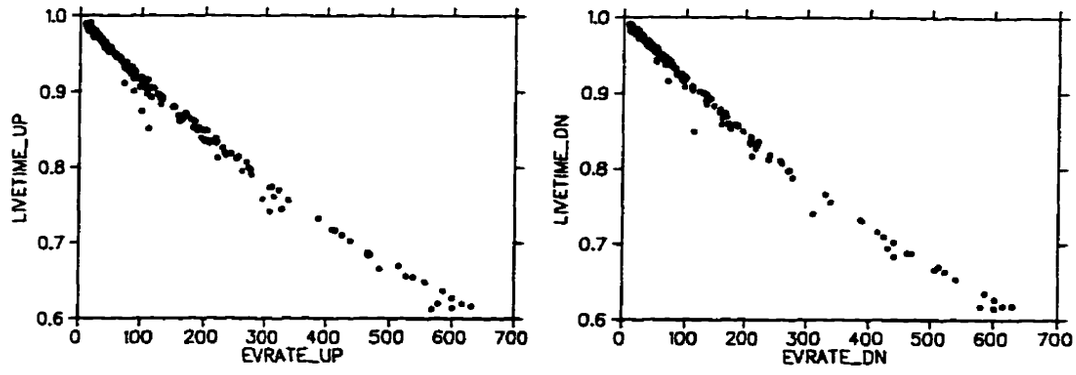

Figure 2.32: Computer livetime versus event rate for spin states UP and DOWN.

dependence due to unexplained rises in ungated event counts, as shown in figure 2.33. Consequently only spin-gated scalers were used in calculations.

2.3.12 Detector efficiency

The efficiency of the SASP detector system must be determined in order to normalize the calculated cross sections of the reactions.

The scintillators are considered effectively 100% efficient, provided their gains have been set properly (section 2.3.8 contains a note on a possible gain problem in one of the paddles). Therefore the detector efficiency is that of the FEC (when employed) and the VDC's.

E633 analysis followed two parallel courses—one using the FEC, and one not—and this was reflected in the offline NOVA OPSEQ (listed in appendix B), which evaluated two sets of detector conditions. In both cases, efficiency was evaluated for events which were identified as pions, as discussed in section 2.3.8. The following conditions were evaluated separately for ALL, spin UP and spin DOWN events.

The FECless efficiency was defined to be the fraction of those events identified as pions (as discussed in section 2.3.8) which passed the 'multiwire OK' condition of the VDC's:

```
LVDC_OK=LX1_OK&LX2_OK&LU1_OK&LU2_OK.
```

A plane is 'OK' if it registered a valid hit with position information. Note that

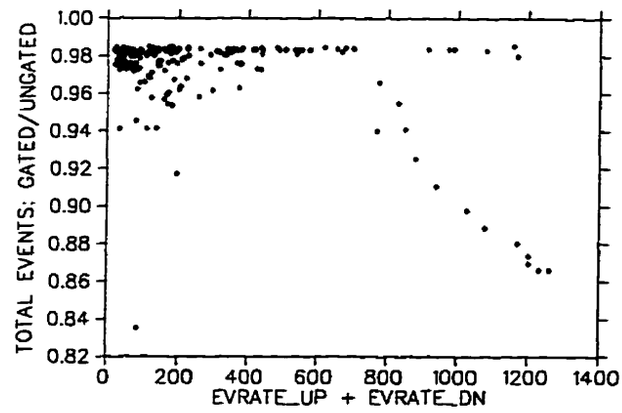

Figure 2.33: Ratio of spin-gated to ungated Event totals, plotted against the spin-gated event rate. If the beam current remained stable during spin-flipping, this ratio should be constant.

LVDC_OK was also used as a cut on the data—only events with position data at all four VDC wire planes were considered in further analysis.

For the NOVA analysis branch which used the FEC, the efficiency was determined from the pass fraction of the 'multiwire OK' of the FEC and VDC's

```
LMWOK=LVDC_OK&LFEC_OK
      LVDC_OK=LX1_OK&LX2_OK&LU1_OK&LU2_OK
      LFEC_OK=LXO_OK&LYO_OK.
```

This condition was evaluated after the particle identification and the requirement LFEC_OR, where

```
LFEC_OR=LXO_OK|LYO_OK.
```

By considering only events which which were also detected by the Front End Chamber. much room background (particles which did not pass through the spectrometer) was removed, resulting in more accurate efficiency estimates. Note that satisfying the condition LFEC_OK was a requirement for an event to be considered in the FEC-included data analysis.

The VDC efficiency results were checked by further calculations of the efficiency where all possible combinations of 2, 3 and 4 VDC planes were considered. These showed

expected variations due to the correlations in the hit patterns for adjacent planes, but the results were generally consistent with the composite VDC efficiency defined above.

Wire chamber efficiency is shown in figure 2.34, plotted against the rates of VDC plane X1 and scintillator S1. Dependence of the efficiencies upon rates is evident but not very strong. This is because the rates at the top end are largely determined by room background, while rates at the FEC are determined by the reaction rate at the target. These two are not necessarily highly correlated.

Error in detector efficiency is defined [21]

$$\varepsilon_\eta = \sqrt{\frac{\eta(1-\eta)}{N_{eval}}}, \tag{2.49}$$

where η is the efficiency, and N_{eval} is the number of times the efficiency condition was evaluated.

2.3.13 VDC and FEC meantime

VDC meantime is the TDC value for a hypothetical wire at the intersection of the particle track and a VDC wire plane. The NOVA variable LVDCMEANTIME is an average of these values, and is plotted in HSVDCMT. FEC meantime is an actual hardware mean for the timing pulses from the FEC wires. NOVA variable LFECMEANTIME is an average of the FEC wires, and is plotted in HSFECMT. The TDC's for both devices work in 'common stop' mode, where the start is a wire hit and the stop is a focal plane paddle hit time plus a delay. Thus, VDC and FEC meantimes give an approximate, relative measure of the time of flight from the respective wire chamber to the paddles. In E633, both HSVDCMT and HSFECMT always showed clear and clean peaks for the good events, and cuts on the meantimes—LVDCMTWIND and LFECMTWIND—were placed around them.

Since the VDC's are so close to the paddles, LVDCMEANTIME varies very little over the momentum range of the experiment, and LVDCMTWIND remained constant. LVDCMEANTIME was very clean, with the LVDCMTWIND pass rate over 98%.

The FEC meantime is a rough measure of time of flight through the spectrometer, and therefore shifts substantially for different momentum settings. LFECMEANTIME was also very clean, with LFECMTWIND pass rates typically over 95%. The primary

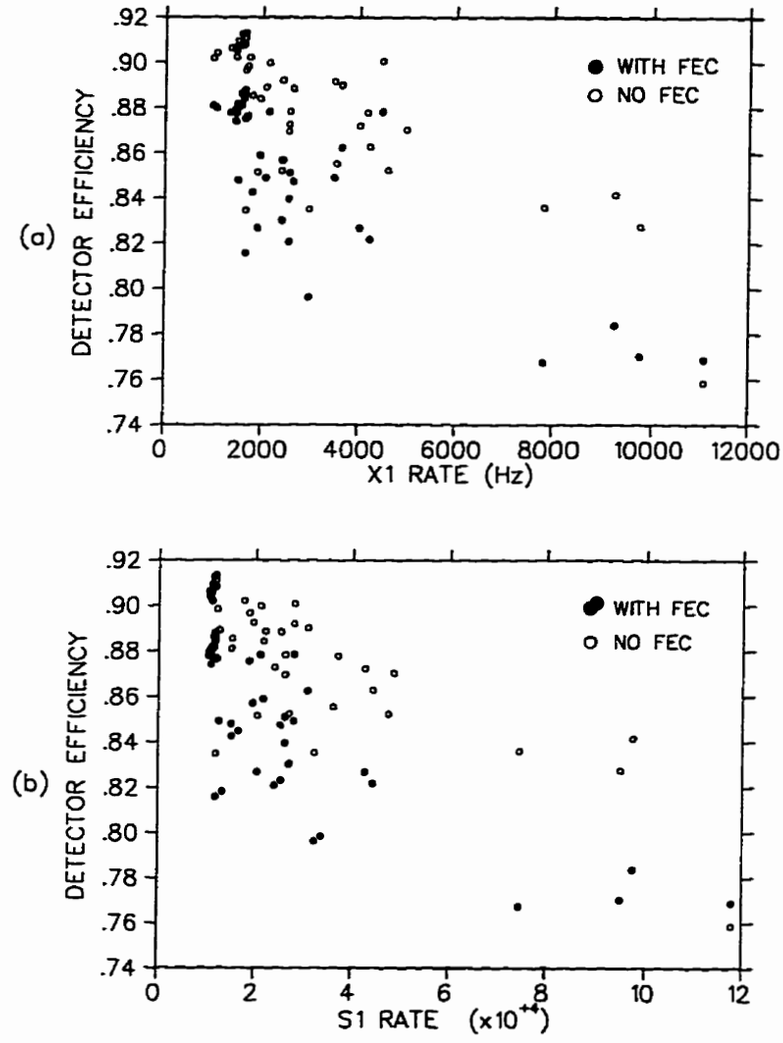

Figure 2.34: Combined detector efficiency, with and without the FEC. Efficiency declines at increased rates, as measured by the X1 plane (a) and scintillator S1 (b).

value of LFECMTWIND was in its removal of accidental events from earlier and later beam pulses. These are random coincidences with background triggers (recall that the trigger involved only top end detectors), and are separated from the good LFECMEAN-TIME peak by multiples of the beam pulse period, 43 ns.

2.4 Run plan

For scattering angles from 25° to 100°, the reaction $pp \rightarrow pn\pi^+$ was mapped out through a series of momentum bites. For each angle setting, the first bite was selected so the peak from the two body reaction $pp \rightarrow d\pi^+$ would appear at approximately δ=12%. Then contiguous momentum bites followed the three body continuum down to the lower measurable limit of pion momentum. Each data-taking run was preceded or followed by a background measurement run under the same conditions, but with the dummy target cell in place. Table 2.6 summarizes the useful E633 data and background runs. Angle settings at which the FEC was inadvertently unplugged are denoted NF.

Before data-taking at 500 MeV, and after data-taking at 420 MeV, momentum scans were made by sweeping the $pp \rightarrow d\pi^+$ peak across the focal plane in 3% steps. The 500 MeV scan had θ_{SASP} = 23.63°and θ_{TARGET}= -19°; the 420 MeV scan had θ_{SASP} = 54.95°and θ_{TARGET}= 23°.

There were some runs with the beam polarization off to measure instrumental asymmetry in the IBP. These runs are listed in table 2.7.

Target angle

It is illustrated in figure 2.10 on page 18 that kinetic energy losses in the target may be considerably different for pions produced at the beginning and at the end of the active area, because of the differing lengths of liquid hydrogen 'seen' by both the beam proton and the scattered pion. For each scattering angle, a target angle was calculated to minimize this difference for the pions from $pp \rightarrow d\pi^+$, and thereby increase momentum resolution for this peak. The program for this included the curved shape of the cell and the contribution of the stainless steel walls. Note that target angle, like SASP angle, was measured in the opposite direction of the Transport convention for angles in the

E633 DATA RUN SUMMARY			
SASP Angle (°)	Target Angle (°)	Data Run Numbers	Bkgd. Run Numbers
- 500 MeV -			
23.63	-19	95,97,100,101,104	96,98,99,102,103
34.97	-3	110,113,115,117,119	112,114,116,118,120
44.98	8	123,125,127,129,131	124,126,128,130,132
54.98	19	134,137,140,141 (NF)	135,138,139,142 (NF)
65.08	28	147,150,152	148,149,153
75.18	36	162,165,166,170	163,164,167,171
85.07	44	173,176,178,182	174,175,179,180
99.99	50	183,188,189 (NF)	185,186,190 (NF)
- 420 MeV -			
25.06	-17	259,262,263,265,268	260,261,264,266,267
34.96	-2	246,249,252,253,256	248,250,251,255,257
44.98	12	235,237,240,242	236,239,241,243
55.05	23	224,226,228	225,227,230
65.05	33	216,219,222	217,218,221
75.10	42	208,211,213	209,210,214
85.07	50	202,205	203,204
99.99	60	195,197 (NF)	196,199 (NF)

Table 2.6: A summary of the E633 data and background runs.

——Polarization Off Runs——		
Beam Energy (MeV)	IBP Target	Run Numbers
500	3	133,145,159,172,184,191
500	4	74-85,161
420	3	194,200,206,207,215,233,234
420	4	246,274

Table 2.7: A list of runs with unpolarized beam.

non-bend plane.

Chapter 3

Analysis and Results

3.1 Analysis

Cross sections, analyzing powers, and statistical errors were calculated from the NOVA pion momentum spectra in the program E633_ANAL.FOR (appendix C), or in a non-binning version E633_ANAL_P.FOR which worked on a channel by channel basis, allowing resolution in momentum to 0.04%. Relatively simple programs then subtracted out the $pp \rightarrow d\pi^+$ cross sections and the muon contribution.

3.1.1 Cross section

The spin-averaged differential cross section was calculated

$$\frac{d^2\sigma}{d\Omega dp} = \frac{P(\downarrow)\frac{d^2\sigma}{d\Omega dp}(\uparrow) + P(\uparrow)\frac{d^2\sigma}{d\Omega dp}(\downarrow)}{P(\uparrow) + P(\downarrow)} \tag{3.1}$$

where '$\uparrow$' and '$\downarrow$' refer to spin up and down states, and dp refers to the momentum interval of the detected pion. Cross sections were calculated for the Up and Down beam spin states. A cross section for all events was also calculated, but not used due to uncertainty about the spin Off fraction. Cross sections were calculated in two versions: one which used FEC data, and one which did not. The spin-dependent cross section was defined

$$\frac{d^2\sigma}{d\Omega dp}(\updownarrow) = \frac{Counts(\updownarrow)}{n_p(\updownarrow)n_t n_{live}(\updownarrow)E_{det}(\updownarrow)d\Omega dp} \tag{3.2}$$

where ($\updownarrow$) indicates a spin-dependent quantity. *Counts* are the total Up or Down events, weighted for spectrometer acceptance and pion survival on an event-by-event basis, as

discussed in section 2.3.10. n_p is the number of beam protons which hit the target. which is determined by multiplying the beam flux measured by the SEM by the spin state fraction determined by the IBP; for spin Up, for example, this is

$$n_p = \frac{SEMI \cdot POLU}{POLU + POLD} / 1.602 \times 10^{-10}, \tag{3.3}$$

where SEMI is the corrected total charge, in nC, measured by the SEM (section 2.1.2), and POLU and POLD are the spin-gated total IBP counts (section 2.1.3)

$$POLU = L(UP) + R(UP) - L_{acc}(UP) - R_{acc}(UP) \tag{3.4}$$

$$POLD = L(DN) + R(DN) - L_{acc}(DN) - R_{acc}(DN). \tag{3.5}$$

n_{live} is the computer live time, defined in section 2.3.11. E_{det} is the combined detector efficiency, defined in section 2.3.12. $d\Omega$ is the SASP solid angle, 13.5 msr. dp is the pion momentum interval for the calculation. The smallest interval used in our calculations was 0.04% of the central momentum. n_t is the number of target protons per cm^2,

$$n_t = \frac{t\rho}{cos\theta_T} \tag{3.6}$$

where t is the perpendicular thickness at the centre of the target cell, ρ is the density in nuclei/cm^3, and θ_T is the target angle. For the target thickness of 9.82 mm and liquid hydrogen at 16.25 psi, $t\rho = 4.111 \times 10^{22}$ protons/cm^2.

Background subtraction

For the background runs with the dummy target, spin averaged differential cross sections were similarly calculated with equation 3.1 and equation 3.2. In calculating the background cross sections, the same target density, n_t, was used. Thus, the background cross sections were calculated as if the background events also came from $pp \rightarrow pn\pi^+$. so they could be directly subtracted from those calculated from the data runs, for each spin-dependent cross section:

$$\frac{d^2\sigma}{d\Omega dp}(\updownarrow) = \frac{d^2\sigma}{d\Omega dp}(\updownarrow)(LH_2) - \frac{d^2\sigma}{d\Omega dp}(\updownarrow)(Dummy). \tag{3.7}$$

Background momentum measurements were corrected with the target energy loss function of a full target, as discussed in section 2.2.1. This is not precisely correct, but the error thus created is insignificant.

3.1.2 Subtraction of synchronous muons

As discussed in section 2.3.8, detected particles were identified during NOVA analysis on the basis of time of flight and $\frac{dE}{dx}$ in the scintillator paddles. Pions and muons were not always distinguishable on this basis. For example, for a beam energy of 500 MeV and a reaction angle of 23.6°, the reaction $pp \rightarrow d\pi^+$ produces pions of momentum 295 MeV/c. This reaction was measured in run 95 (see Run Plan in section 2.4). Muons of the same momentum differ in time of flight through the spectrometer by only 1.2 ns. But the detected pion group for this run extended over an LRFTIME range of over 6 ns; the muon and pion groups have effectively the same timing. This situation arose at the highest momentum runs at most reaction angles, and usually there was also overlap to varying degrees in the second and third momentum bites.

Muons were a problem because of the relatively intense flux of pions from the $pp \rightarrow d\pi^+$ reaction. These pions, decaying between the target and the entrance to the spectrometer, produced a muon flux which is considerable compared to the low cross section pion flux at the lower momentum bites. The solution was to estimate the muon population for the conditions of each run. This was done with the Monte Carlo program MUON_MC.FOR (appendix D). Comparison of MUON_MC output with measured muon levels, where this was possible, showed reasonable accuracy. Figure 3.1 shows measured muon cross sections with the results of the Monte Carlo, for the lower momentum settings (where the pions and muons were distinguishable on the basis of time of flight) at several angles. In some cases, such as the settings represented by figures 3.1(b) and 3.1(c), *ad hoc* scaling factors were applied to correct the muon background estimates. Error was taken to be 30%. The program calculated differential cross sections so its output (or an estimated fraction thereof, in cases of partial overlap) could be subtracted from the measured cross sections, much like background.

Since muons show the same analyzing power as the pions they decayed from, and most of the muons came from the intense pion peak from $pp \rightarrow d\pi^+$, measured analyzing power also had to be recalculated where there was muon contamination:

$$A_c = \frac{\sigma_m A_m - \sigma_\mu A_\mu}{\sigma_m - \sigma_\mu} \tag{3.8}$$

where σ_m is the measured cross section, A_m is the measured analyzing power, σ_μ is the

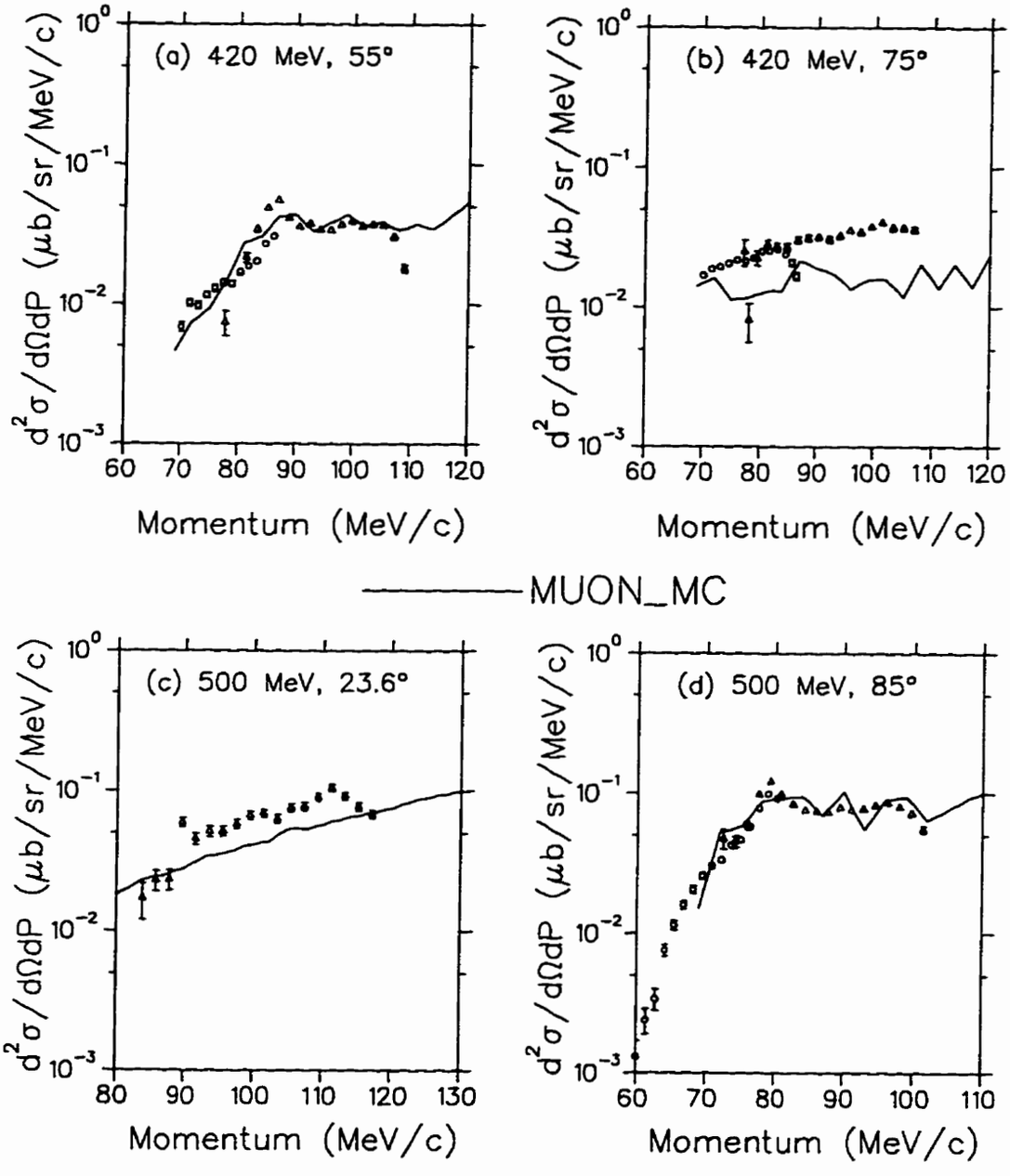

Figure 3.1: Measured muon cross sections are shown for the lower momentum bites at several angles and energies, along with Monte Carlo predictions. Agreement is good in (a) and (d); corrections were made based on (b) and (c).

estimated cross section contribution of the muons, and A_μ is the muon analyzing power.

Figure 3.2 shows the estimated muon cross sections and the measured 'pion' cross sections, and the measured and corrected analyzing powers, for one reaction angle. The muon rise around 160 MeV/c comes from the decay of pions from $pp \rightarrow d\pi^+$, where the muon is emitted at an angle of 180° in the pion rest frame. Note how this bump is reflected in the rise of A_{N0} at the same pion momentum. The influence of contaminant muons was magnified by the pion survival factor (introduced in section 2.3.10), since the muons themselves, having a lifetime of 2.2 μs, do not decay in significant numbers within the spectrometer. Consequently the estimated muon cross section must be increased by the pion survival factor before being subtracted from the measured cross section.

3.1.3 Subtraction of the deuteron peak

After the background and muon contributions were subtracted from the measured cross sections, the next step was to subtract the part of the measured cross section corresponding to the $pp \rightarrow d\pi^+$ reaction. Since this was an inclusive measurement in which recoil particles were not detected, pions from $pp \rightarrow d\pi^+$ and from $pp \rightarrow pn\pi^+$ are distinguishable only on the basis of their momenta. As shown in figure 3.3(a), separation of the deuteron peak from the three body continuum was not complete; in addition to an approximately gaussian peak shape, there was a long high momentum tail. Preliminary Monte Carlo calculations for muons produced between the dipole and VDC2 showed that these might account for long tails in the peak distribution, but detailed calculations are not yet complete.

With the assumption of symmetry, the tail of the deuteron peak underlying the beginning of the continuum was found by reflecting the higher momentum half of the peak and the visible tail about the peak centroid. Then the upper half and its reflection were subtracted from the measured cross section. An example of the curves involved is shown in figure 3.3(b). This technique reduced the highest part of the cross section continuum by between 2 and 15%. Analyzing power in the continuum was not recalculated after the removal of the deuteron tail contribution.

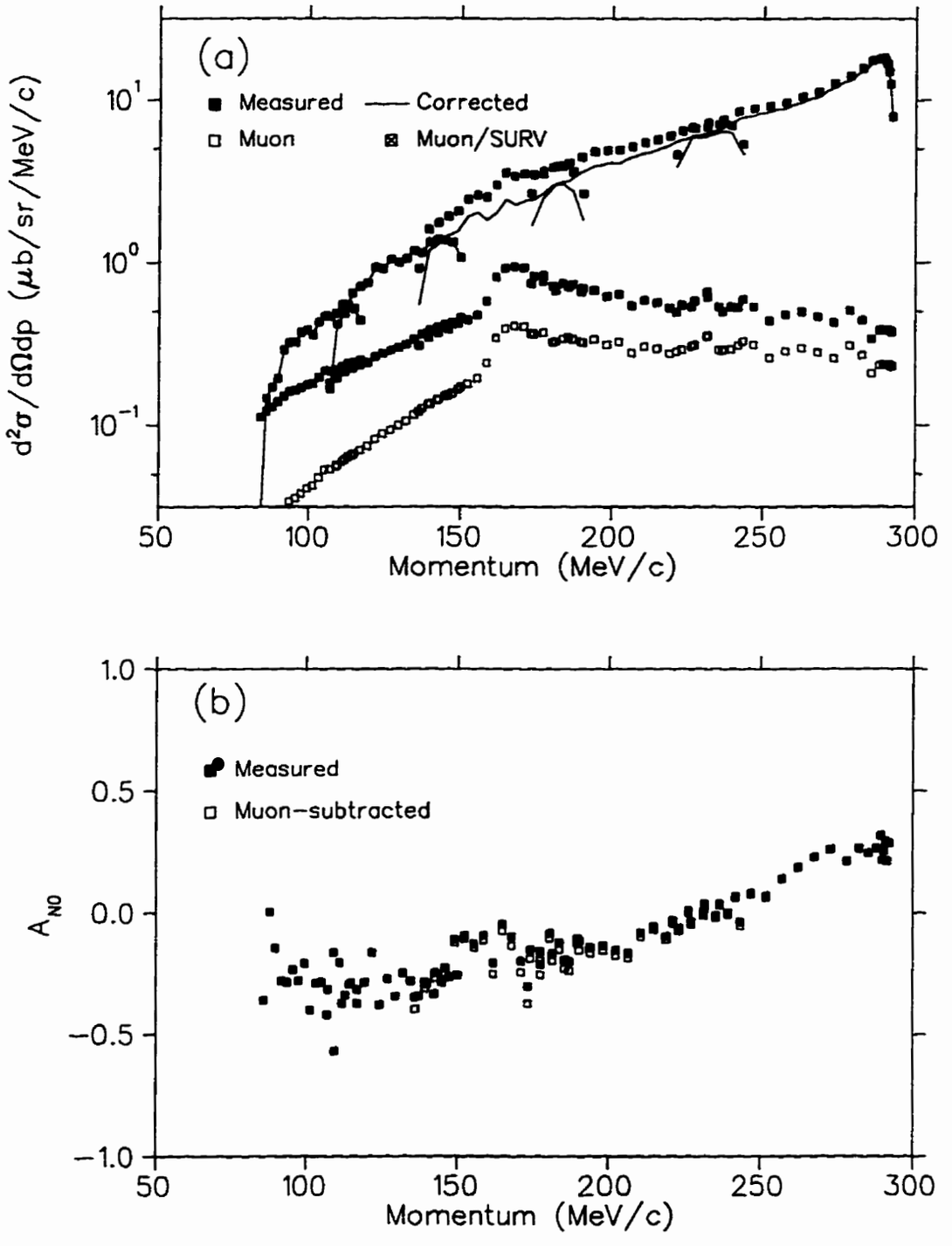

Figure 3.2: For beam energy 500 MeV, reaction angle 23.5°: (a) shows the estimated muon cross sections with and without the pion survival factor, and the measured cross sections before and after muon subtraction; (b) shows the analyzing powers before and after corrections for muon subtraction.

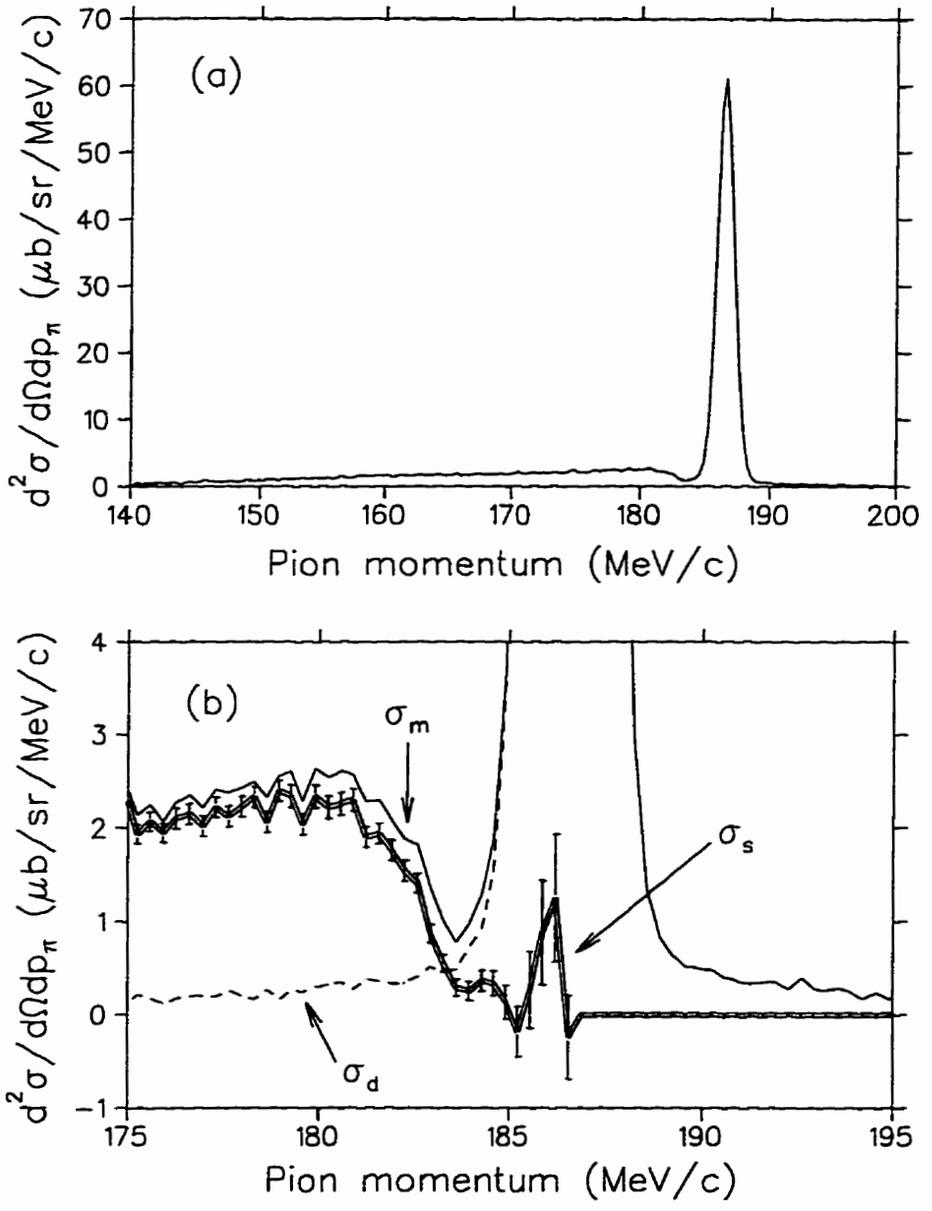

Figure 3.3: A cross section measurement including the deuteron peak and the beginning of the three body continuum (a). An expansion of the separation region (b) illustrates the peak subtraction technique; shown are the original cross section measurement σ_m, the reflected peak shape σ_d and the peak-subtracted cross section σ_s, with error.

3.1.4 Analyzing power

The analyzing power was calculated

$$A_{N0} = \frac{-(\frac{d^2\sigma}{d\Omega dp}(\uparrow) - \frac{d^2\sigma}{d\Omega dp}(\downarrow))}{P(\downarrow)\frac{d^2\sigma}{d\Omega dp}(\uparrow) + P(\uparrow)\frac{d^2\sigma}{d\Omega dp}(\downarrow)} \tag{3.9}$$

using the background-subtracted differential cross sections and the magnitudes of the Up and Down polarizations. The minus sign in the numerator appears because the SASP was to the right of the beam, whereas the convention assumes the reaction angle is to the left.

3.1.5 Statistical error

Spin-dependent cross section

Statistical error in the spin-dependent cross section, as defined in equation 3.2, arises from the statistical error of its constituents. Denoting this cross section $\sigma(\updownarrow)$, the error is calculated

$$\frac{\varepsilon^2_{\sigma(\updownarrow)}}{\sigma(\updownarrow)^2} = \frac{\varepsilon^2_{Counts(raw)}}{(Counts(raw))^2} + \frac{\varepsilon^2_{n_p}}{n_p^2} + \frac{\varepsilon^2_{n_{live}}}{n^2_{live}} + \frac{\varepsilon^2_{E_{det}}}{E^2_{det}}. \tag{3.10}$$

$Counts(raw)$ are the measured event counts, not normalized for pion survival and SASP acceptance; these were plotted in HSDELF_UP, HSDELF_DN, HSDELNF_UP and HSDELNF_DN. The error in this quantity is

$$\varepsilon_{Counts(raw)} = \sqrt{Counts(raw)}. \tag{3.11}$$

The number of protons hitting the target is given, for the spin Up state, by equation 3.3. The statistical error in n_p is

$$\varepsilon_{n_p} = \frac{1}{C_p}\sqrt{\varepsilon^2_{SEMI}\left(\frac{\partial n_p}{\partial SEMI}\right)^2 + \varepsilon^2_{POLU}\left(\frac{\partial n_p}{\partial POLU}\right)^2 + \varepsilon^2_{POLD}\left(\frac{\partial n_p}{\partial POLD}\right)^2}, \tag{3.12}$$

where $C_p = 1.602 \times 10^{-10}$. The error in the total SEM accumulated current, ε_{SEMI} is given by equation 2.3 in section 2.1.2. The error in spin-gated polarimeter counts is just the counting errors of the IBP detectors; thus, from equation 3.4,

$$\varepsilon_{POLU} = \sqrt{L(UP) + R(UP) + L_{acc}(UP) + R_{acc}(UP)} \tag{3.13}$$

and similarly for ε_{POLD}. The partial differentials of equation 3.3 are

$$\frac{\partial n_p}{\partial SEMI} = \frac{POLU}{POLU + POLD} \tag{3.14}$$

$$\frac{\partial n_p}{\partial POLU} = \frac{POLD}{(POLU + POLD)^2} \tag{3.15}$$

$$\frac{\partial n_p}{\partial POLD} = \frac{-POLU}{(POLU + POLD)^2}. \tag{3.16}$$

Substituting these into equation 3.12 gives, after some rearrangement,

$$\varepsilon_{n_p} = \frac{\sqrt{(\varepsilon^2_{POLU} POLD^2 + \varepsilon^2_{POLD} POLU^2)(\frac{SEMI}{POLU+POLD})^2 + \varepsilon^2_{SEMI} POLU^2}}{POLU + POLD}. \tag{3.17}$$

Statistical livetime error, $\varepsilon_{n_{live}}$, is defined in equation 2.48 in section 2.3.11. Detector efficiency error, $\varepsilon_{E_{det}}$ is defined in equation 2.49 in section 2.3.12.

The error in spin Down cross section was calculated similarly.

The error in cross section for the dummy target was also calculated using equation 3.10. The error in the background-subtracted result is

$$\varepsilon_{\sigma(\updownarrow)} = \sqrt{\varepsilon^2_\sigma(\updownarrow)(LH_2) + \varepsilon^2_\sigma(\updownarrow)(Dummy)}, \tag{3.18}$$

where σ again represents the differential cross section.

Spin-averaged cross section

Statistical error in the spin-averaged cross section arises from the error in the polarizations and spin-dependent cross sections:

$$\varepsilon^2_\sigma = \varepsilon^2_{P(\updownarrow)} \left(\frac{\partial \sigma}{\partial P(\updownarrow)}\right)^2 + \varepsilon^2_{P(\downarrow)} \left(\frac{\partial \sigma}{\partial \sigma(\updownarrow)}\right)^2 + \varepsilon^2_{\sigma(\updownarrow)} \left(\frac{\partial \sigma}{\partial \sigma(\updownarrow)}\right)^2 + \varepsilon^2_{\sigma(\downarrow)} \left(\frac{\partial \sigma}{\partial \sigma(\downarrow)}\right)^2, \tag{3.19}$$

where $\sigma(\uparrow)$, $\sigma(\downarrow)$ and σ represent the spin Up, spin Down and spin-averaged differential cross sections. With the partial differentials determined from equation 3.1, the error becomes

$$\begin{aligned} \varepsilon^2_\sigma &= \varepsilon^2_{P(\updownarrow)} \left(-\frac{P(\downarrow)(\sigma(\uparrow) - \sigma(\downarrow))}{(P(\uparrow) + P(\downarrow))^2}\right)^2 + \varepsilon^2_{P(\downarrow)} \left(\frac{P(\uparrow)(\sigma(\uparrow) - \sigma(\downarrow))}{(P(\uparrow) + P(\downarrow))^2}\right)^2 \\ &+ \varepsilon^2_{\sigma(\updownarrow)} \left(\frac{P(\downarrow)}{(P(\uparrow) + P(\downarrow))}\right)^2 + \varepsilon^2_{\sigma(\downarrow)} \left(\frac{P(\uparrow)}{(P(\uparrow) + P(\downarrow))}\right)^2. \end{aligned} \tag{3.20}$$

and therefore

$$\varepsilon_\sigma = \frac{\sqrt{\varepsilon^2_{P(\updownarrow)} \left(\frac{P(\downarrow)(\sigma(\uparrow)-\sigma(\downarrow))}{(P(\uparrow)+P(\downarrow))}\right)^2 + \varepsilon^2_{P(\downarrow)} \left(\frac{P(\uparrow)(\sigma(\uparrow)-\sigma(\downarrow))}{(P(\uparrow)+P(\downarrow))}\right)^2 + \varepsilon^2_{\sigma(\updownarrow)} P(\downarrow)^2 + \varepsilon^2_{\sigma(\downarrow)} P(\uparrow)^2}}{P(\uparrow) + P(\downarrow)}. \tag{3.21}$$

The error arising from the subtraction of the muon contribution, σ_μ, from the measured cross section σ_m is

$$\varepsilon_{\sigma_c} = \sqrt{\varepsilon^2_{\sigma_m} + \varepsilon^2_{\sigma_\mu}}. \tag{3.22}$$

The error in the estimated muon cross section contribution was taken to be 30%.

Similarly the error arising from the subtraction of the deuteron peak cross section σ_d is

$$\varepsilon_\sigma = \sqrt{\varepsilon^2_{\sigma_c} + \varepsilon^2_{\sigma_d}}. \tag{3.23}$$

The error in the peak cross section is just the normal statistical error calculated in equations 3.21 and 3.22, calculated over the higher momentum half of the peak.

Analyzing power

Statistical error in the analyzing power arises from error in the beam polarization and the spin-dependent cross sections. Formally, the error is

$$\varepsilon^2_{A_{N0}} = \varepsilon^2_{P(\uparrow)}\left(\frac{\partial A_{N0}}{\partial P(\uparrow)}\right)^2 + \varepsilon^2_{P(\downarrow)}\left(\frac{\partial A_{N0}}{\partial P(\uparrow)}\right)^2 + \varepsilon^2_{\sigma(\uparrow)}\left(\frac{\partial A_{N0}}{\partial \sigma(\uparrow)}\right)^2 + \varepsilon^2_{\sigma(\downarrow)}\left(\frac{\partial A_{N0}}{\partial \sigma(\downarrow)}\right)^2, \tag{3.24}$$

where $\sigma(\uparrow)$ and $\sigma(\downarrow)$ represent the spin Up and spin Down differential cross sections. The cross section errors were calculated with equation 3.10, and the polarization errors with equation 2.8 in section 2.1.3. Calculating the partial differentials from equation 3.9, equation 3.24 becomes

$$\begin{aligned}\varepsilon^2_{A_{N0}} &= \varepsilon^2_{P(\uparrow)}\left(\frac{(\sigma(\uparrow)-\sigma(\downarrow))\sigma(\downarrow)}{(P(\downarrow)\sigma(\uparrow)+P(\uparrow)\sigma(\downarrow))^2}\right)^2 + \varepsilon^2_{P(\downarrow)}\left(\frac{(\sigma(\uparrow)-\sigma(\downarrow))\sigma(\uparrow)}{(P(\downarrow)\sigma(\uparrow)+P(\uparrow)\sigma(\downarrow))^2}\right)^2 \\ &+ \varepsilon^2_{\sigma(\uparrow)}\left(\frac{-\sigma(\downarrow)(P(\uparrow)+P(\downarrow))}{(P(\downarrow)\sigma(\uparrow)+P(\uparrow)\sigma(\downarrow))^2}\right)^2 + \varepsilon^2_{\sigma(\downarrow)}\left(\frac{\sigma(\uparrow)(P(\uparrow)+P(\downarrow))}{(P(\downarrow)\sigma(\uparrow)+P(\uparrow)\sigma(\downarrow))^2}\right)^2\end{aligned} \tag{3.25}$$

and therefore

$$\varepsilon_{A_{N0}} = \frac{\sqrt{(\sigma(\uparrow)-\sigma(\downarrow))^2(\varepsilon^2_{P(\downarrow)}\sigma(\uparrow)^2 + \varepsilon^2_{P(\uparrow)}\sigma(\downarrow)^2) + (P(\uparrow)+P(\downarrow))^2(\varepsilon^2_{\sigma(\downarrow)}\sigma(\downarrow)^2 + \varepsilon^2_{\sigma(\downarrow)}\sigma(\uparrow)^2}}{(P(\downarrow)\sigma(\uparrow)+P(\uparrow)\sigma(\downarrow))^2}. \tag{3.26}$$

Error in the muon-corrected analyzing power A_c is

$$\varepsilon_{A_c} = \sqrt{2\left(\frac{U^2+V^2}{W^2}\right)(\varepsilon^2_{\sigma_m} + \varepsilon^2_{\sigma_\mu})}, \tag{3.27}$$

where

$$\begin{aligned} U &= \sigma_m(1-A_m)-\sigma_\mu(1-A_\mu) \\ V &= \sigma_m(1+A_m)-\sigma_\mu(1+A_\mu) \\ W &= 2(\sigma_m-\sigma_\mu)^2; \end{aligned}$$

the subscripts m and μ refer to the measured and muon quantities, respectively. This formula used the simplifying assumption that

$$\varepsilon_{\sigma(\uparrow)} \simeq \varepsilon_{\sigma(\downarrow)}. \tag{3.28}$$

3.1.6 Systematic error

A number of the quantities which go into calculating the spin-dependent differential cross section (equation 3.2) have associated systematic errors. If combined in quadrature, these errors result in a 6% systematic uncertainty estimate.

Normalized counts

The normalization of momentum spectra counts for SASP acceptance and the pion survival fraction (introduced in section 2.3.10) contributes a systematic error to the resultant counts estimated at $\pm 3\%$.

Solid angle

The SASP solid angle, $d\Omega$, depends in a complex way upon cuts on the reconstructed particle trajectories. Very generous cuts were used the current experiment and this, together with the experience of earlier studies, led to an estimation of $d\Omega = 13.5 \pm 4\%$.

Target density

If we allow a target thickness uncertainty of ± 0.2 mm this contributes a systematic error of $\pm 2\%$ in the target nuclear density n_t. A further error of $\pm 1\%$ is contributed by uncertainty in the target angle. The contribution of the thin sleeve of superinsulation to the effective hydrogen thickness was negligible.

Beam flux

From the experimental calibration data of the SEM and IBP, the estimated error in proton flux measurements are ±2% for each device. For the IBP this does not include the uncertainty in the target thickness, but the discrepancy between beam energies, discussed in section 2.1.4, is independent of this. Two possible explanations are advanced: (i) The IBP count rates are relatively low at 500 MeV due to overly high discriminator levels. It would be necessary for the settings to be similarly wrong for all IBP detectors arms, since no strong beam dependent instrumental asymmetry was observed; (ii) If the IBP gives the correct relative proton flux (which it should since the *pp* elastic cross section is well known), then the total charge measured by the SEM is approximately 6% low at 420 MeV, compared to 500 MeV, and the cross sections at 420 MeV will consequently be 6% high.

3.1.7 Measurements without the Front End Chamber

As indicated in the Run Plan in section 2.4, there were three sets of measurements in which the FEC was not working. These were the measurements at 55° and 100° at 500 MeV, and at 100° at 420 MeV. In order to have useful results from these measurements it was necessary to use a parallel course of analysis which made no use of FEC data. The FECless branch, which involved different wire chamber efficiencies, cuts, and coordinates as previously discussed, resulted in a second set of NOVA output spectra. For instance, for momentum in the spin Up state, there was both HSDELFUP and HSDELNFUP (the complete OPSEQ is listed in appendix B). These noFEC output spectra and efficiencies were used in a parallel set of cross section and analyzing power calculations. This set was compared with the presumably more accurate results where the FEC data was used, and this led to correction factors to be applied to the three noFEC data sets.

NoFEC cross sections were generally higher, as indicated in figure 3.4. This was mainly due to our inability in these cases to cut on x_i and the relative increase of background events permitted when there was no event confirmation at the front end (recall that only top end detectors were in the trigger).

The ratio of FEC/noFEC cross section decreased linearly in momentum from a max-

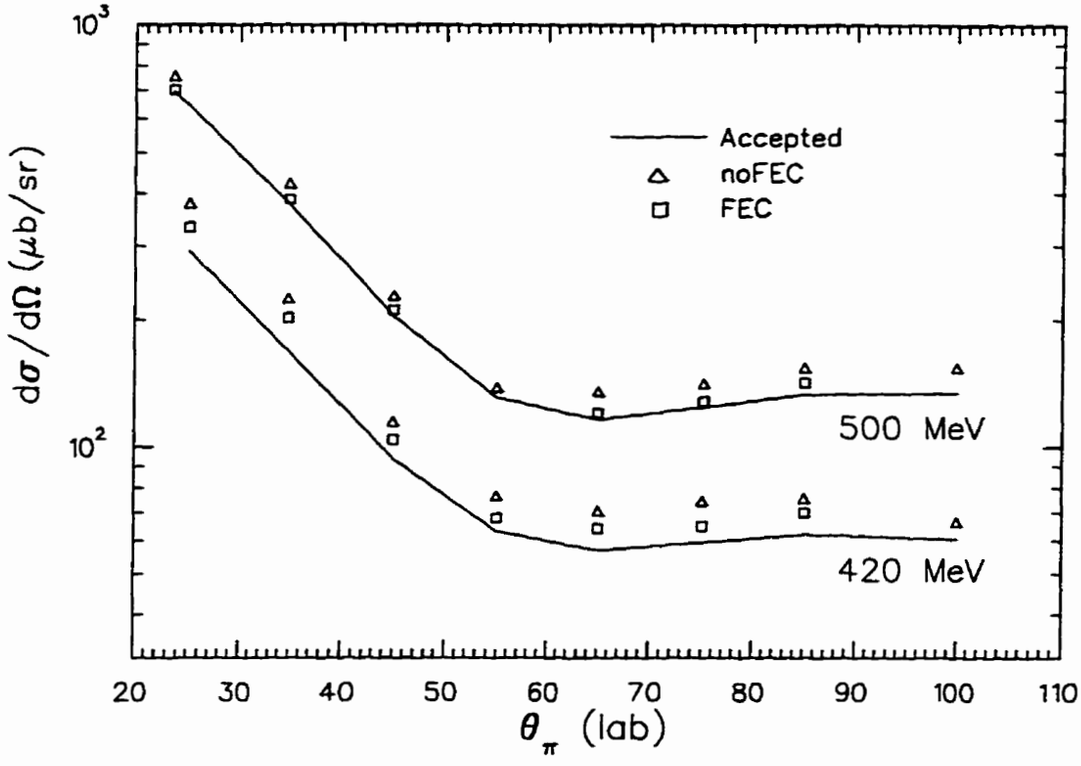

Figure 3.4: Measured cross sections for the reaction $pp \rightarrow d\pi^+$, calculated with and without FEC data, and the accepted values [25]. Statistical error bars are smaller than the plotting symbols.

imum at the deuteron peak, reflecting an increasing proportion of background events as the reaction cross section decreases. Momentum-dependent fits to these ratios provided corrective scaling factors for the three noFEC cross section curves. In cases where this was done, both the original and corrected cross section curves are shown (figures 3.8,3.12. and 3.20).

3.2 Results

3.2.1 $pp \rightarrow d\pi^+$

Figure 3.4 shows the measured cross sections for $pp \rightarrow d\pi^+$, calculated with and without FEC data, together with the values of Bugg *et al.* [25]

3.2.2 $pp \rightarrow pn\pi^+$

Figures 3.5 through 3.20 show the cross sections and analyzing powers for the reaction angles and beam energies of E633. Alternating symbols indicate the ranges of individual momentum bites. Note that for cross section results, error bars were often smaller than the plotting symbols. Measurements become inaccurate at the edges of each bite due to uncertainties in particle paths near edges of the focal plane; path length and acceptance become irregular. Also shown are the predictions of a simple model, which is discussed in the next section. The results in these figures were calculated with FEC data, except where otherwise indicated.

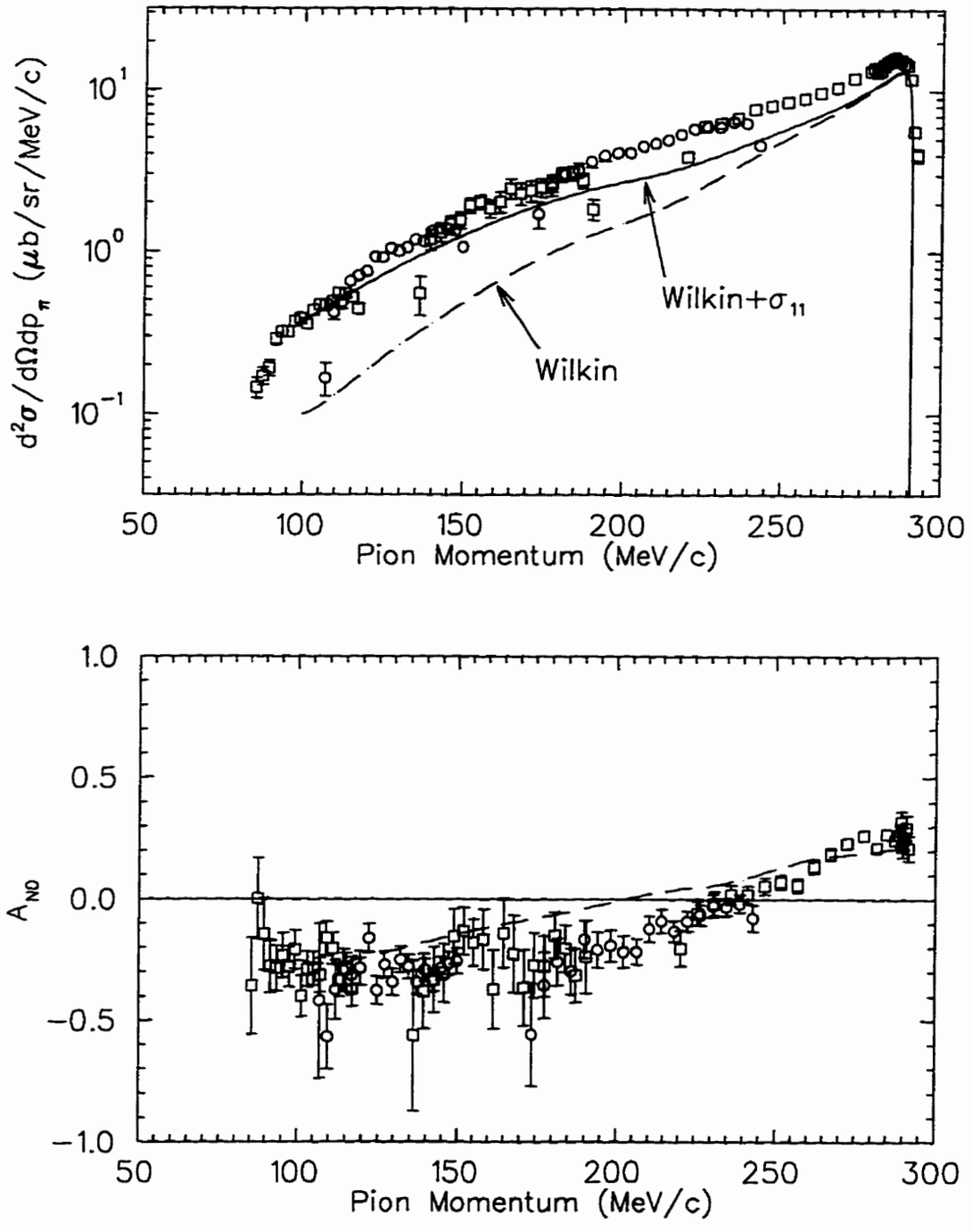

Figure 3.5: Cross sections and analyzing powers for $pp \rightarrow pn\pi^+$. 500 MeV, θ=23.6°, with the predictions of Falk/Wilkin. For the cross section, the Wilkin prediction is also shown with a σ_{11} term added.

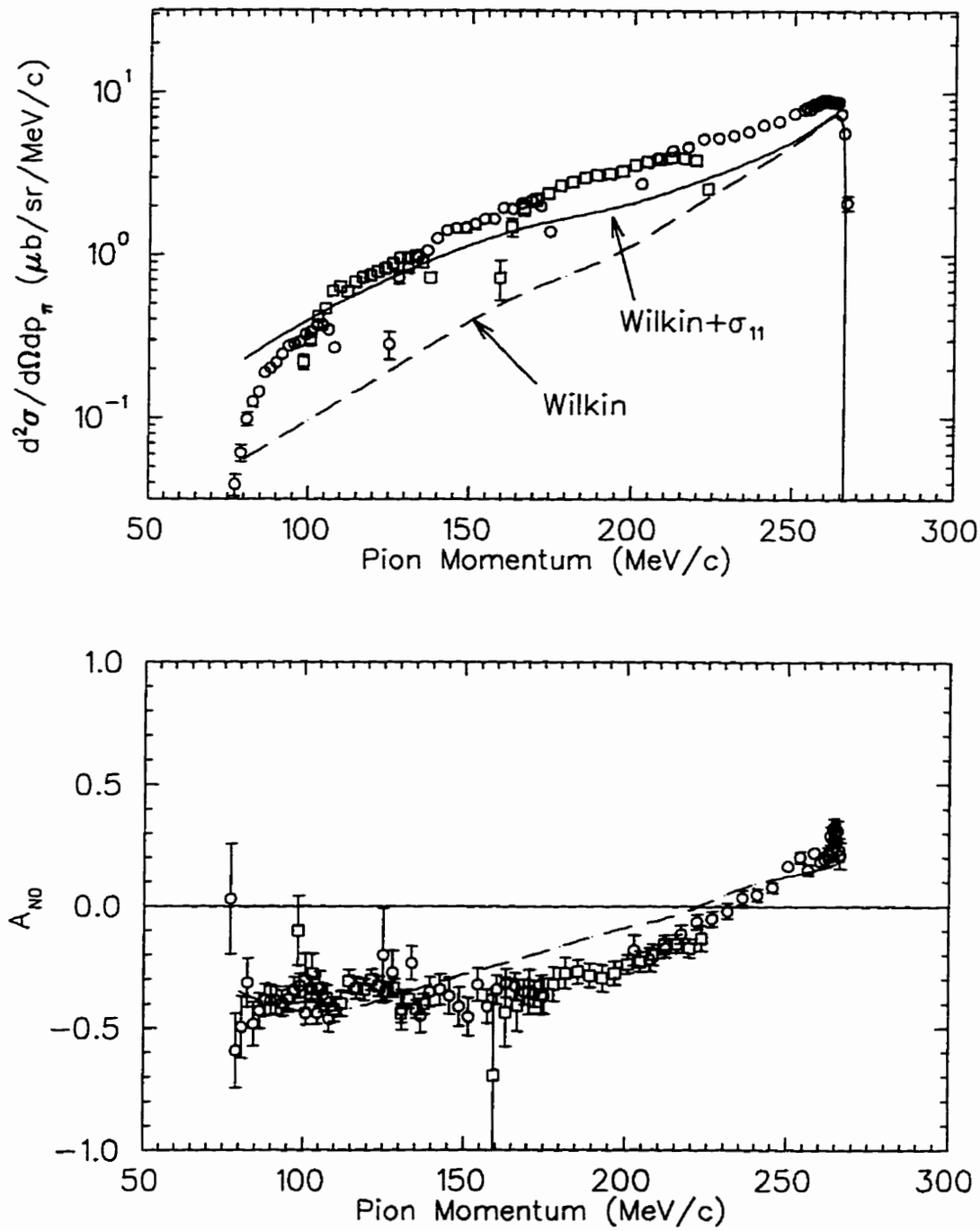

Figure 3.6: Cross sections and analyzing powers for $pp \rightarrow pn\pi^+$. 500 MeV, θ=35.0°, with the predictions of Falk/Wilkin. For the cross section, the Wilkin prediction is also shown with a σ_{11} term added.

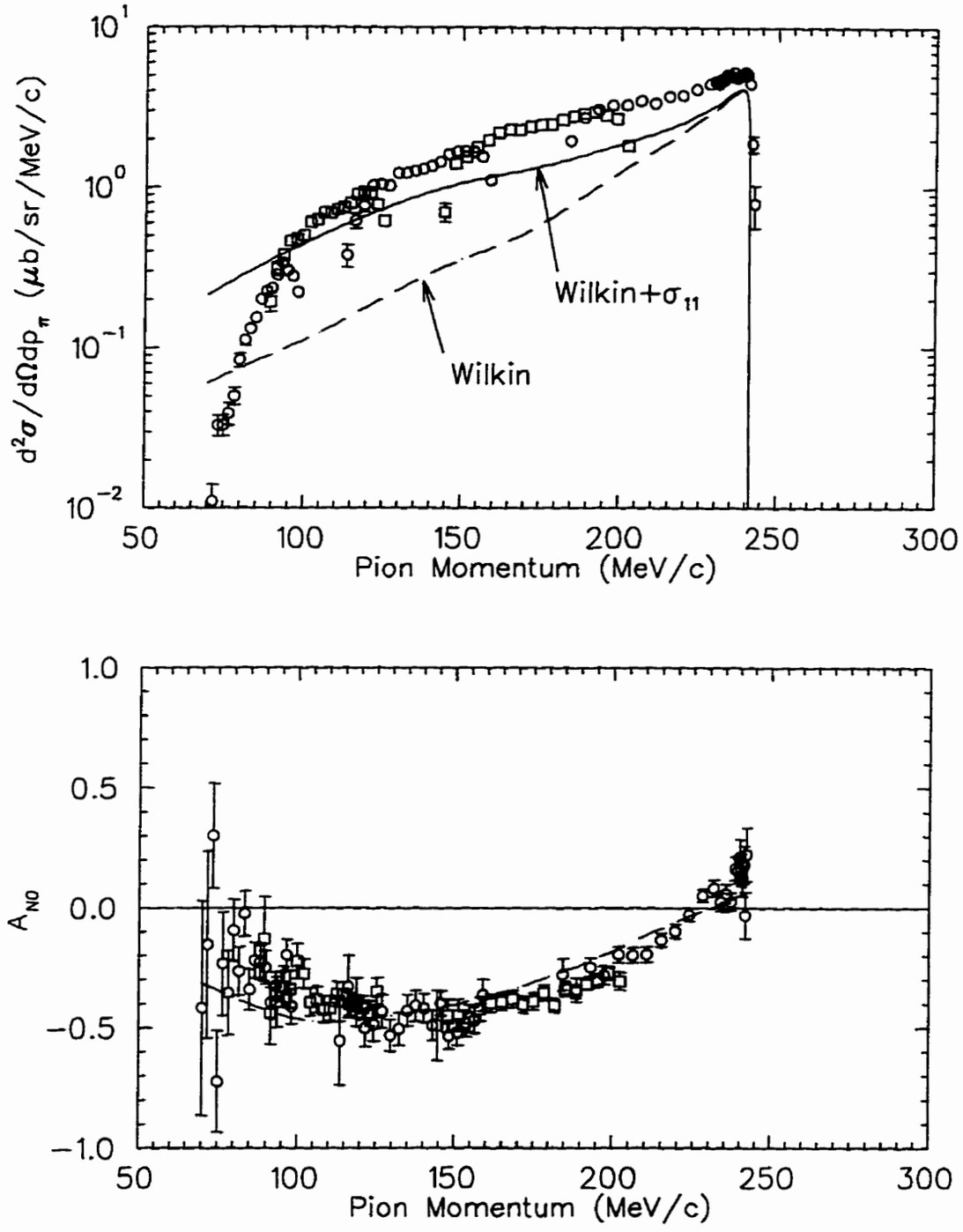

Figure 3.7: Cross sections and analyzing powers for $pp \rightarrow pn\pi^+$. 500 MeV, θ=45.0°, with the predictions of Falk/Wilkin. For the cross section, the Wilkin prediction is also shown with a σ_{11} term added.

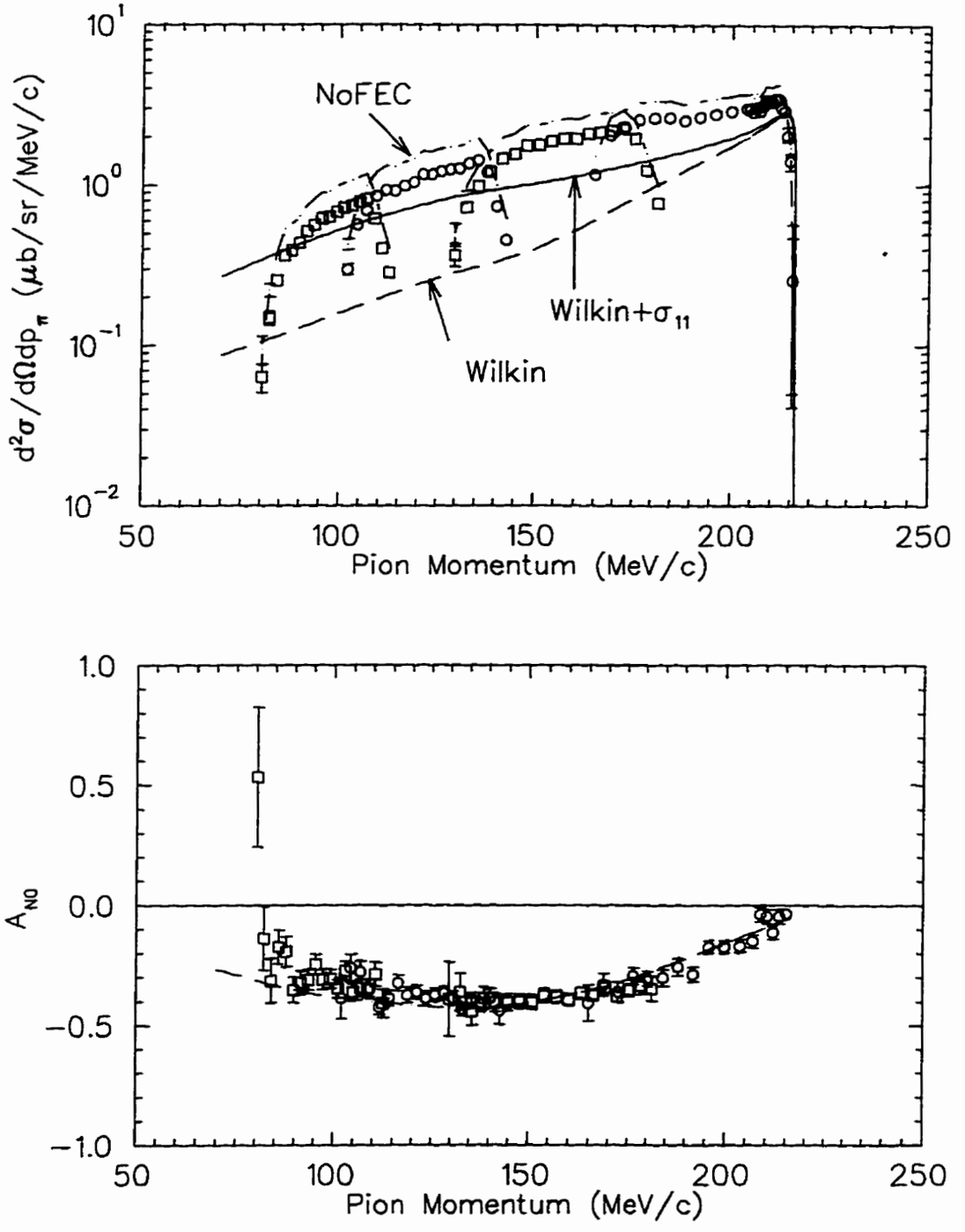

Figure 3.8: Cross sections and analyzing powers for $pp \rightarrow pn\pi^+$. 500 MeV, θ=55.0°, with the predictions of Falk/Wilkin. For the cross section, the Wilkin prediction is also shown with a σ_{11} term added. The cross section results have been scaled down from the cross sections calculated without FEC data.

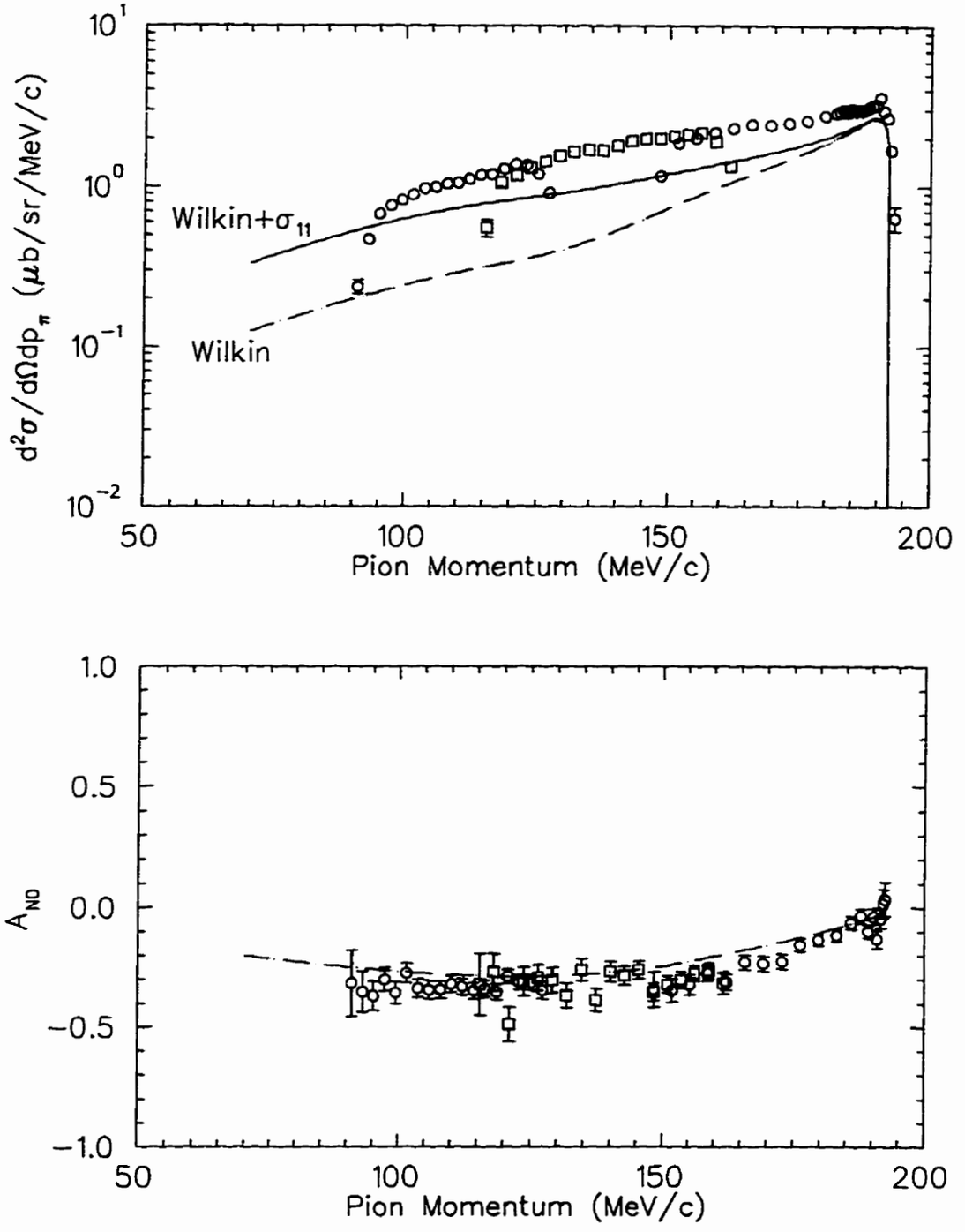

Figure 3.9: Cross sections and analyzing powers for $pp \rightarrow pn\pi^+$. 500 MeV, θ=65.1°, with the predictions of Falk/Wilkin. For the cross section, the Wilkin prediction is also shown with a σ_{11} term added.

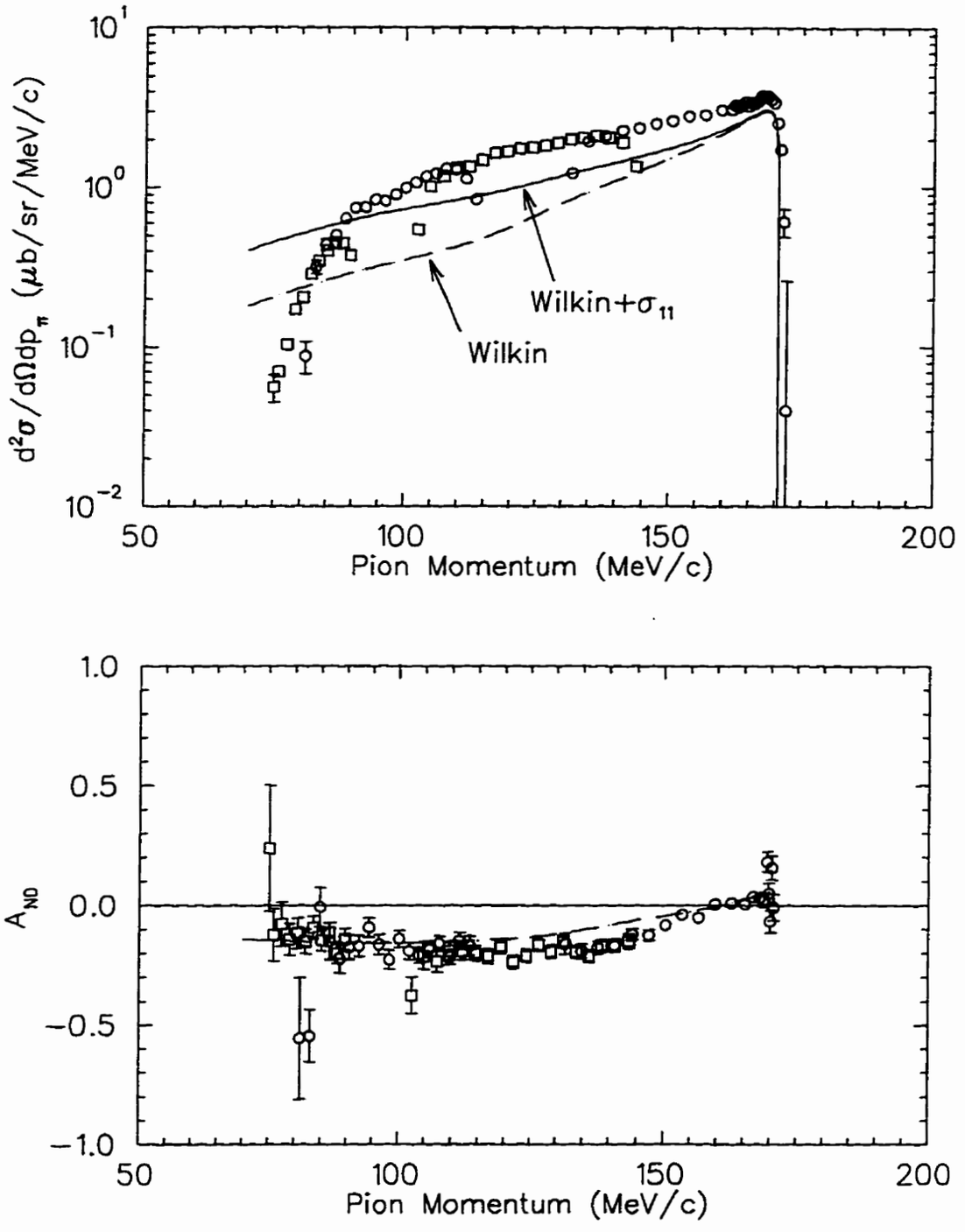

Figure 3.10: Cross sections and analyzing powers for $pp \rightarrow pn\pi^+$. 500 MeV, θ=75.2°, with the predictions of Falk/Wilkin. For the cross section, the Wilkin prediction is also shown with a σ_{11} term added.

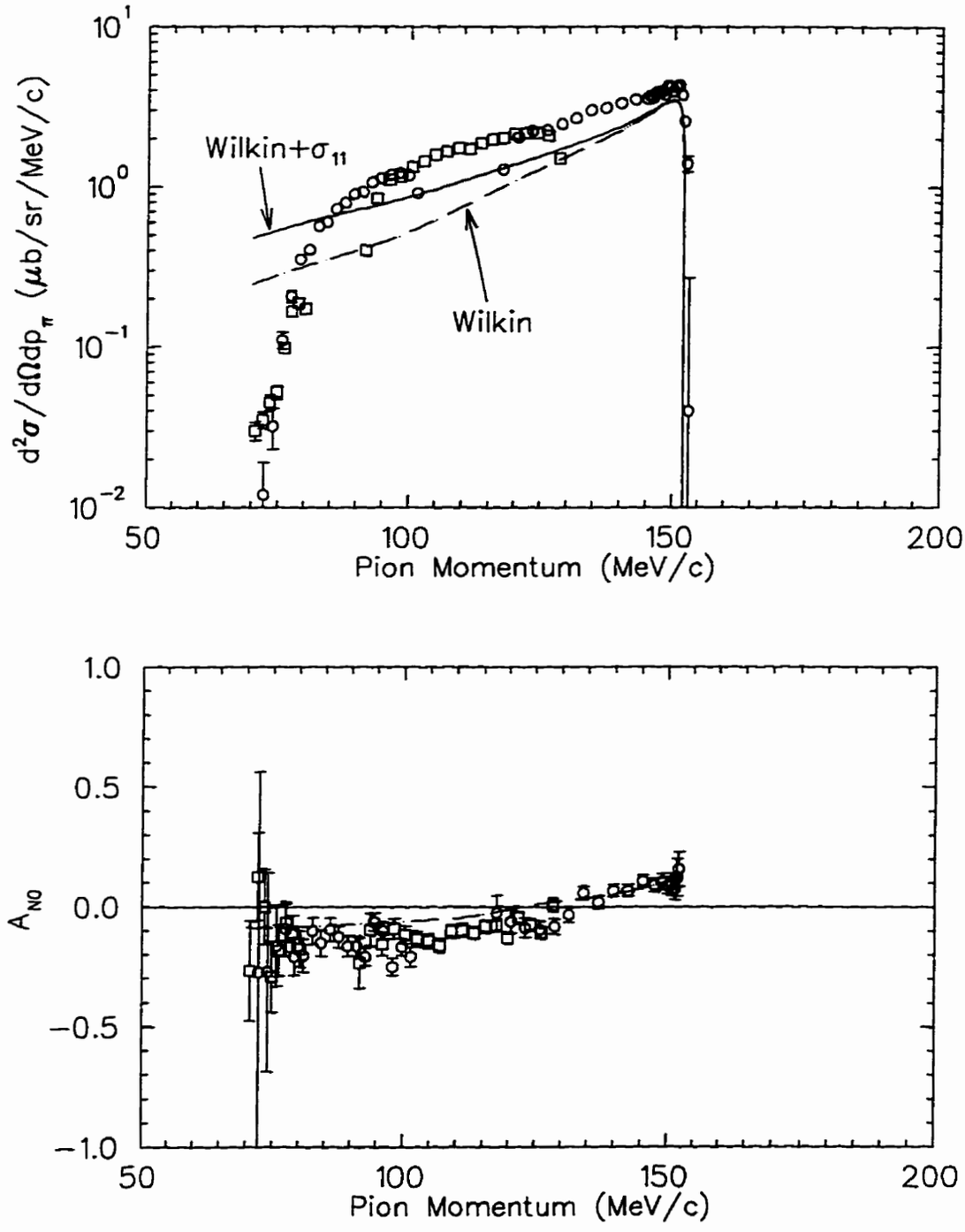

Figure 3.11: Cross sections and analyzing powers for $pp \rightarrow pn\pi^+$. 500 MeV, θ=85.1°, with the predictions of Falk/Wilkin. For the cross section, the Wilkin prediction is also shown with a σ_{11} term added.

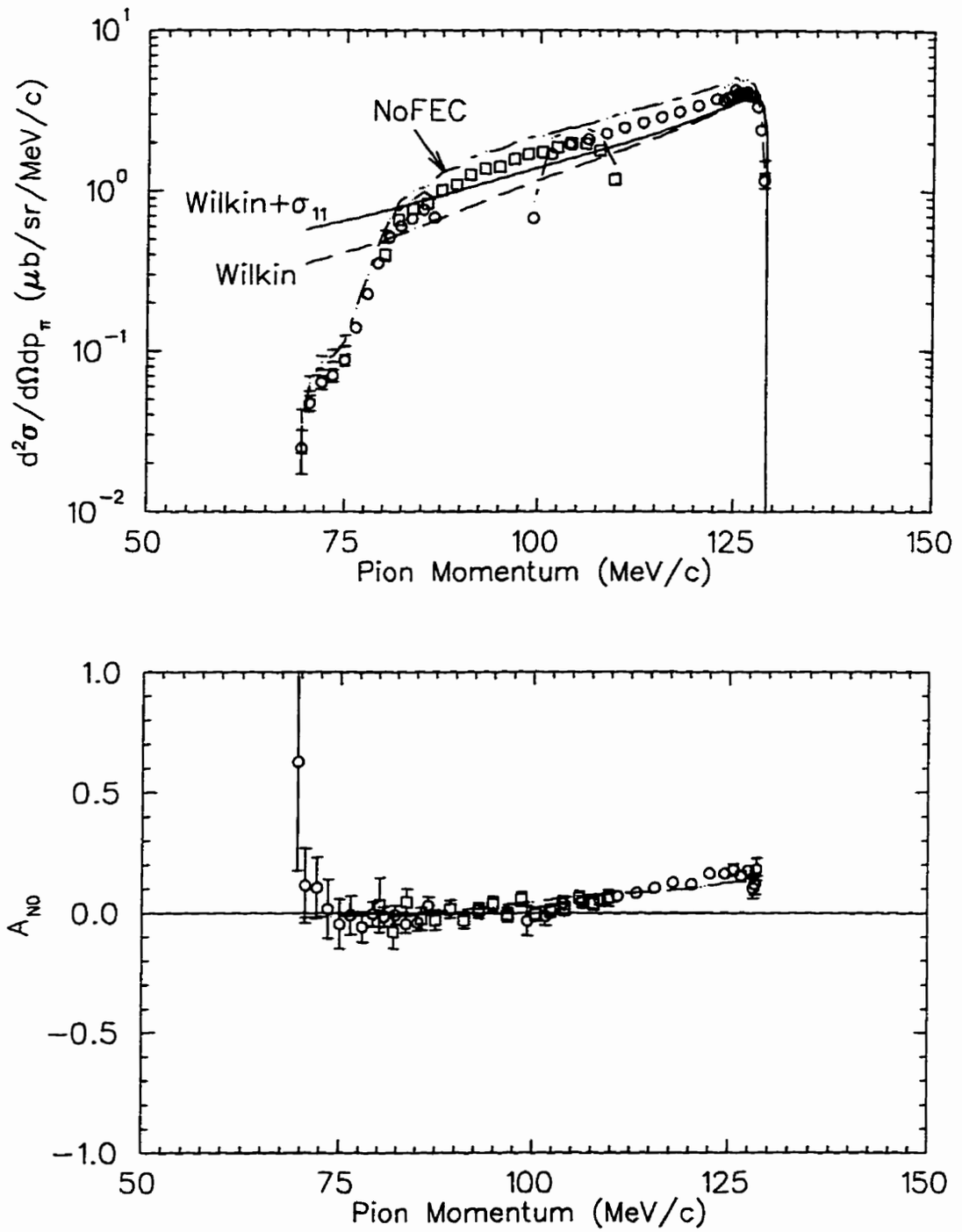

Figure 3.12: Cross sections and analyzing powers for $pp \rightarrow pn\pi^+$. 500 MeV, θ=100.0°, with the predictions of Falk/Wilkin. For the cross section, the Wilkin prediction is also shown with a σ_{11} term added. The cross section results were scaled down from the cross section calculated without FEC data.

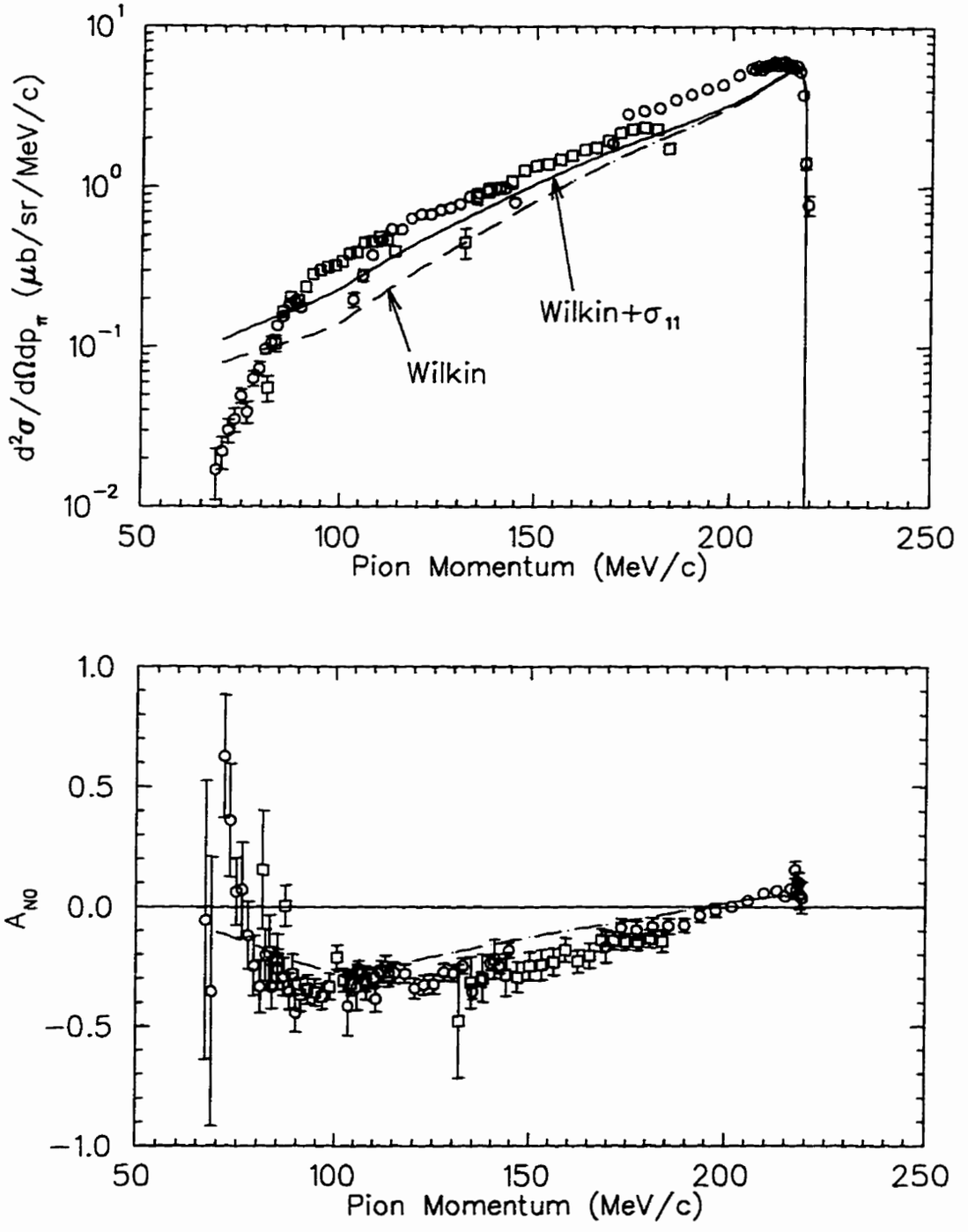

Figure 3.13: Cross sections and analyzing powers for $pp \rightarrow pn\pi^+$. 420 MeV, θ=25.1°, with the predictions of Falk/Wilkin. For the cross section, the Wilkin prediction is also shown with a σ_{11} term added.

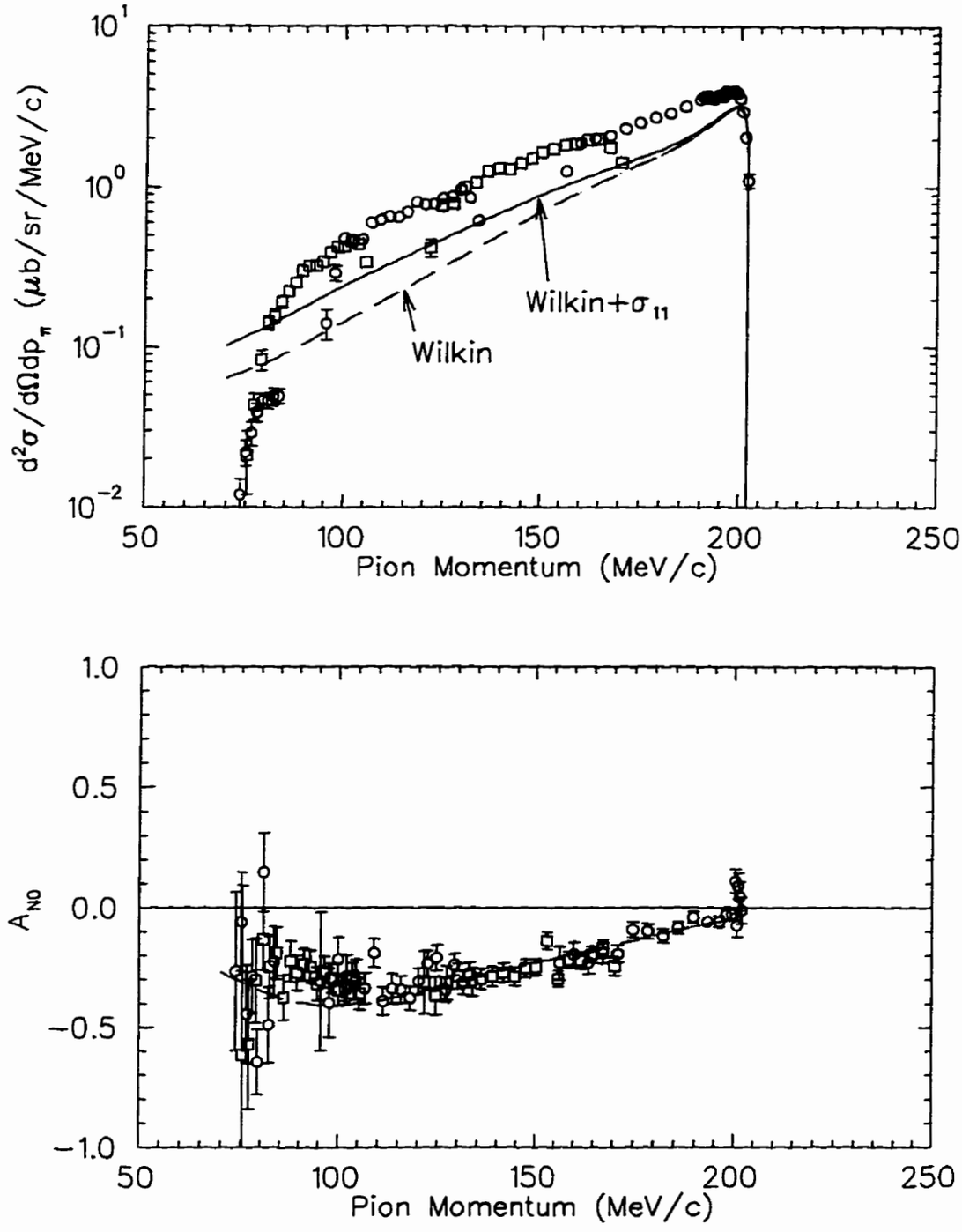

Figure 3.14: Cross sections and analyzing powers for $pp \rightarrow pn\pi^+$. 420 MeV, θ=34.9°. with the predictions of Falk/Wilkin. For the cross section, the Wilkin prediction is also shown with a σ_{11} term added.

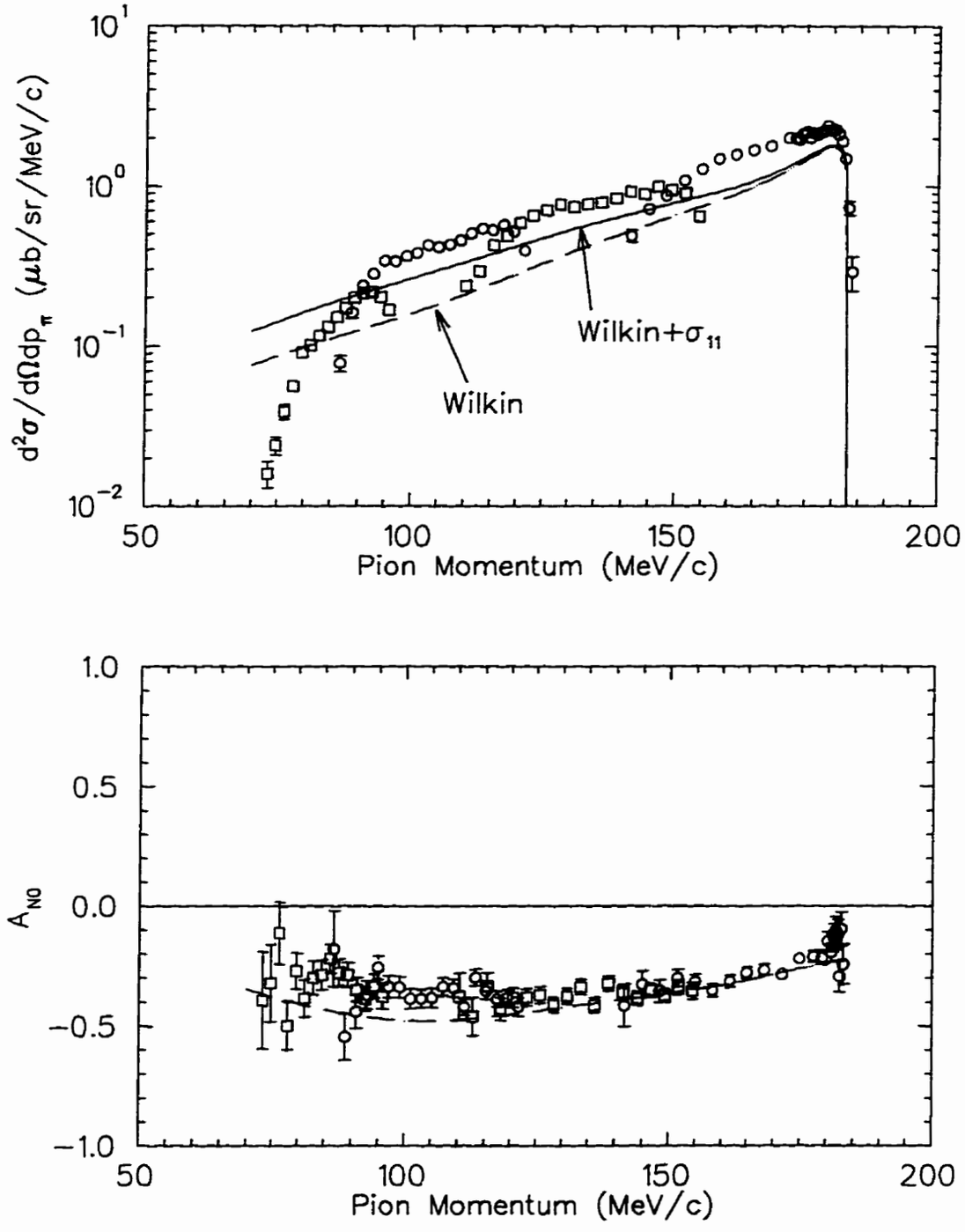

Figure 3.15: Cross sections and analyzing powers for $pp \rightarrow pn\pi^+$. 420 MeV, θ=45.0°, with the predictions of Falk/Wilkin. For the cross section, the Wilkin prediction is also shown with a σ_{11} term added.

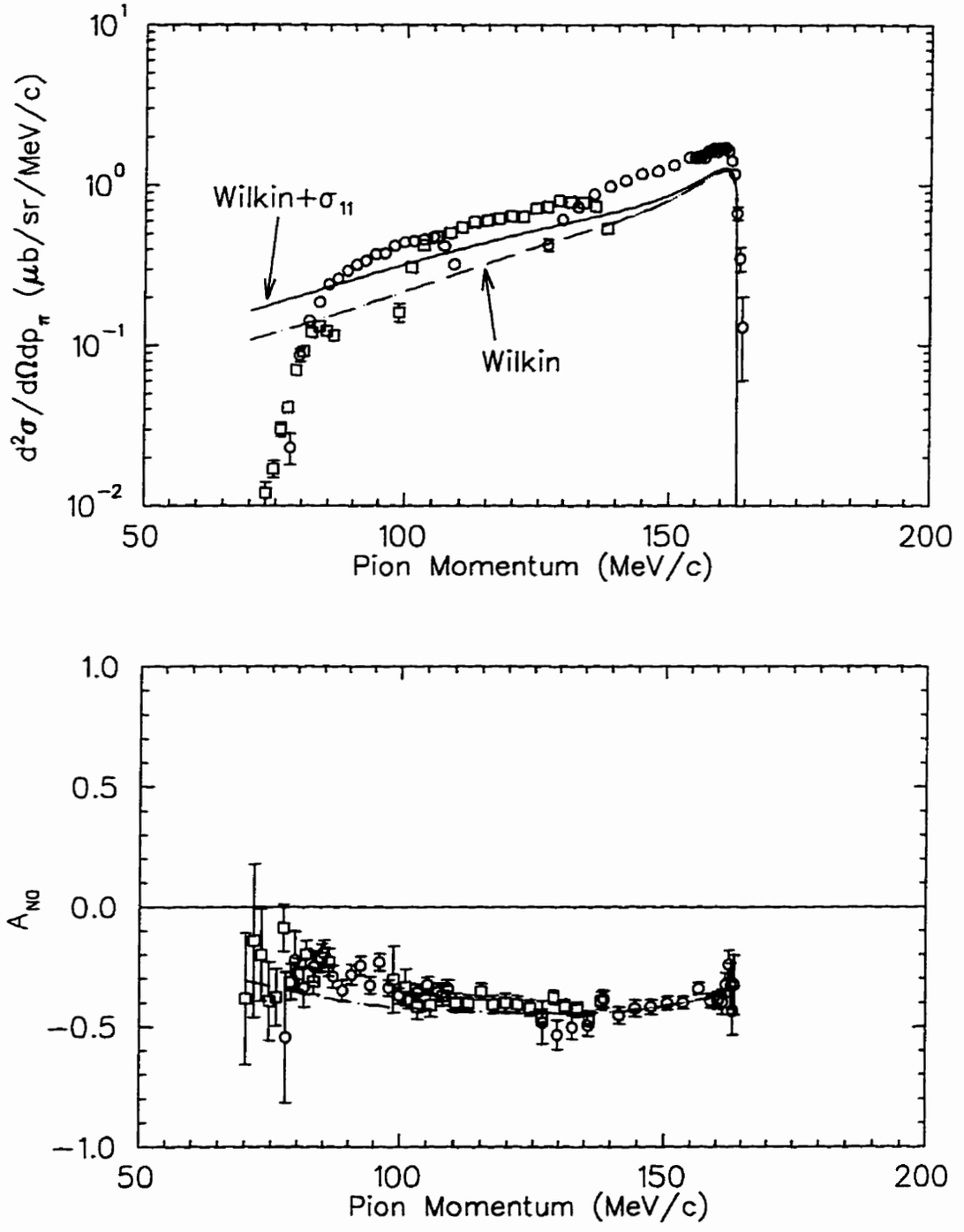

Figure 3.16: Cross sections and analyzing powers for $pp \rightarrow pn\pi^+$. 420 MeV, θ=55.1°, with the predictions of Falk/Wilkin. For the cross section, the Wilkin prediction is also shown with a σ_{11} term added.

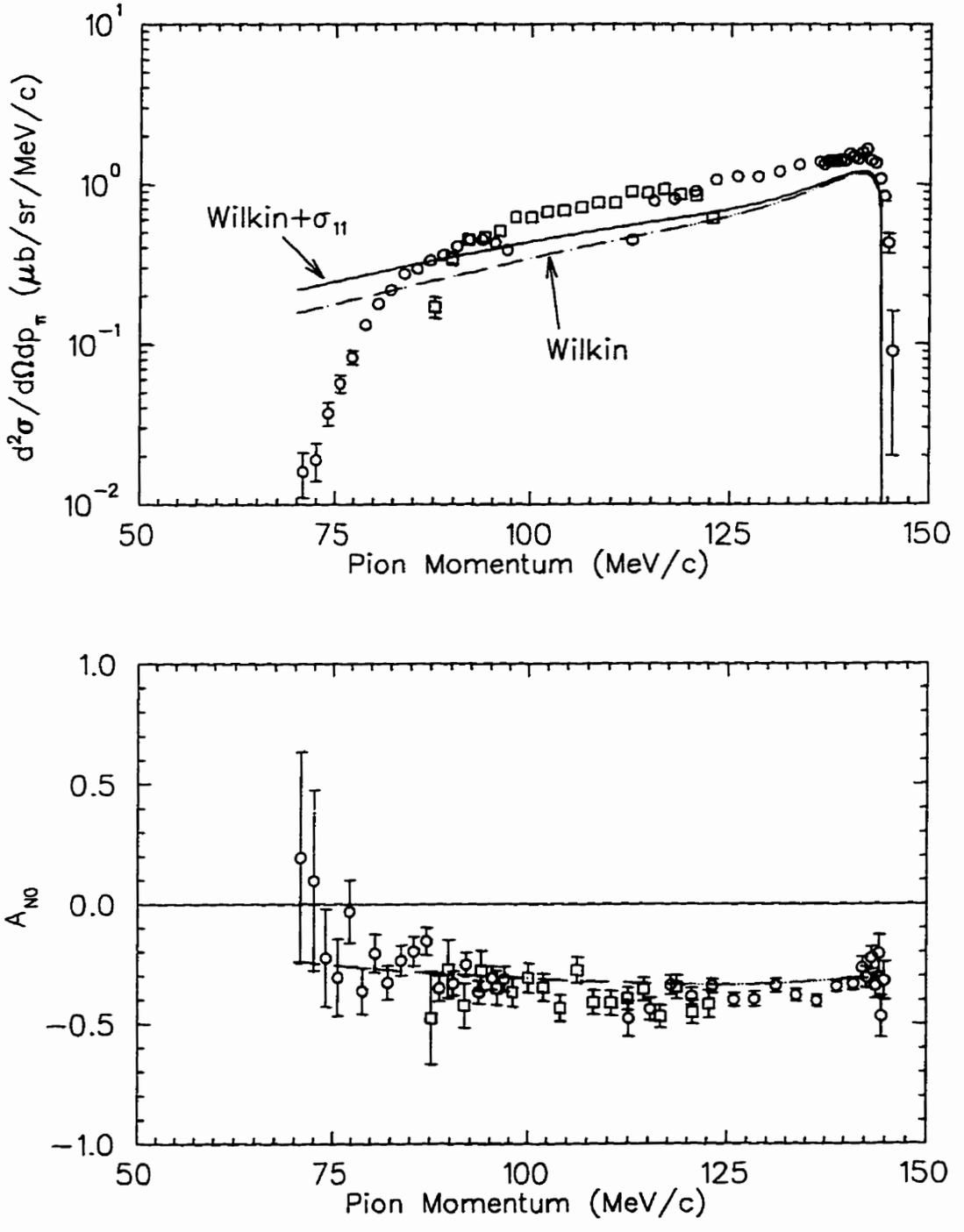

Figure 3.17: Cross sections and analyzing powers for $pp \rightarrow pn\pi^+$. 420 MeV, θ=65.1°, with the predictions of Falk/Wilkin. For the cross section, the Wilkin prediction is also shown with a σ_{11} term added.

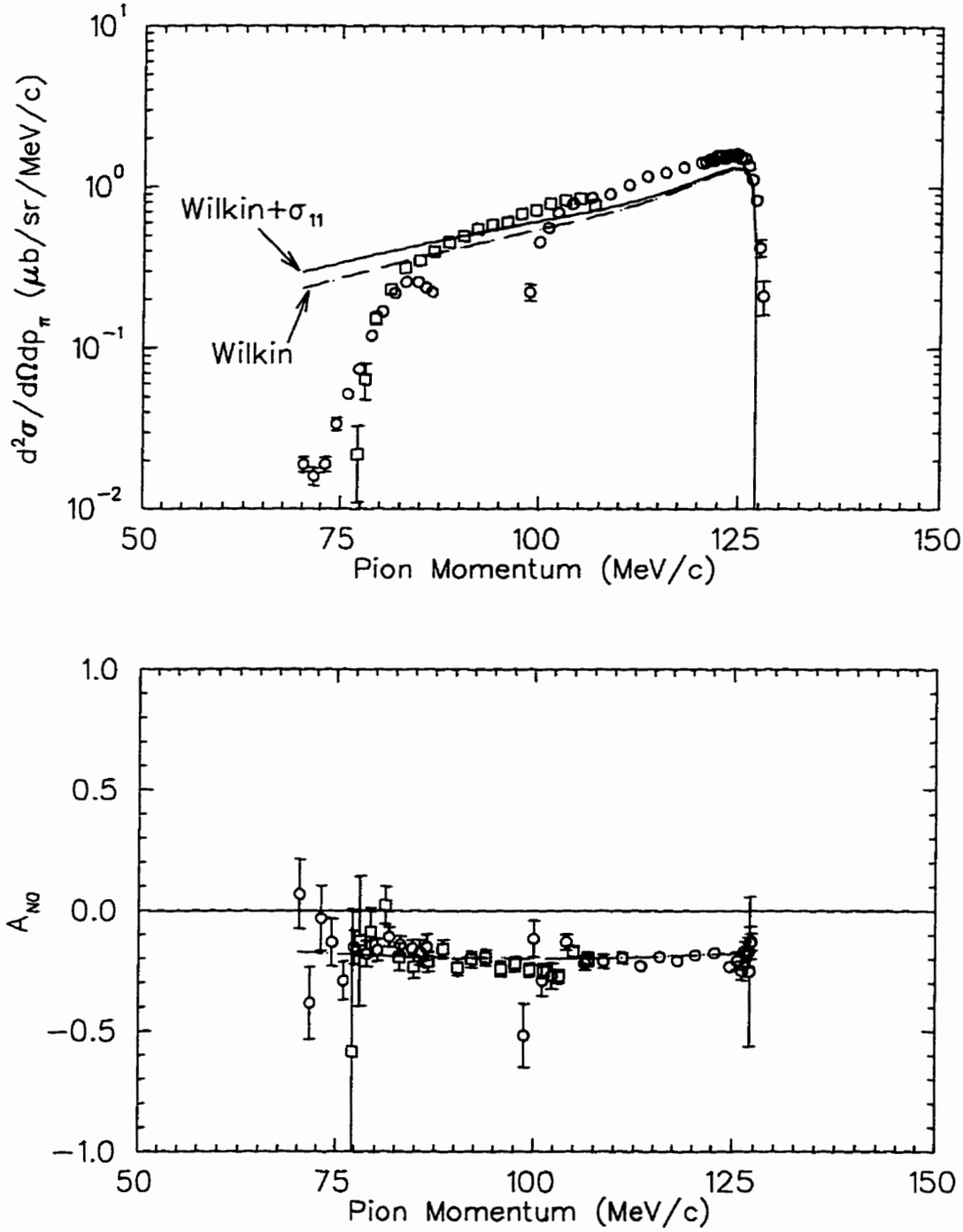

Figure 3.18: Cross sections and analyzing powers for $pp \rightarrow pn\pi^+$. 420 MeV, θ=75.1°, with the predictions of Falk/Wilkin. For the cross section, the Wilkin prediction is also shown with a σ_{11} term added.

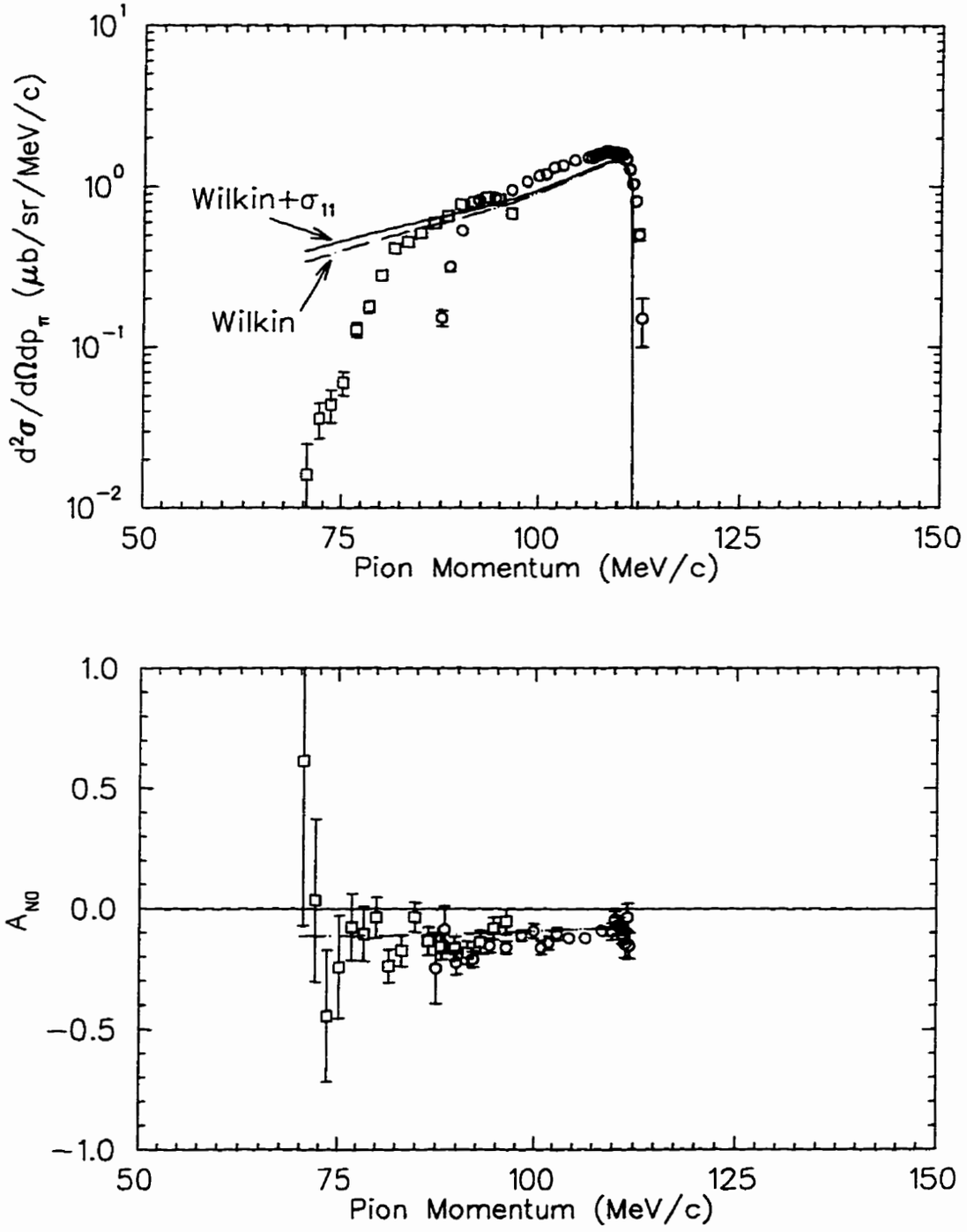

Figure 3.19: Cross sections and analyzing powers for $pp \rightarrow pn\pi^+$. 420 MeV, θ=85.1°, with the predictions of Falk/Wilkin. For the cross section, the Wilkin prediction is also shown with a σ_{11} term added.

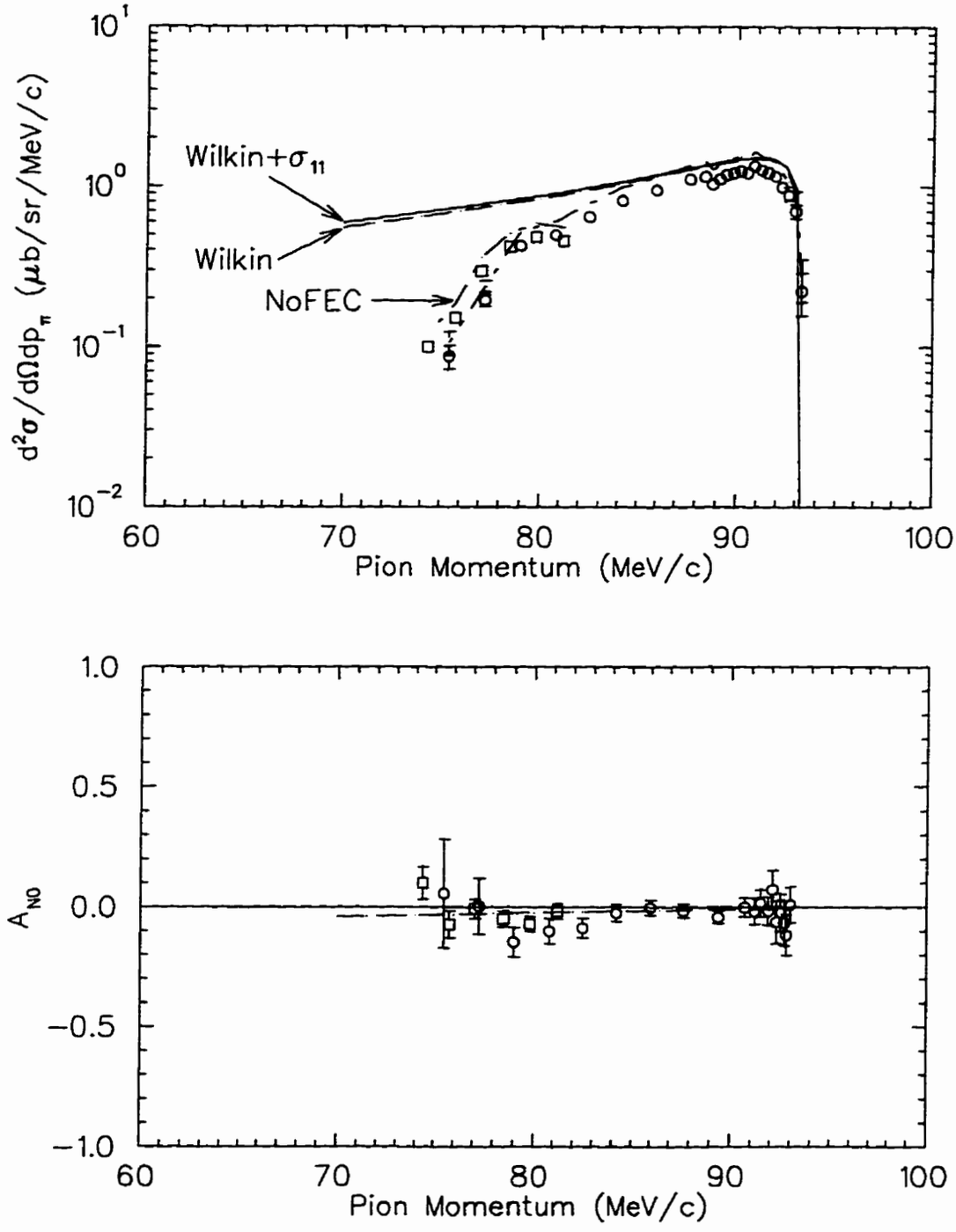

Figure 3.20: Cross sections and analyzing powers for $pp \rightarrow pn\pi^+$. 420 MeV, θ=100.0°. with the predictions of Falk/Wilkin. For the cross section, the Wilkin prediction is also shown with a σ_{11} term added. The cross section results were scaled down from the cross section calculated without FEC data.

Chapter 4

Discussion

4.1 Theory

For reactions such as $pp \rightarrow pn\pi^+$, where there is a final pn pair which can also remain bound as a deuteron, Boudard, Fäldt and Wilkin have related the cross section for the unbound final state to that of the bound final state [22]. Their result is valid so long as the spin singlet pn contribution to the cross section is relatively small. It is known that the cross section for pion production is much greater where the final pn state has quantum numbers S=1, T=0, like the deuteron [23]. The Wilkin cross section relationship is based on the observation that the scattering wave function is proportional to the bound state wave function when extrapolated to the bound state pole, which leads to an amplitude estimate for pion production:

$$M(pp \rightarrow \pi^+\{np\}_k) \approx -\sqrt{\frac{2\pi m}{\alpha_t(k^2+\alpha_t^2)}}e^{-i\delta}M(pp \rightarrow \pi^+ d). \qquad (4.1)$$

Here $\alpha_t = \sqrt{m\epsilon}$, where m is the average nucleon mass, ϵ is the deuteron binding energy, and δ is the uncoupled S-wave triplet phase shift at relative momentum $\vec{k}$. Thus, we have an expression relating the $pp \rightarrow pn\pi^+$ amplitude to the well-known $pp \rightarrow d\pi^+$ amplitude, parameterized in terms of the relative momentum of the pn pair. Introducing the above expression into phase space, one can predict the spin-triplet contribution to the differential cross section.

The Wilkin cross section predictions assume the dominance of the σ_{10} term. Contributions from the σ_{11} term have also been estimated from the $pp \rightarrow pp\pi^0$ data of

Stanislaus *et. al* [24].

Analysing powers may be calculated using the same formalism. The centre of mass energy and angle used in calculations are not those fixed by the beam energy, which would lead to analyzing powers which remain nearly constant across the range of pion momenta. Instead c. m. energies and angles are based on the $pp \rightarrow d\pi^+$ reaction corresponding to the same pion momentum. This procedure was first applied to the interpretation of the $pp \rightarrow pn\pi^+$ data at 400 and 450 MeV [5]. This will be referred to as the Falk/Wilkin model. The resulting A_{N0} are strongly dependent on pion momentum.

Our 'accepted' values for the $pp \rightarrow d\pi^+$ cross sections come from experimental data of Bugg *et al.* [25]. The amplitudes were parameterized for some model calculations of the $A(p,\pi^+)B$ reaction discussed in reference [26]. The predicted cross sections and analyzing powers have been compared with calculations from SAID. At 420 MeV the cross sections are typically within 1% to 4% of each other, and the A_{N0} differ by ~ 0.02. At 500 MeV the results are better, with cross section agreement at the 1% level, and the A_{N0} again differing by ~ 0.02.

4.2 Comparison of experimental results with theory

4.2.1 $pp \rightarrow d\pi^+$

Measured cross sections for $pp \rightarrow d\pi^+$ are shown together with accepted values in figure 3.4. The measured quantities (where the FEC data have been used) are on average 3% high at 500 MeV, and 12% high at 420 MeV. The former result is in good agreement with the estimated 6% uncertainty in the overall normalization (see Systematic Error, section 3.1.6), but our results are outside this limit at 420 MeV. However, it was noted earlier (section 2.1.4) that there was an unresolved beam normalization discrepancy of 6% between 500 MeV and 420 MeV. This implied that the 420 MeV cross sections could be 6% too high. This could account for much of the remaining difference between the measured and accepted values of $pp \rightarrow d\pi^+$ cross section.

Results for the $pp \rightarrow d\pi^+$ reaction cross sections can be used for normalizing the $pp \rightarrow pn\pi^+$ curves, but this was not done in this paper.

4.2.2 $pp \rightarrow pn\pi^+$

The Wilkin formalism was used to calculate cross sections at the reaction angles of E633, using a parameterization of accepted $pp \rightarrow d\pi^+$ cross sections [26]. These predictions are shown in figures 3.5 through 3.20 as dashed lines in the cross section plots. The solid lines are the Wilkin predictions plus the estimated σ_{11} contribution. Generally, the Wilkin cross sections decrease at lower momenta much faster than the observed ones; the σ_{11} contribution brings the predicted slope into better qualitative agreement with the observations, but the cross section is consistently underpredicted, except at 420 MeV, reaction angle 100°.

For all angles and beam energies, we observed a clear termination of the pion momentum continuum, represented by a sharp decline in cross section, at between 80 and 100 MeV/c. Results at the high end of the continuum were generally consistent with those from earlier measurements at 400 and 450 MeV [5].

Although the results from the edges of each momentum bite (which go beyond the design SASP acceptance) diverge, their is sufficient overlap to show good continuity in observed cross section curves in almost all cases.

Analyzing powers from the Falk/Wilkin model are shown as dashed lines with the experimental results in section 3.2. At 500 MeV, the predictions show good consistency with the observed values, generally following their clear and smooth momentum dependence. At 420 MeV, the observed A_{N0} curves show less momentum dependence (this tendency was also observed in previous measurements in this energy range [5]); Falk/Wilkin curves are again consistent with the measured quantities. Observed analyzing powers show continuity between $pp \rightarrow pn\pi^+$ and $pp \rightarrow d\pi^+$, and agreement with the accepted values for the latter.

Chapter 5

Conclusions

5.1 Recommendations

Problems during data-taking consisted of simple oversights or technical difficulties such as missing wires in a VDC. The experimental procedure itself was sound. There remain a number of issues to be resolved in data analysis:

- The muon population predictions of MUON_MC.FOR should be further tested, and the program refined, since agreement with observed muon cross sections was not uniformly good.
- The optical aberrations which the NOVA userfunction USRL was designed to correct are evidently not independent of SASP dipole field strength, as has been assumed.
- A better algorithm for reconstructing y_i would make it possible to remove more junk events and muons.

5.2 Conclusions

Inclusive measurements of the differential cross sections and analyzing powers in the reaction $pp \rightarrow pn\pi^+$ were made with TRIUMF's SASP spectrometer, at beam energies of 420 and 500 MeV, for reaction angles from 24° to 100°. Corrections were made for muon contamination and, in the cross sections, overlap of pions from the $pp \rightarrow d\pi^+$ reaction.

Agreement of the cross section data with the theory of Wilkin *et al.* is qualitatively good if a contribution for final isospin state 1 is added, but the measured values typically exceed the predictions by 30 to 100%.

A strong momentum dependence was found in the measured analyzing powers, which were generally in agreement with the predictions of the Falk/Wilkin theory.

Cross sections and analyzing powers were consistent with previous measurements in a similar energy range.

Bibliography

[1] S. S. M. Wong. *Introductory Nuclear Physics.* Prentice-Hall, Inc., 1990.

[2] T.S. Bhatia et al. Phys. Rev. **C28**, 2071 (1983).

[3] A.D. Hancock et al. Phys. Rev. **C28**, 2742 (1983).

[4] W.W. Daehnick et al. Phys. Rev. Lett. **74**, 2913 (1995).

[5] W.R. Falk et al. Phys. Rev. **C32**, 1972 (1985).

[6] C.E. Waltham et al. Nucl. Phys. **A433**, 649 (1985).

[7] M. A. Punyasena. PhD thesis, University of Alberta, 1996.

[8] P. Walden. Private communication. TRIUMF.

[9] S. Yen et al. Calibration of beamline 4B2 "George", August 1994. TRIUMF internal document.

[10] The "DASSHELP" on-line VMS help for SASP/MRS/DASS experimenters at TRIUMF.

[11] P.Walden. 4B Polarimeter. TRIUMF internal document.

[12] A. Zelenski. Private communication. TRIUMF.

[13] S. Yen. Optics of the Q-Q-Clamshell Second Arm Spectrometer. TRIUMF Design Note, TRI-DN-88-10, February 1988.

[14] K.L. Brown, F. Rothacker, D.C. Carey, and Ch. Iselin. SLAC-91, 1977.

[15] M. J. Benjamintz. Master's thesis, University of Manitoba, 1996.

[16] P.Walden. The corrected THOFF algorithm. TRIUMF internal document.

[17] M. A. Punyasena, S. Yen, M. Hartig, and Y. Ke. Empirical determination of the focal surface and first order transfer matrix elements of the SASP. TRIUMF, December 1994.

[18] D. C. Carey. *The Optics of Charged Particle Beams.* Harwood Academic Publishers, 1987.

[19] P. Walden. Where is the SASP focal plane? TRIUMF internal document.

[20] P. W. Green. Introduction to the NOVA data analysis system, March 1996. TRIUMF document no. TRI-DNA-91-1.

[21] S. Yen. Nuclear Instruments and Methods **A320**, 493 (1991).

[22] A. Boudard, G. Faldt, and C. Wilkin. Phys. Lett. **B389**, 440 (1996).

[23] B.J. VerWest and R.A. Arndt. Phys. Rev. **C25**, 1979 (1982).

[24] S. Stanislaus et al. Phys. Rev. **C44**, 2287 (1991).

[25] D.V. Bugg, A. Hasan, and R.L. Shypit. Nucl. Phys. **A477**, 546 (1988).

[26] W. R. Falk. Phys. Rev. **C50**, 1574 (1994).

Appendix A

Glossary of variables

ACC The SASP acceptance fraction at a particular momentum deviation (2.3.10).

A_{N0} Analyzing power. The subscript indicates this is for a vertically polarized beam and an unpolarized target (3.1.4). A_c is the analyzing power after the muon contamination correction (3.1.2).

B_{SASP} The SASP dipole magnetic field, in kG (2.3.2).

$d\Omega$ SASP solid angle, in sr (3.1.1).

e IBP beam asymmetry (2.1.3).

E_{det} SASP detector efficiency (2.3.12).

δ A momentum, expressed as the percentage deviation from the SASP central momentum (2.3.2). Our approximations to the true momentum deviation of an event are SDEL_9, SDEL_Z, SDEL_XF, SDEL_XNF, SDEL_RF and SDEL_RNF (*q.v.*).

LAPDSUM The sum of signals from the SASP focal plane scintillator paddles, in arbitrary units. LAPDSUM is measure of the particle's energy loss in the paddles, and hence, its kinetic energy (2.3.8).

LFECMEANTIME A measure of the particle time of flight from the FEC to the focal plane paddles, in ns (2.3.13).

LFEC_OK The logical test of the FEC planes, TRUE when both planes return valid location information for an event (2.3.12).

LMWOK The logical test of all wire chamber planes, TRUE when all planes return valid location information for an event (2.3.12).

LRFTIME The time from a valid focal plane paddle hit to an RF timing pulse, in 0.25 ns units. A relative measure of a particles time of flight through the spectrometer. (2.3.5).

LTOF The time from a FEC signal to a paddle signal, in 0.25 ns units. A measure of absolute time of flight (2.3.5).

LU1POS The U coordinate at VDC1, in 50 μ units (2.3.1).

LU2POS The U coordinate at VDC2, in 50 μ units (2.3.1).

LVDCMEANTIME A measure of the time of flight between the VDCs and the focal plane paddles, in ns (2.3.13).

LVDC_OK The logical test of the VDC planes, TRUE when all four VDC planes return valid location information for and event (2.3.12).

LX0POS The X coordinate at the FEC, in 50 μ units (2.3.1).

LX1POS The X coordinate at VDC1, in 50 μ units (2.3.1).

LX2POS The X coordinate at VDC2, in 50 μ units (2.3.1).

LY0POS The Y coordinate at the FEC, in 50 μ units (2.3.1).

LY1POS The Y coordinate at VDC1, in 50 μ units (2.3.1).

LY2POS The Y coordinate at VDC2, in 50 μ units (2.3.1).

MMF The missing mass of the reaction, calculated using FEC data, in MeV/c^2 (2.3.9).

MMFP The missing mass MMF with the THC (*q.v.*) correction (2.3.9).

MMNF The missing mass of the reaction, calculated without using FEC data, in MeV/c^2 (2.3.9).

n_{live} The computer live time fraction (2.3.11).

n_p The total proton flux in a measurement (3.1.1).

n_t The number of target protons per cm^2, along the beam axis (3.1.1).

P The beam polarization, measured by the IBP (2.1.3).

PHC A correction term applied to MMNF (*q.v.*) (2.3.9).

ϕ_f The non-bend plane angle of the particle trajectory at the focal plane, in mrad; a Transport coordinate (2.3.1,2.3.3). Our calculation of ϕ_f is SPHF (*q.v.*).

ϕ_i The non-bend plane angle of the particle trajectory at the target, in mrad; a Transport coordinate (2.3.1). Approximations to ϕ_f include SPHI_P3, SPHI_P5 and SPHI_L3 (*q.v.*).

Rnn Elements of the transfer matrix, SRMATRIX (2.3.3).

SDEL_9 Our first approximation to the percentage momentum deviation δ (*q.v.*) of a particle (2.3.2).

SDEL_RF The momentum deviation SDEL_XF (*q.v.*), after correction for energy loss in the target (2.2.1).

SDEL_RNF The momentum deviation SDEL_XNF (*q.v.*), after correction for energy loss in the target (2.2.1).

SDEL_XF The percentage momentum deviation for a detected pion, extracted at the nominal reaction angle from MMF (*q.v.*).

SDEL_XNF The percentage momentum deviation for a detected pion, extracted at the nominal reaction angle from MMNF (*q.v.*).

σ Cross section, in μb (3.1.1). Sometimes used to represent the differential cross section $\frac{d^2\sigma}{d\Omega dp}$; units are $\frac{\mu b}{sr \cdot MeV/c}$ (3.1.5). σ_m is the measured differential cross section; σ_c is σ_m after corrections for muon contamination (3.1.2).

SPHF The non-bend plane angle of the particle trajectory at the focal plane in mrad, calculated from VDC position data; a Transport coordinate (2.3.1,2.3.2).

SPHI_L3 The non-bend plane angle of the particle trajectory at the target in mrad. calculated by applying higher order aberration corrections to SPHI_P3 (*q.v.*); a Transport coordinate (2.3.1,2.3.7).

SPHI_P3 The non-bend plane angle of the particle trajectory at the target in mrad. calculated with VDC position information and the transfer matrix; a Transport coordinate (2.3.1).

SPHI_P5 The non-bend plane angle of the particle trajectory at the target in mrad. calculated from FEC position information; a Transport coordinate (2.3.1).

STHFCN The bend plane angle of the particle trajectory at the focal plane in mrad. calculated with VDC position information; a Transport coordinate (2.3.1).

STHI_L3 The bend plane angle of the particle trajectory at the target in mrad, calculated by applying higher order aberration corrections to STHI_P3 (*q.v.*); a Transport coordinate (2.3.1,2.3.7).

STHI_P3 The bend plane angle of the particle trajectory at the target in mrad, calculated with VDC position information and the transfer matrix; a Transport coordinate (2.3.1).

SURV The pion survival fraction in SASP, a function of the effective path length EFF_L, which is determined by the dipole field and the pion momentum (2.3.10).

SX0_TR The X coordinate of the particle trajectory at the FEC, in 50 μm units (2.3.1).

SXF The X coordinate of the particle trajectory at the focal plane in cm, calculated from VDC position information; a Transport coordinate (2.3.1,2.3.2). SXFC is SXF plus higher order aberration corrections 2.3.7.

SXI_L3 The X coordinate of the particle trajectory at the target, in cm, calculated from FEC information and STHI_L3 (*q.v.*); a Transport coordinate (2.3.1).

SX0_TR The X coordinate of the particle trajectory at the FEC, in 50 μm units (2.3.1).

SYI_F The Y coordinate of the particle trajectory at the target, in cm, calculated from FEC and VDC information; a Transport coordinate.

SYL_P The Y coordinate of the particle trajectory at the target, in cm, calculated from VDC information; a Transport coordinate.

SYF The Y coordinate of the particle trajectory at the focal plane in cm, calculated from VDC position information; a Transport coordinate (2.3.1,2.3.2).

SZF The Z coordinate of the particle trajectory at the focal plane in cm, calculated from VDC position information; a Transport coordinate (2.3.1,2.3.2).

θ_f The bend plane angle of the particle trajectory at the focal plane, in mrad; a Transport coordinate (2.3.1,2.3.3). Our calculation of thi_f is STHFCN (*q.v.*).

θ_i The bend plane angle of the particle trajectory at the target, in mrad; a Transport coordinate (2.3.1,2.3.3). Approximations to thi_f include STHI_P3 and STHI_L3 (*q.v.*).

θ_{SASP} The angle of the spectrometer with respect to the beam, in degrees. This is the nominal reaction angle (2.3.1).

θ_{TARGET} The rotation of the target cell with respect to the beam axis, in degrees (2.2.1).

x_f The X coordinate of the particle trajectory at the focal plane, in cm; a Tranport coordinate (2.3.1,2.3.3). Our calculation of x_f is SXF (*q.v.*).

x_i The X coordinate of the particle trajectory at the target, in cm; a Tranport coordinate (2.3.1,2.3.3). Our calculation of x_i is SXI_L3 (*q.v.*).

y_f The Y coordinate of the particle trajectory at the focal plane, in cm; a Tranport coordinate (2.3.1,2.3.3). Our calculation of y_f is SYF (*q.v.*).

y_i The Y coordinate of the particle trajectory at the target, in cm; a Tranport coordinate (2.3.1,2.3.3). Approximations to y_i include SYI_P and SYI_F (*q.v.*).

Appendix B

E633 NOVA off-line OPSEQ

```
( 1)                IF ($EVENTTYPE==1)THEN
( 1)                  IF ($NUMEVIN==1867)GOTO $END_OPSEQ
( 1)                  EVAL RATES
( 1)                  INCR HBEAM BY I_NA
( 1)                  INCR HEVENT BY EVENT_NORM
( 1)                  INCR HFECXO BY FECXO_NORM
( 1)                  INCR HNRSRATE BY NRSRATENORM
( 2)                  IF (IPOLUP>0)THEN
( 2)                    INCR HPOLUP
( 1)                  ENDIF
( 2)                  IF (IPOLDW>0)THEN
( 2)                    INCR HPOLDW
( 1)                  ENDIF
( 1)                  INCR HMYPOL
( 1)                  INCR HTMYPOL
( 1)                  GOTO $END_OPSEQ
( 0)                ENDIF
( 1)                IF ($EVENTTYPE==2)THEN
( 1)                  IF ($NUMEVIN==1867)GOTO $END_OPSEQ
( 1)                  EVAL X1HIT
( 1)                  EVAL X1X2HIT
( 1)                  EVAL PLSRU
( 1)                  EVAL PLSRD
( 1)                  EVAL PLSRO
( 1)                  INCR HSDCR
( 1)                  EVAL LFTFET
( 1)                  EVAL LFTFEV
( 1)                  EVAL LFTFESCINT
( 1)                  INCR HSX1_RAW
( 2)                  IF (LPD4)THEN
( 2)                    EVAL ADD
( 1)                  ENDIF
( 2)                  IF (LVDC_OK)THEN
( 2)                    INCR HSPID_OK
( 3)                    IF (LFECO_OK)THEN
( 3)                      INCR HSXOYO
( 2)                    ENDIF
( 2)                    INCR GSPID_OK
( 2)                    INCR HSRFT_OK
( 2)                    INCR TOFRF
( 2)                    INCR HS60HZPHASE
( 1)                  ENDIF
( 1)                  INCR HSADC
( 1)                  INCR HSPID
```

```
( 1)                INCR GSPID
( 1)                INCR HSRFT
( 1)                INCR HSFETTDC
( 1)                INCR HSFEVTDC
( 2)                IF (LPID)THEN
( 2)                  INCR HSXANG
( 2)                  INCR HSUANG
( 2)                  INCR HSANGPOS
( 2)                  INCR HSX1X2ANG
( 2)                  INCR HSVDCTIME
( 2)                  INCR HSFECTIME
( 2)                  INCR HSDIAG
( 2)                  INCR HSFEGTDC
( 2)                  INCR HSPOS
( 2)                  INCR HSANGLE
( 2)                  INCR HSU1CH
( 2)                  INCR HSU2CH
( 2)                  INCR HSXOCH
( 2)                  INCR HSXOPCH
( 2)                  INCR HSYOCH
( 2)                  INCR HSYOPCH
( 2)                  INCR HSX1CH
( 2)                  INCR HSX2CH
( 3)                  IF (LHX2G)THEN
( 3)                    INCR HSU2G
( 2)                  ENDIF
( 3)                  IF (GAPCON)THEN
( 3)                    EVAL GAPFILL
( 3)                    INCR HRATE
( 2)                  ENDIF
( 3)                  IF (REG1)THEN
( 3)                    EVAL LX2R1
( 3)                    INCR HSX2R1
( 2)                  ENDIF
( 3)                  IF (REG2)THEN
( 3)                    EVAL LX2R2
( 3)                    EVAL LX2R2F
( 3)                    INCR HSX2R2
( 2)                  ENDIF
( 3)                  IF (REG3)THEN
( 3)                    EVAL LX2R3
( 3)                    INCR HSX2R3
( 2)                  ENDIF
( 2)                  INCR HSX2G
( 2)                  EVAL LVDCCON_B
( 2)                  EVAL LFECOCON_B
( 2)                  EVAL LHWOK_B
( 3)                  IF (SPIN_UP)THEN
( 3)                    EVAL LVDCCON_UP
( 3)                    EVAL LFECOCON_UP
( 3)                    EVAL LHWOK_UP
( 2)                  ENDIF
( 3)                  IF (SPIN_DOWN)THEN
( 3)                    EVAL LVDCCON_DN
( 3)                    EVAL LFECOCON_DN
( 3)                    EVAL LHWOK_DN
( 2)                  ENDIF
( 3)                  IF (FEC_OR)THEN
( 3)                    EVAL LVDCCON_BA_F
( 3)                    EVAL LFECCON_BA_F
( 3)                    EVAL LHWOK_B_F
( 4)                    IF (SPIN_UP)THEN
( 4)                      EVAL LVDCCON_UP_F
( 4)                      EVAL LFECCON_UP_F
( 4)                      EVAL LHWOK_UP_F
( 3)                    ENDIF
```

```
( 4)                    IF (SPIN_DOWN)THEN
( 4)                      EVAL LVDCCON_DN_F
( 4)                      EVAL LFECCON_DN_F
( 4)                      EVAL LNNOK_DN_F
( 3)                    ENDIF
( 2)                  ENDIF
( 3)                  IF (LVDC_OK2)THEN
( 3)                    INCR HSDEL_9
( 4)                    IF (DELCUT)THEN
( 4)                      INCR HSTHIPHI_NF
( 4)                      EVAL LFAILS
( 4)                      INCR HSXF
( 4)                      INCR HSXFZ
( 4)                      INCR HSYF
( 4)                      INCR HSDEL_Z
( 4)                      INCR HSDELRF
( 4)                      INCR HSDELYF
( 4)                      INCR HSTHF
( 4)                      INCR HSDELPHI
( 4)                      INCR HSXFPHI
( 4)                      INCR HSXFZPHI
( 5)                      IF (LVDCNTWIND)THEN
( 6)                        IF (LCTHI_L3)THEN
( 6)                          INCR HSTHFCN
( 7)                          IF (LCTHFCN)THEN
( 8)                            IF (LCPHI_L3)THEN
( 8)                              INCR HSPHFNF
( 8)                              EVAL LCPHFNF
( 8)                              INCR HSYINF
( 8)                              EVAL SYINFCUT
( 8)                              INCR HSDELNF
( 8)                              INCR HSDELNF1
( 8)                              INCR HSDELNF1_AS BY ACCSURV
( 8)                              INCR HSDELNF_SN BY SURVNORM
( 8)                              INCR HSDELNF_AS BY ACCSURV
( 8)                              INCR HDRMNFC
( 8)                              INCR HDRMNFC1
( 8)                              INCR HDELNFTARG
( 8)                              INCR HDRMNFTARG
( 8)                              INCR HCORNF
( 9)                              IF (SPIN_UP)THEN
( 9)                                INCR HSDELNFUP
( 9)                                INCR HSDELNFUP_SN BY SURVNORM
( 9)                                INCR HSDELNFUP_AS BY ACCSURV
( 9)                                INCR HDRMNF_DU BY    -1.000000
( 8)                              ENDIF
( 9)                              IF (SPIN_DOWN)THEN
( 9)                                INCR HSDELNFDN
( 9)                                INCR HSDELNFDN_SN BY SURVNORM
( 9)                                INCR HSDELNFDN_AS BY ACCSURV
( 9)                                INCR HDRMNF_DU
( 8)                              ENDIF
( 7)                            ENDIF
( 8)                            IF (LFECO_OK)THEN
( 9)                              IF (LFECNTWIND)THEN
( 9)                                INCR HSPHI_FEC
( 9)                                INCR HSXI_L3
(10)                                IF (SXICUT)THEN
(11)                                  IF (LCPHI_P5)THEN
(11)                                  INCR HSPHFF
(11)                                  EVAL LCPHFF
(11)                                  INCR HSYI_F
(11)                                  INCR HSYIFRF
(11)                                  EVAL SYIFCUT
(11)                                  INCR HSDELF
(11)                                  INCR HSDELF1
```

```
(11)                                INCR HSDELF1_AS BY ACCSURV
(11)                                INCR HSDELF_SH BY SURVHORM
(11)                                INCR HSDELF_AS BY ACCSURV
(11)                                INCR HDRMFC
(11)                                INCR HDRMFC1
(11)                                INCR HDELFTARG
(11)                                INCR HDRMFTARG
(11)                                INCR HCORF
(12)                                IF (SPIN_UP)THEN
(12)                                INCR HSDELFUP
(12)                                INCR HSDELFUP_SH BY SURVHORM
(12)                                INCR HSDELFUP_AS BY ACCSURV
(12)                                INCR HDRMF_DU BY   -1.000000
(11)                                ENDIF
(12)                                IF (SPIN_DOWN)THEN
(12)                                INCR HSDELFDN
(12)                                INCR HSDELFDN_SH BY SURVHORM
(12)                                INCR HSDELFDN_AS BY ACCSURV
(12)                                INCR HDRMF_DU
(11)                                ENDIF
(10)                                ENDIF
( 9)                              ENDIF
( 8)                            ENDIF
( 7)                          ENDIF
( 6)                        ENDIF
( 5)                      ENDIF
( 4)                    ENDIF
( 3)                  ENDIF
( 2)                ENDIF
( 1)              ENDIF
( 0)            ENDIF
EOF
```

Appendix C

The E633_ANAL.FOR program

```
C Program E633_ANAL.FOR, for analyzing E633 output from NOVA
C W.R. FALK, Jan. 24, 1997
C (Starting with E634 file E634_ANAL.FOR, dated July 12, 1995)
C LINK : E633_ANAL+FEC_VDC+POL_OFF
C
IMPLICIT REAL*8(A-H,O-Z)
DIMENSION A(2,2,6,900),S(112),UF(900),NHH(2),PPI(2),B(2),
1 THETAS(2),THETAT(2),IBP(2),NTG(2),BUSY(2),EVENT(2),RTRIGS(2),
2 POLLTU(2),POLRTU(2),POLLAU(2),POLRAU(2),EVU(2),SEMU(2),
3 T6OU(2),CLU(2),POLLTD(2),POLRTD(2),POLLAD(2),POLRAD(2),EVD(2),
4 SEMD(2),T6OD(2),CLD(2),
5 COMP_LIVE(2),ECO_L(2),UP_LIVE(2),EUP_L(2),DN_LIVE(2),EDN_L(2),
6 ASYMM_UP(2),ASYMM_DN(2),PUP(2),EUP(2),PDN(2),EDN(2),
7 POLU(2),EPOLU(2),POLD(2),EPOLD(2),POL_RAT(2),POL_SEM(2),
8 SEM_RAT(2),PROT_UP(2),EP_UP(2),PROT_DN(2),EP_DN(2),EP_TO(2),
9 Tmin(2),CURRENT_UP(2),CURRENT_DN(2),CURRENT_AV(2),
1 RTO(2,2),RUP(2,2),RDN(2,2),SEMU_C(2),SEMD_C(2),POL_CORR(2),
2 EE_TO(2,2),EE_UP(2,2),EE_DN(2,2),
3 NCH(2,50),DEL1(2,50),DEL2(2,50),P1(2,50),P2(2,50),
4 P_INT(2,50),P_AV(2,50),NBOUND(2),NINT(2),
5 SUM(2,2,6,50),Y(2,2,6,50),EY(2,2,6,50),SIGO(2,50),dSIGO(2,50),
6 SIGU(2,50),dSIGU(2,50),SIGD(2,50),dSIGD(2,50),SIGA(2,50),
7 dSIGA(2,50),ANO(2,50),dANO(2,50),SIG_BKD(2,50),
8 LPID1(2),LPID2(2),NTRY(2,2,6),FECVDC_A(2,2,3),EFF_A(2,2,54),
9 Tsec(2),FECIO(2),VDCK1(2),PADD0(2),PADD1(2),PADD2(2),PADD3(2),
1 PADD4(2),RSLO(2),RSHI(2),REVENT(2),RBUSY(2),RPID1(2),RPID2(2)
C
COMMON/EFFICIENCY/NTRY(2,6),FECVDC(2,3),EFF(2,54),FEC(2,3),
1 EFEC(2,3),VDC(2,3),EVDC(2,3),FV(2,2,3),EFV(2,2,3)
C-----------------------------------------------------------------------
C ARRAYS :
C V(I) : I=1, FOREGROUND RUN   I=2, BACKGROUND RUN
C
C Z(I,J,K,L) :   I=1, FOREGROUND RUN   I=2, BACKGROUND RUN
C J=1, NO FEC J=2, WITH FEC
C K=1-6 SPECTRA
C L= CHANNEL # (1-900)
C-----------------------------------------------------------------------
C
C INPUT: UNIT 2 - Input file E633_RUNS.
C UNIT 3 - Input file E633_SCAL.
C UNIT 4 - Input file E633_EFFS.
C UNIT 5 - Input file ANAL#., where # is run number
C
C INPUT UNITS for SWRITE files from NOVA. nnn is the RUN #
C       FOREGROUND      BACKGROUND
C       ----------      ----------
```

```
C HSDELNFnnn.SWR FOR011 FOR023       \
C HSDELNFUPnnn.SWR FOR012 FOR024      |
C HSDELNFDNnnn.SWR FOR013 FOR025      | NO
C HSDELNF_ASnnn.SWR FOR014 FOR026     | FEC
C HSDELNFUP_ASnnn.SWR FOR015 FOR027   |
C HSDELNFDN_ASnnn.SWR FOR016 FOR028   /
C
C HSDELFnnn.SWR FOR017 FOR029       \
C HSDELFUPnnn.SWR FOR018 FOR030      |
C HSDELFDNnnn.SWR FOR019 FOR031      | WITH
C HSDELF_ASnnn.SWR FOR020 FOR032     | FEC
C HSDELFUP_ASnnn.SWR FOR021 FOR033   |
C HSDELFDN_ASnnn.SWR FOR022 FOR034   /
C
C OUTPUT: UNIT 6 - All input information and final results
C UNIT 7 - Summary of final results, NO FEC
C UNIT 8 - Summary of final results, WITH FEC
C UNIT 9 - Spectra for PLOTDATA plots (spectra from units 11-34)
C
C-----------------------------------------------------------------------
RAD=57.296
NX=900 ! Number of channels in SWRITE spectra
DEL_LO=-16.0 ! Low SDEL limit for SWRITE spectra
DEL_HI=20.0 ! High SDEL limit for SWRITE spectra
dWSASP=0.0135 ! SASP solid angle, sr
C-----------------------------------------------------------------------
C
C NFRUN = Foreground Run number (search for this in next READ)
C NBRUN = Background Run number (search for this in next READ)
C       = 0, No background run available
C IFEC = 0, Analysis carried out for NO FEC case only
C        1, Analysis carried out for NO FEC and WITH FEC cases
C IPRI is a print control in SUBROUTINE FEC_VDC (normally=0)
C NBOUND = Number of channel boundaries for binning data
C  (50 max). Number of intervals (or bins) = NBOUND-1
C     NBOUND(1) : NO FEC , >2
C     NBOUND(2) : WITH FEC , >2
C NCH(J,I) = Channel boundaries in SDEL spectra (50 max),
C     for NO FEC (J=1), and WITH FEC (J=2)
C
        READ(5,*) NFRUN,NBRUN,IFEC,IPRI,NBOUND(1),NBOUND(2)
C
        IMAX=2
        IF(NBRUN.EQ.0) IMAX=1
        JFEC=IFEC+1
NINT(1)=NBOUND(1)-1
        NINT(2)=NBOUND(2)-1
C
        DO J=1,JFEC
        READ(5,*) (NCH(J,I),I=1,NBOUND(J))
ENDDO
C
WRITE(6,605) NFRUN,NBRUN,IFEC,IPRI,NINT(1),NINT(2)
605 FORMAT(' FOREGROUND RUN =',I4,'   BACKGROUND RUN =',I4,
1 '   FEC =',I2,'   IPRI =',I2,'    INTERVALS :',I3,I4/)
WRITE(6,606) (NCH(1,N),N=1,NBOUND(1))
606 FORMAT(' CHANNEL BOUND.,   NO FEC :',20I5/27X,20I5/27X,20I5)
WRITE(6,607) (NCH(2,N),N=1,NBOUND(2))
607 FORMAT(' CHANNEL BOUND., WITH FEC :',20I5/27X,20I5/27X,20I5)
C
C-----------------------------------------------------------------------
C
C Read input information from files E633_RUNS., E633_SCAL. & E633_EFFS.
C   ---------- ----------   ----------
C Read BASIC run information for foreground and background runs,
C from file E633_RUNS. (This file is always the same composite file.)
```

```
C
C Read SCALERS information for foreground and background runs,
C from file E633_SCAL. (This file is always the same composite file.)
C
C Read FEC & VDC efficiencies from NOVA analysis for foreground and
C background runs, from file E633_EFFS.
C (This file is always the same composite file.)
C
IF(NBRUN.NE.0) GO TO 7
IF(NBRUN.EQ.0) THEN
NRUN=NFRUN
I=1
ENDIF
GO TO 8
C
7 IF(NFRUN.LT.NBRUN) THEN
NRUN=NFRUN
I=1
ENDIF
C
IF(NBRUN.LT.NFRUN) THEN
NRUN=NBRUN
I=2
ENDIF
C
8 CONTINUE
C
DO K=1,IMAX
C
10      READ(2,*) IRUN,PO,BSASP,THSASP,ITHTGT,IBPT,NTGT ! E633_RUNS.
IF(IRUN.LT.NRUN) GO TO 10
IF(IRUN.NE.NRUN) GO TO 99
C
20      READ(3,*) JRUN ! E633_SCAL.
        READ(3,*) (S(J),J=1,112)
IF(JRUN.LT.NRUN) GO TO 20
IF(JRUN.NE.NRUN) GO TO 99
C
32 READ(4,*) KRUN,LPID1(I),LPID2(I),(MTRY(1,I,J),J=1,6),
1 (FECVDC_A(1,I,J),J=1,3),(EFF_A(1,I,J),J=1,54),
2 (MTRY(2,I,J),J=1,6),(FECVDC_A(2,I,J),J=1,3),
3 (EFF_A(2,I,J),J=1,54) ! E633_EFFS.
C
IF(KRUN.LT.NRUN) GO TO 32
IF(KRUN.NE.NRUN) GO TO 99
C
C Now assign the variables to the appropriate arrays
C    (I=1 <-> FOREGROUND,  I=2 <-> BACKGROUND)
C
C ############################  E633_RUNS.  ############################
MMM(I)=NRUN
PPI(I)=PO
B(I)=BSASP
THETAS(I)=THSASP
THETAT(I)=ITHTGT
IBP(I)=IBPT
NTG(I)=NTGT
C
C ############################  E633_SCAL.  ############################
                BUSY(I)=S(26)               ! LATCH (SASP)
                EVENT(I)=S(29)              ! EVENT (SASP)
                RTRIGS(I)=S(42)             ! TRIGS (HRS), used as monitor
C       POLARIMETER UP
                POLLTU(I)=S(65)             ! POLARIMETER LEFT TOTALS UP
                POLRTU(I)=S(66)             ! POLARIMETER RIGHT TOTALS UP
                POLLAU(I)=S(69)             ! POLARIMETER LEFT ACCIDENTALS UP
```

```
                POLRAU(I)=S(70)             ! POLARIMETER RIGHT ACCIDENTALS UP
C       OTHER SPIN UP
                EVU(I)=S(72)
                SEMU(I)=S(73)
                T6OU(I)=S(75)
                CLU(I)=S(76)
C       POLARIMETER DOWN
                POLLTD(I)=S(77)             ! POLARIMETER LEFT TOTALS DOWN
                POLRTD(I)=S(78)             ! POLARIMETER RIGHT TOTALS DOWN
                POLLAD(I)=S(81)             ! POLARIMETER LEFT ACCIDENTALS DOWN
                POLRAD(I)=S(82)             ! POLARIMETER RIGHT ACCIDENTALS DOWN
C       OTHER SPIN DOWN
                EVD(I)=S(84)
                SEMD(I)=S(85)
                T6OD(I)=S(87)
                CLD(I)=S(88)
C   RATE CALCULATIONS
Tsec(I)=(T6OU(I)+T6OD(I))/60.0 ! Time in sec
                TS=Tsec(I)
FECXO(I)=S(22)/TS
                VDCX1(I)=S(19)/TS
                PADDO(I)=S(1)/TS
                PADD1(I)=S(2)/TS
                PADD2(I)=S(3)/TS
                PADD3(I)=S(4)/TS
                PADD4(I)=S(5)/TS
                RSLO(I)=S(6)/TS
                RSHI(I)=S(7)/TS
                REVENT(I)=S(29)/TS
                RBUSY(I)=S(26)/TS
RRPP=LPID1(I)
RPID1(I)=RRPP/TS
RRPP=LPID2(I)
RPID2(I)=RRPP/TS

C ##########################################################################
C
IF(NBRUN.EQ.0) GO TO 44
IF(K.EQ.1.AND.I.EQ.1) GO TO 41
IF(K.EQ.1.AND.I.EQ.2) GO TO 42
C
41 NRUN=NBRUN
I=2
GO TO 44
42 NRUN=NFRUN
I=1
44 CONTINUE
C
ENDDO ! K-Loop end, all files E633_RUNS, E633_SCAL, E633_EFFS read
C--------------------------------------------------------------------------
WRITE(6,620)
620 FORMAT('O RUN  NTG IBP  P_pi   BSASP   SASP   TGT    HRS HOM ',
1'   BUSY     EVENT    BUSYU   EVENTU    BUSYD   EVENTD ')
DO I=1,IMAX
WRITE(6,621) NNN(I),NTG(I),IBP(I),PPI(I),B(I),THETAS(I),THETAT(I),
1 RTRIGS(I),BUSY(I),EVENT(I),CLU(I),EVU(I),CLD(I),EVD(I)
621 FORMAT(1H ,3I4,F8.2,F7.3,F8.2,F6.1,F11.0,6F9.0)
ENDDO
C
WRITE(6,622)
622 FORMAT('O RUN  T(s)',16X,'XO     X1       PO     P1     P2     ',
1 ' P3     P4        SL      SH     EVENT  BUSY  ',
2 ' LPIDi  LPIDo ')
   DO I=1,IMAX
WRITE(6,623) NNN(I),Tsec(I),FECXO(I),VDCX1(I),PADDO(I),PADD1(I),
1 PADD2(I),PADD3(I),PADD4(I),RSLO(I),RSHI(I),REVENT(I),RBUSY(I),
```

```
 2 RPID1(I),RPID2(I)
 ENDDO
 623 FORMAT(1H ,I4,F7.0,'  RATES : ',F9.0,F7.0,2X,5F7.0,2X,2F8.0,2X,
 1 2F6.0,1X,2F7.0)
 C
 WRITE(6,624)
 624 FORMAT('0   POLLTU    POLRTU    POLLAU    POLRAU      SEMU  ',
 1        '  POLLTD    POLRTD    POLLAD    POLRAD      SEMD  ',
 2        '    T6OU      T6OD ')
 DO I=1,IMAX
 WRITE(6,625) POLLTU(I),POLRTU(I),POLLAU(I),POLRAU(I),SEMU(I),
 1       POLLTD(I),POLRTD(I),POLLAD(I),POLRAD(I),SEMD(I),
 2        T6OU(I),T6OD(I)
 625 FORMAT(1H ,12F10.0)
 ENDDO
 C-------------------------------------------------------------------------
 C
 C Computer live-times and associated errors
 NRUN=NFRUN
 C
 C       Polarization and beam normalization
                 IF(NRUN.LE.191) THEN             ! 500 MeV
                         ANCH2=0.470              ! CH2 analyzing power
                         IF(IBP(1).EQ.3) POLN=111.3       ! Counts/nC
                         IF(IBP(1).EQ.4) POLN=2943.0      ! Counts/nC
                         SEM=6.71                 ! Counts/nC
                 ENDIF
                 IF(NRUN.GE.192) THEN             ! 420 MeV
                         ANCH2=0.434              ! CH2 analyzing power
                         IF(IBP(1).EQ.3) POLN=98.1        ! Counts/nC
                         IF(IBP(1).EQ.4) POLN=2593.0      ! Counts/nC
                         SEM=7.24                 ! Counts/nC
                 ENDIF
                         POLSEM=POLN/SEM
 WRITE(6,630) SEM,POLN,ANCH2,dWSASP
 630 FORMAT('0 CALIBRATION CONSTANTS :    SEM =',F5.2,' Counts/nC',
 1 '     POLARIMETER =',F7.1,' Counts/nC    Ano =',F6.3,
 2 '     dOMEGA =',F7.4,' sr')
 C
         DO I=1,IMAX
         COMP_LIVE(I)=BUSY(I)/EVENT(I)
                 ECO_L(I)=DSQRT(COMP_LIVE(I)*(1.0-COMP_LIVE(I))/EVENT(I))
         UP_LIVE(I)=CLU(I)/EVU(I)
                 EUP_L(I)=DSQRT(UP_LIVE(I)*(1.0-UP_LIVE(I))/EVU(I))
         DN_LIVE(I)=CLD(I)/EVD(I)
                 EDN_L(I)=DSQRT(DN_LIVE(I)*(1.0-DN_LIVE(I))/EVD(I))
 C
 IBPT=IBP(I)
 CALL POL_OFF(NRUN,IBPT,POL_C)
 POL_CORR(I)=POL_C ! POL. OFF correction
 C
             ASYMN_UP(I)=((POLLTU(I)-POLLAU(I))-(POLRTU(I)-POLRAU(I)))/
 1               ((POLLTU(I)-POLLAU(I))+(POLRTU(I)-POLRAU(I)))
             ASYMN_DN(I)=((POLLTD(I)-POLLAD(I))-(POLRTD(I)-POLRAD(I)))/
 1    ((POLLTD(I)-POLLAD(I))+(POLRTD(I)-POLRAD(I)))

 PUP(I)=ASYMN_UP(I)/ANCH2-POL_CORR(I) ! UP polarization, corrected
         PDN(I)=-ASYMN_DN(I)/ANCH2+POL_CORR(I)  ! DOWN polarization, corrected
 C
 C Statistical error in UP polarization
     G1=DSQRT((POLLTU(I)+POLLAU(I))*(POLRTU(I)-POLRAU(I))**2+
 1        (POLRTU(I)+POLRAU(I))*(POLLTU(I)-POLLAU(I))**2)
     EUP(I)=(1.0/ANCH2)*2.0*G1/
 1        (POLLTU(I)-POLLAU(I)+POLRTU(I)-POLRAU(I))**2
 C
 C Statistical error in DN polarization
```

```
      G2=DSQRT((POLLTD(I)+POLLAD(I))*(POLRTD(I)-POLRAD(I))**2+
     1      (POLRTD(I)+POLRAD(I))*(POLLTD(I)-POLLAD(I))**2)
      EDN(I)=(1.0/ANCH2)*2.0*G2/
     1      (POLLTD(I)-POLLAD(I)+POLRTD(I)-POLRAD(I))**2
C
C Polarimeter UP counts and error
POLU(I)=(POLLTU(I)+POLRTU(I)-POLLAU(I)-POLRAU(I))
EPOLU(I)=DSQRT(POLLTU(I)+POLRTU(I)+POLLAU(I)+POLRAU(I))
C
C Polarimeter DN counts and error
POLD(I)=(POLLTD(I)+POLRTD(I)-POLLAD(I)-POLRAD(I))
EPOLD(I)=DSQRT(POLLTD(I)+POLRTD(I)+POLLAD(I)+POLRAD(I))
C
C Proton flux and error. Note that there is a problem with the SEM in
C that it indicates large asymmetries (~10%), when the polarimeter
C indicates no UP/DN asymmetries. In addition, the SEM seems to have
C a 'dark current', noticeable at low beam currents (~0.1 nA). After
C correcting for this effect, we adopt the 'fix' that the SEM now
C gives the correct total proton flux and the polarimeter gives the
C proper UP/DN ratio. Hence,
C
C Various scaler ratios
SEMU_C(I)=0.0366*T60U(I)/60.0 ! SEM 'dark current corr.
SEMD_C(I)=0.0366*T60D(I)/60.0 ! SEM 'dark current corr.
SEM_CORR=(SEMU(I)-SEMU_C(I))+(SEMD(I)-SEMD_C(I))
C
                  POL_RAT(I)=POLU(I)/POLD(I)
                  POL_SEM(I)=((POLU(I)+POLD(I))/(SEM_CORR))/POLSEM
                  SEM_RAT(I)=(SEMU(I)-SEMU_C(I))/(SEMD(I)-SEMD_C(I))
C
                  SEMI=(SEM_CORR/SEM)/(1.602D-10)
                       ESEMI=(2.0/SEM)/(1.602D-10) ! 1 unit error in each
YYY=POLU(I)+POLD(I)
VVV=((EPOLU(I)*POLD(I))**2+(EPOLD(I)*POLU(I))**2)*
1 (SEMI/YYY)**2
                  PROT_UP(I)=SEMI*POLU(I)/(POLU(I)+POLD(I))
EP_UP(I)=DSQRT(VVV+(ESEMI*POLU(I))**2)/YYY
                  PROT_DN(I)=SEMI*POLD(I)/(POLU(I)+POLD(I))
EP_DN(I)=DSQRT(VVV+(ESEMI*POLD(I))**2)/YYY
EP_TO(I)=DSQRT(EP_UP(I)**2+EP_DN(I)**2)
C
                  Tmin(I)=(T60U(I)+T60D(I))/3600.0         ! Total time in min.
C       Average beam currents (nA)
                  CURRENT_UP(I)=(1.602D-10)*PROT_UP(I)/(T60U(I)/60.0)
                  CURRENT_DN(I)=(1.602D-10)*PROT_DN(I)/(T60D(I)/60.0)
                  CURRENT_AV(I)=(CURRENT_UP(I)+CURRENT_DN(I))/2.0
ENDDO
C-------------------------------------------------------------------------
WRITE(6,640)
640 FORMAT('0 CALCULATIONS FROM SCALERS (Including following ',
1 'POLARIMETER and SEM corrections)' )
WRITE(6,6401) POL_CORR(1),SEMU_C(1),SEMD_C(1),CURRENT_AV(1)
6401 FORMAT('        FOREGROUND : POL :',F8.4,'   SEM (UP/DN) :',
1 2F7.1,'     I_AV =',F5.2,' nA')
IF(NBRUN.EQ.0) GO TO 6405
WRITE(6,6402) POL_CORR(2),SEMU_C(2),SEMD_C(2),CURRENT_AV(2)
6402 FORMAT('        BACKGROUND : POL :',F8.4,'   SEM (UP/DN) :',
1 2F7.1,'     I_AV =',F5.2,' nA')
C
6405 CONTINUE
WRITE(6,641)
641 FORMAT('0    COMP_LIVE          UP_LIVE          DN_LIVE     ',
1 '       POL_UP            POL_DN ')
C
DO I=1,IMAX
WRITE(6,642) COMP_LIVE(I),ECO_L(I),UP_LIVE(I),EUP_L(I),
```

```
1 DN_LIVE(I),EDN_L(I),PUP(I),EUP(I),PDN(I),EDN(I)
642 FORMAT(1H ,F7.4,' (',F6.4,')',2X,F7.4,' (',F6.4,')',2X,
1 F7.4,' (',F6.4,')',2X,F7.4,' (',F6.4,')',2X,
2 F7.4,' (',F6.4,')')
ENDDO
C
WRITE(6,646)
646 FORMAT('0    POLARIMETER_UP     POLARIMETER_DN    ',
1 '      SEM PROTONS_UP             SEM PROTONS_DN ')
DO I=1,IMAX
WRITE(6,648) POLU(I),EPOLU(I),POLD(I),EPOLD(I),
1 PROT_UP(I),EP_UP(I),PROT_DN(I),EP_DN(I)
648 FORMAT(1H ,F11.0,' (',F5.0,')',F11.0,' (',F5.0,')',
1 E14.4,' (',E10.4,')',E14.4,' (',E10.4,')')
ENDDO
C
C-------------------------------------------------------------------------
DO LZ=1,JFEC
WRITE(6,650)
DO I=1,IMAX
DO J=1,6
NTRY(I,J)=NTRY(LZ,I,J)
ENDDO
DO J=1,3
FECVDC(I,J)=FECVDC_A(LZ,I,J)
ENDDO
DO J=1,54
EFF(I,J)=EFF_A(LZ,I,J)
ENDDO
ENDDO
C
CALL FEC_VDC(LZ,IMAX,IFEC,IPRI)
C FEC(I,M) ! FEC efficiency
C EFEC(I,M) ! Error in FEC efficiency
C VDC(I,M) ! VDC efficiency
C EVDC(I,M) ! Error in VDC efficiency
C FV(I,J,M) ! Composite FEC&VDC efficiency
C EFV(I,J,M) ! Error in above ...
C   I=1,2 for Foreground and background, respectively
C   J=1,2 for No FEC and With FEC analysis, respectively
C   M=1,2,3 for ALL, UP and DN, respectively
C
ENDDO
WRITE(6,650)
650 FORMAT('0**********************************************************',
1 '**********************************************************',
2 '******************'/)
C
C-------------------------------------------------------------------------
C
WRITE(6,654)
654 FORMAT(' COMPOSITE FEC AND VDC EFFICIENCIES TRANSFERRED FROM',
1 ' SUBROUTINE FEC_VDC TO MAIN ROUTINE (FOR SIGMA CALC.)'/)
C
WRITE(6,655) FV(1,1,1),EFV(1,1,1),FV(1,1,2),EFV(1,1,2),
1 FV(1,1,3),EFV(1,1,3),FV(1,2,1),EFV(1,2,1),
2 FV(1,2,2),EFV(1,2,2),FV(1,2,3),EFV(1,2,3)
655 FORMAT(' FOREGROUND : NO FEC ',
1 F8.4,' (',F6.4,')',F8.4,' (',F6.4,')',F8.4,' (',F6.4,')',
2 ',  FEC ',
3 F8.4,' (',F6.4,')',F8.4,' (',F6.4,')',F8.4,' (',F6.4,')')
C
IF(NBRUN.EQ.0) GO TO 47
WRITE(6,657) FV(2,1,1),EFV(2,1,1),FV(2,1,2),EFV(2,1,2),
1 FV(2,1,3),EFV(2,1,3),FV(2,2,1),EFV(2,2,1),
2 FV(2,2,2),EFV(2,2,2),FV(2,2,3),EFV(2,2,3)
```

```
657 FORMAT(' BACKGROUND : NO FEC ',
1 F8.4,' (',F6.4,')',F8.4,' (',F6.4,')',F8.4,' (',F6.4,')',
2 ',  FEC ',
3 F8.4,' (',F6.4,')',F8.4,' (',F6.4,')',F8.4,' (',F6.4,')')
47 CONTINUE
C
C-----------------------------------------------------------------------
C
C READ 12 (NO FEC) or 24 (WITH FEC) NX channel spectra created by
C the NOVA SWRITE command.
C
NX=900
DO I=1,IMAX
DO J=1,JFEC
IF(I.EQ.1.AND.J.EQ.1) KK=10
IF(I.EQ.1.AND.J.EQ.2) KK=16
IF(I.EQ.2.AND.J.EQ.1) KK=22
IF(I.EQ.2.AND.J.EQ.2) KK=28
DO K=1,6
KK=KK+1
C
C Read 1D spectrum
DO N=1,2 !Dummy READS
READ(KK,*) IJUNK
ENDDO
READ(KK,*) QJUNK ! Dummy READ
C
LL=NX+2
READ(KK,*) (UF(L),L=1,LL)
DO L=1,NX !
A(I,J,K,L)=UF(L+1) ! Ignore underflow and overflow
ENDDO !
ENDDO
ENDDO
ENDDO
C-----------------------------------------------------------------------
C Output spectra for PLOTDATA. FOREGROUND spectra 1-6 for NO FEC,
C followed by FOREGROUND spectra 1-6 WITH FEC.
DO N=1,NX
WRITE(9,910) N,A(1,1,1,N),A(1,1,2,N),A(1,1,3,N),A(1,1,4,N),
1 A(1,1,5,N),A(1,1,6,N),A(1,2,1,N),A(1,2,2,N),
2 A(1,2,3,N),A(1,2,4,N),A(1,2,5,N),A(1,2,6,N)
ENDDO
910 FORMAT(1H ,I5,2X,6F8.0,2X,6F8.0)
C-----------------------------------------------------------------------
C       Output spectra for PLOTDATA. BACKGROUND spectra 1-6 for NO FEC,
C       followed by BACKGROUND spectra 1-6 WITH FEC.
IF(NBRUN.EQ.0) GO TO 48
        DO N=1,NX
WRITE(9,910) N,A(2,1,1,N),A(2,1,2,N),A(2,1,3,N),A(2,1,4,N),
1 A(2,1,5,N),A(2,1,6,N),A(2,2,1,N),A(2,2,2,N),
2 A(2,2,3,N),A(2,2,4,N),A(2,2,5,N),A(2,2,6,N)
        ENDDO
48 CONTINUE
C-----------------------------------------------------------------------
C Factors for cross section calculations
                TARG_N=4.111*(1.0D+22)/DCOS(THETAT(1)/RAD)
                RRR=dWSASP*TARG_N*(1.0D-30)
DO I=1,IMAX
RTO(I,1)=RRR*COMP_LIVE(I)*FV(I,1,1)*(PROT_UP(I)+PROT_DN(I))
RTO(I,2)=RRR*COMP_LIVE(I)*FV(I,2,1)*(PROT_UP(I)+PROT_DN(I))
  RUP(I,1)=RRR*UP_LIVE(I)*FV(I,1,2)*PROT_UP(I) ! NO FEC
  RUP(I,2)=RRR*UP_LIVE(I)*FV(I,2,2)*PROT_UP(I) ! WITH FEC
  RDN(I,1)=RRR*DN_LIVE(I)*FV(I,1,3)*PROT_DN(I) ! NO FEC
  RDN(I,2)=RRR*DN_LIVE(I)*FV(I,2,3)*PROT_DN(I) ! WITH FEC
ENDDO
```

```
C-----------------------------------------------------------------------
WRITE(6,662) RTO(1,1),RUP(1,1),RDN(1,1)
WRITE(6,663) RTO(1,2),RUP(1,2),RDN(1,2)
662 FORMAT('0FACTORS FOR FOREGROUND CROSS SECTION CALCULATION,',
1 ' TOTAL, UP, DN    (NO FEC)  : ',3E13.4)
663 FORMAT(' FACTORS FOR FOREGROUND CROSS SECTION CALCULATION,',
1 ' TOTAL, UP, DN  (WITH FEC)  : ',3E13.4)
C
WRITE(9,920) RTO(1,1),RUP(1,1),RDN(1,1),
1      RTO(1,2),RUP(1,2),RDN(1,2)
920 FORMAT(1H ,6F13.3)
C
IF(NBRUN.EQ.0) GO TO 49
WRITE(9,920) RTO(2,1),RUP(2,1),RDN(2,1),
1      RTO(2,2),RUP(2,2),RDN(2,2)
C
WRITE(6,664) RTO(2,1),RUP(2,1),RDN(2,1)
WRITE(6,665) RTO(2,2),RUP(2,2),RDN(2,2)
664 FORMAT('0FACTORS FOR BACKGROUND CROSS SECTION CALCULATION,',
1 ' TOTAL, UP, DN    (NO FEC)  : ',3E13.4)
665 FORMAT(' FACTORS FOR BACKGROUND CROSS SECTION CALCULATION,',
1 ' TOTAL, UP, DN  (WITH FEC)  : ',3E13.4)
49 CONTINUE
C-----------------------------------------------------------------------
C
C SASP Spectrometer momentum intervals and boundaries for binning data
PSC=49.9698*B(1) ! SASP central momentum (Foreground Run)
C Calibration scale for SWRITE Spectra
FNX=NX
CAL=FNX/(DEL_HI-DEL_LO) ! Channels/unit SDEL
C DEL Calibration is thus : DEL = DEL_LO + N/CAL, where N = ch. No.
C NCH(J,I) is the lower-end channel of interval I,
C NCH(J,I+1)-1 the upper-end channel of interval I,
C
C Calculate DEL and MOMENTUM at the bin boundaries
C DEL1 and P1 are the SDEL and Momentum values at the lower edge of
C channel NCH(J,N)
C DEL2 and P2 are the SDEL and Momentum values at the upper edge of
C channel NCH(J,N+1)-1
C
DO J=1,JFEC
DO N=1,NINT(J)
X1=NCH(J,N)
DEL1(J,N)=DEL_LO+X1/CAL
P1(J,N)=PSC*(1.0+DEL1(J,N)/100.0)
X2=NCH(J,N+1)
DEL2(J,N)=DEL_LO+X2/CAL
P2(J,N)=PSC*(1.0+DEL2(J,N)/100.0)
P_INT(J,N)=P2(J,N)-P1(J,N) ! Momentum interval
P_AV(J,N)=(P1(J,N)+P2(J,N))/2.0 ! Momentum at center
ENDDO
ENDDO
C-----------------------------------------------------------------------
C Zero arrays
DO I=1,2
DO J=1,2
DO K=1,6
DO N=1,NINT(J)
SUM(I,J,K,N)=0.0
Y(I,J,K,N)=0.0
EY(I,J,K,N)=0.0
ENDDO
ENDDO
ENDDO
ENDDO
C-----------------------------------------------------------------------
```

```
C Bin the data for the various spectra
DO I=1,IMAX
DO J=1,JFEC
DO K=1,6
DO M=1,MINT(J)
LLO=MCH(J,M)
LHI=MCH(J,M+1)-1
DO L=LLO,LHI
SUM(I,J,K,M)=SUM(I,J,K,M)+A(I,J,K,L)
ENDDO
ENDDO
ENDDO
ENDDO
ENDDO
C-------------------------------------------------------------------------
C Print the binned data
        DO J=1,JFEC
        IF(J.EQ.1) WRITE(6,666)
        IF(J.EQ.2) WRITE(6,667)
666     FORMAT('OBINNED DATA (NO FEC), SPECTRA 1-6  ',
1 ' ---------------- FOREGROUND ---------------- ',
2 ' ---------------- BACKGROUND ---------------- ')
667     FORMAT('OBINNED DATA (WITH FEC), SPECTRA 1-6',
1 ' ---------------- FOREGROUND ---------------- ',
2 ' ---------------- BACKGROUND ---------------- ')
C
        WRITE(6,668)
668     FORMAT('    M  MLO  MHI    DEL_LO  DEL_HI   ',
1 '     1       2       3       4       5       6  ',
2 '     1       2       3       4       5       6 ')
C
        DO M=1,MINT(J)
        M=1+MINT(J)-M
                LLO=MCH(J,M)
                LHI=MCH(J,M+1)-1
        WRITE(6,669) M,LLO,LHI,DEL1(J,M),DEL2(J,M),
1 (SUM(1,J,K,M),K=1,6),(SUM(2,J,K,M),K=1,6)
669     FORMAT(1H ,I4,2I5,2X,2F8.3,2X,12F8.0)
        ENDDO
        ENDDO
C-------------------------------------------------------------------------
C Calculate cross sections (Y) for FOREGROUND and BACKGROUND spectra
C and their associated statistical errors (EY)
DO I=1,IMAX
DO J=1,JFEC
C
C SUM of fractional errors squared, in proton flux, livetime, FEC&VDC
C
EE_TO(I,J)=EP_TO(I)**2/(PROT_UP(I)+PROT_DN(I))**2 +
1    (ECO_L(I)/COMP_LIVE(I))**2 + (EFV(I,J,1)/FV(I,J,1))**2
C
EE_UP(I,J)=EP_UP(I)**2/PROT_UP(I)**2 + (EUP_L(I)/UP_LIVE(I))**2
1 + (EFV(I,J,2)/FV(I,J,2))**2
C
EE_DN(I,J)=EP_DN(I)**2/PROT_DN(I)**2 + (EDN_L(I)/DN_LIVE(I))**2
1 + (EFV(I,J,3)/FV(I,J,3))**2
C
DO M=1,MINT(J)
Y(I,J,4,M)=SUM(I,J,4,M)/(RTO(I,J)*P_INT(J,M))
Y(I,J,5,M)=SUM(I,J,5,M)/(RUP(I,J)*P_INT(J,M))
Y(I,J,6,M)=SUM(I,J,6,M)/(RDN(I,J)*P_INT(J,M))
IF(SUM(I,J,1,M).EQ.0.0) GO TO 53
EY(I,J,4,M)=Y(I,J,4,M)*DSQRT(1.0/SUM(I,J,1,M)+EE_TO(I,J))
53 IF(SUM(I,J,2,M).EQ.0.0) GO TO 54
EY(I,J,5,M)=Y(I,J,5,M)*DSQRT(1.0/SUM(I,J,2,M)+EE_UP(I,J))
54 IF(SUM(I,J,3,M).EQ.0.0) GO TO 55
```

```
EY(I,J,6,M)=Y(I,J,6,M)*DSQRT(1.0/SUM(I,J,3,M)+EE_DM(I,J))
55 CONTINUE
ENDDO
ENDDO
ENDDO
C-------------------------------------------------------------------------
DO J=1,JFEC
IF(J.EQ.1) WRITE(6,670)
IF(J.EQ.2) WRITE(6,672)
670 FORMAT('OCROSS SECTIONS (NO FEC)            ',
1 ' ---------------- FOREGROUND ---------------- ',
2 ' ---------------- BACKGROUND ---------------- ')
672 FORMAT('OCROSS SECTIONS (WITH FEC)          ',
1 ' ---------------- FOREGROUND ---------------- ',
2 ' ---------------- BACKGROUND ---------------- ')
C
WRITE(6,674)
674  FORMAT('    M  MLO  MHI    DEL_LO  DEL_HI   ',
1 ' SIG_TO dSIG_TO  SIG_UP dSIG_UP  SIG_DN dSIG_DN ',
2 ' SIG_TO dSIG_TO  SIG_UP dSIG_UP  SIG_DN dSIG_DN ')
C
DO M=1,MINT(J)
M=1+MINT(J)-M
LLO=MCH(J,M)
LHI=MCH(J,M+1)-1
WRITE(6,676) M,LLO,LHI,DEL1(J,M),DEL2(J,M),
1 Y(1,J,4,M),EY(1,J,4,M),Y(1,J,5,M),EY(1,J,5,M),
2 Y(1,J,6,M),EY(1,J,6,M),Y(2,J,4,M),EY(2,J,4,M),
3 Y(2,J,5,M),EY(2,J,5,M),Y(2,J,6,M),EY(2,J,6,M)
676 FORMAT(1H ,I4,2I5,2X,2F8.3,2X,6(F9.4,F7.4))
ENDDO
ENDDO
C-------------------------------------------------------------------------
C Calculate the background-subtracted cross sections and errors
DO J=1,JFEC
DO M=1,MINT(J)
SIGO(J,M)=Y(1,J,4,M)-Y(2,J,4,M)
SIGU(J,M)=Y(1,J,5,M)-Y(2,J,5,M)
SIGD(J,M)=Y(1,J,6,M)-Y(2,J,6,M)
dSIGO(J,M)=DSQRT(EY(1,J,4,M)**2+EY(2,J,4,M)**2)
dSIGU(J,M)=DSQRT(EY(1,J,5,M)**2+EY(2,J,5,M)**2)
dSIGD(J,M)=DSQRT(EY(1,J,6,M)**2+EY(2,J,6,M)**2)
C
C Spin averaged cross section and error, SIGA and dSIGA
IF(PDM(1).LT.0.1.OR.PUP(1).LT.0.1) GO TO 60
C
SIGA(J,M)=(PDM(1)*SIGU(J,M)+PUP(1)*SIGD(J,M))/
1         (PUP(1)+PDM(1))
AAA=((EDM(1)*PUP(1))**2+(EUP(1)*PDM(1))**2)*
1 (SIGU(J,M)-SIGD(J,M))**2/(PUP(1)+PDM(1))**2
BBB=(dSIGU(J,M)*PDM(1))**2+(dSIGD(J,M)*PUP(1))**2
dSIGA(J,M)=DSQRT(AAA+BBB)/(PUP(1)+PDM(1))
GO TO 62
60 SIGA(J,M)=(SIGU(J,M)+SIGD(J,M))/2.0
dSIGA(J,M)=DSQRT(dSIGU(J,M)**2+dSIGD(J,M)**2)/2.0
62 CONTINUE
C
C Background spin-averaged cross section
IF(PDM(2).LT.0.1.OR.PUP(2).LT.0.1) GO TO 64
C
SIG_BKD(J,M)=0.0
IF(MBRUN.EQ.0) GO TO 68
SIG_BKD(J,M)=(PDM(2)*Y(2,J,5,M)+PUP(2)*Y(2,J,6,M))/
1 (PUP(2)+PDM(2))
64 CONTINUE
SIG_BKD(J,M)=(Y(2,J,5,M)+Y(2,J,6,M))/2.0
```

```
68 CONTINUE
C
C Analyzing power and error, ANO and dANO
ANO(J,M)=0.0
     dANO(J,M)=0.0
IF(PDN(1).LT.0.1.OR.PUP(1).LT.0.1) GO TO 72
DDD=(PDN(1)*SIGU(J,M)+PUP(1)*SIGD(J,M))
IF(DDD.EQ.0.0) GO TO 72
ANO(J,M)=-(SIGU(J,M)-SIGD(J,M))/DDD
CCC=(SIGU(J,M)-SIGD(J,M))**2*((EDN(1)*SIGU(J,M))**2 +
1 (EUP(1)*SIGD(J,M))**2) + (PUP(1)+PDN(1))**2*
2 ((dSIGU(J,M)*SIGD(J,M))**2 + (dSIGD(J,M)*SIGU(J,M))**2)
dANO(J,M)=DSQRT(CCC)/DDD**2
72 CONTINUE
ENDDO
ENDDO
C-----------------------------------------------------------------------
WRITE(7,710) NFRUN,NBRUN,NINT(1),NINT(2),B(1),THETAS(1),
1 THETAT(1),IBP(1)
710     FORMAT(' FORGD RUN =',I4,'  BCKGD RUN =',I4,
1 '  INTERVALS =',I3,I4'  BSASP =',F6.3,'  THETA_SASP =',F6.2,
2 '  THETA_TGT =',F5.1,'  IBP_TGT =',I2,'   NO FEC')
        WRITE(7,684)
C
WRITE(8,810) NFRUN,NBRUN,NINT(1),NINT(2),B(1),THETAS(1),
1 THETAT(1),IBP(1)
810     FORMAT(' FORGD RUN =',I4,'  BCKGD RUN =',I4,
1 '  INTERVALS =',I3,I4'  BSASP =',F6.3,'  THETA_SASP =',F6.2,
2 '  THETA_TGT =',F5.1,'  IBP_TGT =',I2,'   WITH FEC')
        WRITE(8,684)
C
        DO J=1,JFEC
        IF(J.EQ.1) WRITE(6,680)
        IF(J.EQ.2) WRITE(6,682)
680     FORMAT('0 FINAL CROSS SECTIONS (NO FEC) ')
682     FORMAT('0 FINAL CROSS SECTIONS (WITH FEC) ')
C
        WRITE(6,684)

684     FORMAT('    N   P_LO    P_HI   P_INT   P_AV      SIGO    dSIGO',
1 '   SIGU    dSIGU   SIGD    dSIGD   SIGA    dSIGA ',
2 '    ANO    dANO    SIG_BKD')
C
        DO N=1,NINT(J)
        M=1+NINT(J)-N
        WRITE(6,686) M,P1(J,M),P2(J,M),P_INT(J,M),P_AV(J,M),SIGO(J,M),
1 dSIGO(J,M),SIGU(J,M),dSIGU(J,M),SIGD(J,M),dSIGD(J,M),
2 SIGA(J,M),dSIGA(J,M),ANO(J,M),dANO(J,M),SIG_BKD(J,M)
686 FORMAT(1H ,I4,2F8.2,F7.3,F8.2,2X,4(F9.4,F7.4),F10.4,F8.4,F10.4)
C
IF(J.EQ.1) WRITE(7,686) M,P1(J,M),P2(J,M),P_INT(J,M),P_AV(J,M),
1 SIGO(J,M),dSIGO(J,M),SIGU(J,M),dSIGU(J,M),SIGD(J,M),
2 dSIGD(J,M),SIGA(J,M),dSIGA(J,M),ANO(J,M),dANO(J,M),
3 SIG_BKD(J,M)
C
IF(J.EQ.2) WRITE(8,686) M,P1(J,M),P2(J,M),P_INT(J,M),P_AV(J,M),
1 SIGO(J,M),dSIGO(J,M),SIGU(J,M),dSIGU(J,M),SIGD(J,M),
2 dSIGD(J,M),SIGA(J,M),dSIGA(J,M),ANO(J,M),dANO(J,M),
3 SIG_BKD(J,M)
C
        ENDDO
        ENDDO
C-----------------------------------------------------------------------
99 CONTINUE
END
C-----------------------------------------------------------------------
```

Appendix D

The MUON_MC.FOR program

```
C ------------------------------------------------------------------------
C
C Program MMUON_MC.FOR, a Monte carlo calculation of the SASP spectrometer
C focal plane pion spectrum contamination from muons generated in the
C target area. This problem can be severe if there is an intense flux
C of higher energy pions (that lead to lower energy decay muons) at the
C target, while the SASP is set to detect lower energy pions. A case in
C point occurs in the study of the pp->pnpi+ reaction. The intense pion
C peak from pp->dpi+ gives rise to muons that, in all respects, look
C like the lower energy pions that are to be measured.
C W.R. Falk, March 19, 1997, Revised April 14, 1997 to use a revised
C Subroutine MPMPI.FOR.
C
C LINK : MMUON_MC+XSECT+MPMPI+SPPPID+BUGGPPI+OBUGGPPI
C
      IMPLICIT REAL*8(A-H,O-Z)
C
DIMENSION SP_THO(100),SP_TH1(100),SP_PHO(100),SP_PH1(100),
1   SP_XIO(100),SP_XI1(100),SP_YIO(100),SP_YI1(100),
2   SP_XOO(100),SP_XO1(100),SP_YOO(100),SP_YO1(100),
3   SP_ALLO(100),SP_ALL1(100),SP_ALLU1(100),SP_ALLD1(100),
4 SUM(14),D_MUTH(61)
C
READ(5,*) Tp,THET,THO,XPL,ZFEC,DPPI,MTH,MPH,MDE,MMU,IPRI,XMULT,
1 PIL,PIH,PMOO,CUT_TH,CUT_PH,CUT_XI,CUT_YI,CUT_XO,CUT_YO
C Tp : Incident beam energy
C THET : SASP angle wrt to beam direction (deg)
C THO : The half-cone angle wrt SASP direction, within which pion
C trajectories will be analyzed for muon decay (deg).
C XPL : The maximum distance from the target for which pion
C decay is considered (cm).
C ZFEC : Spectrometer entrance screen at "FEC distance (cm).
C Distance is not critical, but must have ZFEC>XPL.
C DPPI : Integration step in pion momentum
C MTH : Number of steps in Theta for integ. over pion direction
C MPH : Number of steps in Phi for integ. over pion direction
C MDE : Number of iterations on pion decay point
C MMU : Number of iterations over muon decay angles
C PIL, PIH : The lower and higher momentum limits of the input
C pion spectrum
C PMOO : Lowest output muon momentum value (multiple of 3)
C IPRI : Print control; details of every IPRI'th event written
C XMULT : Cross section multiplying factor for the Wilkin-type
C calc. of XS. Also for routing in XSECT when XMULT<0
C CUT_TH, CUT_PH, CUT_XI, CUT_YI, CUT_XO, CUT_YO : the muon
C trajectory cuts in the usual TRANSPORT conventions.
C
```

```
WRITE(6,610) Tp,THET,THO,XPL,ZFEC,DPPI,NTH,NPH,NDE,NMU,IPRI,
1 XMULT,PIL,PIH,PHOO,CUT_TH,CUT_PH,CUT_XI,CUT_YI,CUT_XO,CUT_YO
610  FORMAT(' Tp, THET, THO, XPL, ZFEC :',5F7.1/
1 ' DPPI, NTH, NPH, NDE, NMU, IPRI, XMULT :',F6.1,4I5,I7,F8.3/
2 ' PIL, PIH, PHOO, CUT-TH, CUT-PH, CUT-XI, CUT-YI, CUT-XO, ',
3 'CUT-YO :',3F7.1,4X,2F7.1,2X,2F5.1,2X,2F5.1)
C
PI=3.14159
RAD=180.0/PI
        TAU_CO=780.4            ! Pion decay length (cm)
        Wpi=139.568             ! Pion mass
Wu=105.658 ! Muon mass
        EUO=109.777             ! Muon decay energy in pion rest frame, MeV
        PUO=29.7905             ! Muon decay momentum in pion rest frame, MeV/c
dW=0.013 ! SASP solid angle
C
JKL=1
        CALL PWPI(JKL,Tp,TH_SCATT,P3M,P3D,PPI,An1,SIGpp,An2,SIGL)
C
DO I=1,100
SP_THO(I)=0.0
SP_TH1(I)=0.0
SP_PHO(I)=0.0
SP_PH1(I)=0.0
SP_XIO(I)=0.0
SP_XI1(I)=0.0
SP_YIO(I)=0.0
SP_YI1(I)=0.0
SP_XOO(I)=0.0
SP_XO1(I)=0.0
SP_YOO(I)=0.0
SP_YO1(I)=0.0
SP_ALLO(I)=0.0
SP_ALL1(I)=0.0
SP_ALLU1(I)=0.0
SP_ALLD1(I)=0.0
ENDDO
C
DO I=1,61
D_MUTH(I)=0.0
ENDDO
DMAX=0.0
C
C       Define a coordinate system (XYZ) with the Z axis in the direction
C of the SASP spectrometer, the Y axis perpendicular to the scattering
C plane (Up), and the X axis such that a RH coordinate system results.
C Note that the relationships to TRANSPORT are : X=YT, Y=-XT, Z=ZT
C
RTHET=THET/RAD
Uxb=DSIN(RTHET) ! Components of unit       |
Uzb=DCOS(RTHET) ! vector in beam direction |
RTHO=THO/RAD
FNTH=NTH
FNPH=NPH
FNDE=NDE
FNMU=NMU
FDEMU=FNDE*FNMU
FNPI=(PIH-PIL)/DPPI+1.0
NPI=FNPI ! The number of steps in momentum integ.
NEV=0 ! Event counter
WRITE(6,620) dW,Uxb,Uzb,FDEMU,NPI
620 FORMAT(' dW, Uxb, Uzb, FDEMU, NPI : ',F7.4,1X,2F7.3,F6.0,I5/)
C
C Initialize RANDOM, the random number generator
R=2.0
CALL RANDOM(R)
```

```
C
C   1. Generate the pion trajectory at the target
C Carry out a discrete integration over the solid angle of the half-cone.
C The angles are the spherical coordinates in the (XYZ) frame.
C
C
NPRIN=0
DTH=RTHO/FNTH
        DPH=2.0*PI/FNPH
DTHDPH=DTH*DPH
C
TH_P=0.0
DO II=1,NTH ! Integrate over THETA   II - Loop
TH_P=TH_P+DTH
dOMEGA=DSIN(TH_P)*DTHDPH
        PH_P=0.0
        DO JJ=1,NPH             ! Integrate over PHI              JJ - Loop
                PH_P=PH_P+DPH
C
C   2. Calculate the pion scattering angle (wrt beam direction), all
C calculations referred to the (XYZ) frame.
C
Uxp=DSIN(TH_P)*DCOS(PH_P) ! Components of unit      |
Uyp=DSIN(TH_P)*DSIN(PH_P) ! vector in the direction |
Uzp=DCOS(TH_P)          ! of the pion trajectory  |
UU=Uxb*Uxp+Uzb*Uzp    ! Scaler product of unit vectors
TH_SCATT=DACOS(UU)    ! Scattering angle
C
C   3.  Define the decay frame (X'Y'Z') with the Z' axis along the pion
C       momentum, the X' axis in the XZ plane, and the Y' axis such that
C       a RH coordinate system is formed. The transformation matrix from
C       this frame to the (XYZ) frame for any vector V is:
C         Vx   |i.i'  i.j'  i.k'| Vx'   |V11  V12  Uxp | Vx'
C         Vy = |j.i'  j.j'  j.k'| Vy' = | 0   V22  Uyp | Vy'
C         Vz   |k.i'  k.j'  k.k'| Vz'   |V31  V32  Uzp | Vz'
C
                DDD=DSQRT(Uxp**2+Uzp**2)
                V11=Uzp/DDD
                V31=-Uxp/DDD
                V12=Uxp*Uyp/DDD
                V22=(Uzp**2-Uyp**2)/DDD
                V32=-Uyp*Uzp/DDD
C
C Calculate various parameters of the pp->dpi+ and pp->pnpi+ reactions
JKL=2
        CALL PNPI(JKL,Tp,TH_SCATT,P3N,P3D,PPI,An1,SIGpp,An2,SIGL)
C
C   4. Integrate over the pion momentum  of the muon-producing pion spectra
C at angle TH_SCATT.
C
PPI=PIL-DPPI
DO KK=1,NPI !                   KK - Loop
PPI=PPI+DPPI
C
C   5.  Define the appropriate reaction for the pion cross section calculation
C
XS=0.0
Ano=0.0
IF(XMULT.LT.0.0) GO TO 33 ! Use Routine XSECT
IF(PPI.LE.P3N) GO TO 30 ! Use Wilkin-type  calc. for pp->pnpi+
        DPP=DPPI/2.0 ! Use Falk parameterization for pp->dpi+
        DP=DABS(PPI-P3D)
        IF(DP.LT.DPP) THEN
Ano=An1
XS=SIGpp/DPPI
ENDIF
```

```
C       Since XS is multiplied by DPPI in MAIN, we must divide by DPPI for
C       the pp->pdi+ reaction. But NOT for pp->pnpi+. NOTE!!!!!!!
GO TO 35
C
30 JKL=3
        CALL PNPI(JKL,Tp,TH_SCATT,P3M,P3D,PPI,An1,SIGpp,An2,SIGL)
Ano=An2
XS=SIGL*XMULT
GO TO 35
33 CALL XSECT(XMULT,Tp,TH_SCATT,PPI,DPPI,XS)
C
35 IF(XS.EQ.0.0) GO TO 80
C
XSDP=XS*DPPI ! Cross section in the interval DPPI
EPI=DSQRT(PPI**2+Wpi**2) ! Pion energy
BETA=PPI/EPI ! Beta of pion
GAM=1.0/DSQRT(1.0-BETA**2) ! Gamma of pion
C
C   6.  Select the distance from the target at which the pion decays. The
C decay probability along the length XPL is essentially constant.
C
QQ=Wpi*XPL/(TAU_CO*PPI)
DPROB=1.0-DEXP(-QQ) ! Decay probability from 0 to XPL
C
COUNTS=XS*DPPI*dOMEGA*DPROB/(FDEMU*dW)
C
DO LL=1,NDE !                   LL - Loop
40 CALL RANDOM(R)
XLPI=XPL*R ! The decay distance from target
C
C   7.  The point at which the pion decays in the (X,Y,Z) frame is
C
Xx=XLPI*Uxp
Yy=XLPI*Uyp
Zz=XLPI*Uzp
C
C   8.  Select the decay angles of the muon in the rest frame of the pion.
C The decay in this frame is isotropic, since the pion has spin 0-.
C
DO MM=1,NMU !                   MM - Loop
NEV=NEV+1 ! Event counter
NPRIN=NPRIN+1
        CALL RANDOM(R)
                U_PH=2.0*PI*R   ! Uniform phi dist'n bewteen 0 and 2*PI rad.
50      CALL RANDOM(R)
                U_TH=PI*R   ! Uniform theta dist'n bewteen 0 and PI rad.
        CALL RANDOM(R)
                YY=DSIN(U_TH)       ! Weight according to SIN(U_TH)
                IF(R.GT.YY) GO TO 50
BB=U_TH*RAD/3.0
IBB=BB
D_MUTH(IBB)=D_MUTH(IBB)+1.0 ! Theta dist'n of muons
IF(D_MUTH(IBB).GT.DMAX) DMAX=D_MUTH(IBB)
C
C   9.  Calculate the trajectory of the muon.
C First calculate the components of the muon momentum in the pion
C rest frame, with axes as defined by the (X'Y'Z') frame
Pxxp=PUO*DSIN(U_TH)*DCOS(U_PH)
Pyyp=PUO*DSIN(U_TH)*DSIN(U_PH)
Pzzp=PUO*DCOS(U_TH)
C Now calculate the components in the lab (X'Y'Z') frame
Pxx=Pxxp
Pyy=Pyyp
Pzz=GAM*(Pzzp+BETA*EUO)
Pmup=DSQRT(Pxx**2+Pyy**2+Pzz**2)
C Now use the transformation matrix to calculate the muon momentum in
```

```
C the (X,Y,Z) frame
Px=V11*Pxx+V12*Pyy+Uxp*Pzz
Py=        V22*Pyy+Uyp*Pzz
Pz=V31*Pxx+V32*Pyy+Uzp*Pzz
Pmu=DSQRT(Px**2+Py**2+Pz**2)
Umx=Px/Pmu ! Unit vector   |
Umy=Py/Pmu ! components of |
Umz=Pz/Pmu ! the muon      |
C
C  10. The moun trajectory in the (X,Y,Z) frame is now defined by the above
C momentum components and the point where the pion decays (Xx,Yy,Zz).
C A point on the trajectory line is given by the parametric eq's.
C (X-Ix)/Umx = (Y-Yy)/Umy = (Z-Zz)/Umz,
C or X=Ix+(Umx/Umz)*(Z-Zz), and Y=Yy+(Umy/Umz)*(Z-Zz),
C Evaluate X and Y at the target (Z=0) and at TFEC position (Z=ZFEC)
XT=Ix+(Umx/Umz)*(-Zz)
XFEC=Ix+(Umx/Umz)*(ZFEC-Zz)
YT=Yy+(Umy/Umz)*(-Zz)
YFEC=Yy+(Umy/Umz)*(ZFEC-Zz)
C
C  11. Bin the data in intervals of 3 MeV/c per channel.
C Channel 1 covers the interval from PMOO-1.5 to PMOO+1.5 MeV/c, etc.
FPMU=(Pmu-PMOO)/3.0+1.5
MCH=FPMU ! Channel number
IF(MCH.LT.1.OR.MCH.GT.86) GO TO 70
COUN=COUNTS/3.0 ! Counts per MeV/c interval
COUN_UP=COUN*(1.0+Ano)  ! Counts UP per MeV/c interval
COUN_DN=COUN*(1.0-Ano)  ! Counts DN per MeV/c interval
C
C  12. Apply the cuts
ITH=0
IPH=0
IXI=0
IYI=0
IXO=0
IYO=0
THmu=1000.0*DABS(Umy)
IF(THmu.LE.CUT_TH) ITH=1
PHmu=1000.0*DABS(Umx)
IF(PHmu.LE.CUT_PH) IPH=1
IF(DABS(YT).LE.CUT_XI) IXI=1
IF(DABS(XT).LE.CUT_YI) IYI=1
IF(DABS(YFEC).LE.CUT_XO) IXO=1
IF(DABS(XFEC).LE.CUT_YO) IYO=1
C
C Increment spectra
IF(ITH.EQ.0) SP_TH0(MCH)=SP_TH0(MCH)+COUN
IF(ITH.EQ.1) SP_TH1(MCH)=SP_TH1(MCH)+COUN
                IF(IPH.EQ.0) SP_PH0(MCH)=SP_PH0(MCH)+COUN
                IF(IPH.EQ.1) SP_PH1(MCH)=SP_PH1(MCH)+COUN
C
                IF(IXI.EQ.0) SP_XI0(MCH)=SP_XI0(MCH)+COUN
                IF(IXI.EQ.1) SP_XI1(MCH)=SP_XI1(MCH)+COUN
                IF(IYI.EQ.0) SP_YI0(MCH)=SP_YI0(MCH)+COUN
                IF(IYI.EQ.1) SP_YI1(MCH)=SP_YI1(MCH)+COUN
C
                IF(IXO.EQ.0) SP_XO0(MCH)=SP_XO0(MCH)+COUN
                IF(IXO.EQ.1) SP_XO1(MCH)=SP_XO1(MCH)+COUN
                IF(IYO.EQ.0) SP_YO0(MCH)=SP_YO0(MCH)+COUN
                IF(IYO.EQ.1) SP_YO1(MCH)=SP_YO1(MCH)+COUN
C
IALL=0
IALL=ITH*IPH*IXI*IYI*IXO*IYO
IF(IALL.EQ.0) SP_ALL0(MCH)=SP_ALL0(MCH)+COUN
IF(IALL.EQ.1) SP_ALL1(MCH)=SP_ALL1(MCH)+COUN
IF(IALL.EQ.1) SP_ALLU1(MCH)=SP_ALLU1(MCH)+COUN_UP
```

```
IF(IALL.EQ.1) SP_ALLD1(NCH)=SP_ALLD1(NCH)+COUN_DN
C
70 CONTINUE
C
IF(NPRIN.EQ.IPRI) THEN
WRITE(7,710) NEV,TH_P,PH_P,dOMEGA,Uxp,Uyp,Uzp,
1 UU,TH_SCATT,V11,V31,V12,V22,V32,PPI,EPI,BETA,GAM
WRITE(8,810) NEV,XSDP,DPROB,COUNTS,Xx,Yy,Zz,U_PH,U_TH,
1 Pxxp,Pyyp,Pzzp,Pzz,Pmup,Px,Py,Pz,Pmu
WRITE(9,910) NEV,Umx,Umy,Umz,XT,YT,XFEC,YFEC
C
710 FORMAT(1H ,I7,1X,2F6.3,F9.6,3F7.3,1X,2F7.3,
1 1X,5F7.3,1X,2F7.1,F7.3,F7.4)
810 FORMAT(1H ,I7,F10.3,F7.4,E11.4,1X,3F5.1,1X,2F6.3,1X,3F6.1,
1 2F7.1,1X,4F6.1)
910 FORMAT(1H ,I7,1X,3F7.3,1X,2F7.2,1X,2F7.2)
NPRIN=0
ENDIF
C
ENDDO ! End of MM-Loop
ENDDO ! End of LL-Loop
80 CONTINUE
ENDDO ! End of KK-Loop
ENDDO ! End of JJ-Loop
ENDDO ! End of II-Loop
C
DIVT=1.0
IF(DMAX.GT.9999.0) DIVT=10.0
IF(DMAX.GT.99999.0) DIVT=100.0
IF(DMAX.GT.999999.0) DIVT=1000.0
IF(DIVT.EQ.1.0) GO TO 86
DO I=1,60
D_MUTH(I)=D_MUTH(I)/DIVT
ENDDO
86 CONTINUE
C
WRITE(6,644) DIVT

644 FORMAT(' MUON THETA-DISTRIBUTION IN PION REST FRAME (3 deg/ch)',
1 '  ,DIVIDED BY FACTOR ',F5.0)
WRITE(6,645) (D_MUTH(I),I=1,60)
645 FORMAT(1H ,20F6.0/1X,20F6.0/1X,20F6.0/)
C
WRITE(6,648)
648 FORMAT(' OUTPUT SPECTRA GIVING CROSS SECTIONS in ub/sr/MeV/c.',
1 ' The SUMS are MULTIPLIED by 3.0, to REFLECT PROPER ',
2 'NORMALIZATION')
C
WRITE(6,649)
649 FORMAT('   P      ALL_O   ALL_IN   Ano    TH_OUT  TH_IN   ',
1 ' PH_OUT  PH_IN    XI_OUT  XI_IN    YI_OUT  YI_IN    XO_OUT ',
2 ' XO_IN    YO_OUT  YO_IN')
C
K=(PMOO-3.0)
DO I=1,86 ! Output spectra
K=K+3
C Calculate the analyzing power for each interval
ANA=0.0
CUP=SP_ALLU1(I)
CDN=SP_ALLD1(I)
CUD=CUP+CDN
IF(CUD.EQ.0.0) GO TO 90
ANA=(CUP-CDN)/CUD
90 CONTINUE
C
WRITE(6,650) K,SP_ALLO(I),SP_ALL1(I),ANA,
```

```
 1 SP_TH0(I),SP_TH1(I),SP_PH0(I),SP_PH1(I),
 2 SP_XI0(I),SP_XI1(I),SP_YI0(I),SP_YI1(I),
 3 SP_X00(I),SP_X01(I),SP_Y00(I),SP_Y01(I)
 ENDDO
 650 FORMAT(1H ,I4,2X,2F8.4,F7.3,1X,2F8.4,1X,2F8.4,1X,2F8.4,
 1 1X,2F8.4,1X,2F8.4,1X,2F8.4)
 C
 DO I=1,14
 SUM(I)=0.0
 ENDDO
 C
 DO I=1,86 ! Generate sum for each spectrum
 SUM(1)=SUM(1)+3.0*SP_ALL0(I)
 SUM(2)=SUM(2)+3.0*SP_ALL1(I)
 SUM(3)=SUM(3)+3.0*SP_TH0(I)
 SUM(4)=SUM(4)+3.0*SP_TH1(I)
 SUM(5)=SUM(5)+3.0*SP_PH0(I)
 SUM(6)=SUM(6)+3.0*SP_PH1(I)
 SUM(7)=SUM(7)+3.0*SP_XI0(I)
 SUM(8)=SUM(8)+3.0*SP_XI1(I)
 SUM(9)=SUM(9)+3.0*SP_YI0(I)
 SUM(10)=SUM(10)+3.0*SP_YI1(I)
                 SUM(11)=SUM(11)+3.0*SP_X00(I)
                 SUM(12)=SUM(12)+3.0*SP_X01(I)
                 SUM(13)=SUM(13)+3.0*SP_Y00(I)
 SUM(14)=SUM(14)+3.0*SP_Y01(I)
 ENDDO
 WRITE(6,655) (SUM(I),I=1,14)
 655 FORMAT('OSUM :',1X,2F8.2,8X,2F8.2,1X,2F8.2,1X,2F8.2,1X,2F8.2,1X,2F8.2,
 1 1X,2F8.2,1X,2F8.2)
 C
 END
 C ------------------------------------------------------------------------
 C
         SUBROUTINE RANDOM(RX)
 C       A special random number generator is used that will hopefully
 C       minimize correlations between random numbers.
 REAL*8 RX
         DIMENSION V(10001)
         COMMON /RAND/ IR1,IR2
 C
         IF(RX.NE.2.0) GO TO 5
 C       Exercise the RANDOM number generator
                 DO I=1,3174
                 CALL RANDU(IR1,IR2,RAND)
                 ENDDO
 C       Fill a large vector with random numbers
                 DO I=1,10001
                 CALL RANDU(IR1,IR2,RAND)
                 V(I)=RAND
                 ENDDO
 C       Random numbers are then calculated according to the prescription
 5               CALL RANDU(IR1,IR2,RAND)
                 R=10000.0*RAND+0.999999
                 IR=R
                 RX=V(IR)
                 CALL RANDU(IR1,IR2,RAND)
                 V(IR)=RAND      ! Replace used random number with a new one
         RETURN
 END
 C ------------------------------------------------------------------------
```